Summer 2021

J/ψ Photoproduction Near Threshold With CLAS12

Joseph Newton
Old Dominion University, jnewt018@odu.edu

Recommended Citation

Newton, Joseph. "J/ψ Photoproduction Near Threshold With CLAS12" (2021). Doctor of Philosophy (PhD), Dissertation, Physics, Old Dominion University, DOI: 10.25777/3ne8-0168
https://digitalcommons.odu.edu/physics_etds/134

J/ψ PHOTOPRODUCTION NEAR THRESHOLD WITH CLAS12

by

Joseph Newton
B.S. May 2014, Old Dominion University
M.S. December 2015, Old Dominion University

A Dissertation Submitted to the Faculty of
Old Dominion University in Partial Fulfillment of the
Requirements for the Degree of

DOCTOR OF PHILOSOPHY

PHYSICS

OLD DOMINION UNIVERSITY
August 2021

Approved by:

Stepan Stepanyan (Director)

Gail Dodge (Member)

Stephen Bueltmann (Member)

Colm Whelan (Member)

Steven Pascal (Member)

ABSTRACT

J/ψ PHOTOPRODUCTION NEAR THRESHOLD WITH CLAS12

Joseph Newton
Old Dominion University, 2021
Director: Dr. Stepan Stepanyan

The structure of the proton is comprised of quarks and a sea of gluons. A mechanism that can extract the characteristics of the hidden-color correlations of the nuclear wavefunction is the production of charm near threshold. Due to the fact that momentum transfer is large near threshold in the production of J/ψ, all three valence quarks must act coherently to exchange energy for the reaction to occur. Models have been developed to predict the nature of J/ψ photoproduction at these specific energies. These include production mechanisms with the two-gluon and three-gluon exchanges. The transferred momentum dependence of the differential cross sections are sensitive to the gluonic form factors, which describe the distribution of color charge in the proton. The CLAS12 detector is capable of measuring J/ψ photoproduction at the energy range close to the threshold. Work showcased in this dissertation encompasses the preparation of the CLAS12 experiments, including the optimization of tracking reconstruction through the study of the Torus magnetic field. In terms of software, contributions were made to the CLAS12 Event Builder, a key stage of reconstruction where event-by-event information is summarized for efficient data analysis. After the run periods were successfully completed, analysis of the RG-A data commenced and an analysis framework was developed to measure the differential and total cross sections of J/ψ photoproduction in Hall B.

ACKNOWLEDGMENTS

My time as a graduate student at Old Dominion University has been very rewarding. There are so many dedicated people that made this work and my development as a scientist possible.

After passing the written qualifying exam in 2015, I began my search for a doctoral supervisor. I found out that Stepan Stepanyan was looking for a graduate student, so I decided to work with him. That was a great decision. Working with him allowed me to be involved with not only an interesting analysis topic, but also to be involved with the final stages of the 12 GeV upgrade. His vast array of knowledge, experience, and enthusiasm was exceptional. He was always available if I had any questions and I have learned a lot from him.

In addition to my doctoral supervisor, I would also like to acknowledge the great team of scientists, post-docs, and graduate students that I collaborated with over the last four years. My di-lepton analysis group, which was instrumental in getting feedback and organizing the analysis, consisted of Rafayel Paremuzyan, Nathan Baltzell, Valery Kubarovsky, Silvia Niccolai, Bryan McKinnon, Pawel Nadel-Turonski, Pierre Chatagnon, Jiwan Poudel, Richard Tyson, and many others.

Mac Mestayer, who I worked with during the Torus Field Mapping project, was an excellent individual to work with. Improving tracking reconstruction with the field mapping was a great joy. I enjoyed our conversations and his wisdom and sense of humor.

I would also like to acknowledge the CLAS12 software group for their helpfulness and their patience. It was a great experience to be involved with the CLAS12 event builder. Gagik Gavalian was one of the first scientists I worked with when I first starting doing research at Jefferson Lab. He gave very useful advice and helped me learned about the software side of physics.

I want to thank Old Dominion University and the physics department for all of the opportunities and education over the years. My professors and classmates have been amazing.

Most of all, I want to thank my family for always being there for me. I am blessed to have such a supportive and loving family.

TABLE OF CONTENTS

Page

Chapter

LIST OF TABLES

Table Page

Table Page

LIST OF FIGURES

Figure Page

CHAPTER 1

INTRODUCTION

The observation of the J/ψ meson was an important step in advancing the understanding of the quark model. Before the observation of J/ψ, there were three confirmed quarks: up, down, and strange. The existence of heavy quarks, such as charm, confirmed the predictions made by the Glashow–Iliopoulos–Maiani (GIM) mechanism, which explained the processes behind flavor-changing neutral currents.[1] The November Revolution of 1974 culminated in the observation of J/ψ, a meson with a charm-anti-charm ($c\bar{c}$) pair. It was discovered at two laboratories: Brookhaven National Laboratory (BNL) and Stanford Linear Accelerator Facility (SLAC). The experiment at BNL consisted of a proton beam colliding with a Beryllium target.[2] The initial intent of the experiment was to study heavy photons, so the observation of a sharp resonance was unexpected. At SLAC, another experiment was initally designed to study scattering and annihilations related to elementary particles.[3] This experiment consisted of an e^+e^- collider.[4] Teams lead by Samuel Ting (BNL) and Burton Richter (SLAC) confirmed the existence of a sharp and narrow peak at 3.097 GeV with a decay width of 93 keV. The name J/ψ originated as the combination of two names (J and ψ) associated with the two groups that observed the resonance. These combined efforts resulted in a Nobel Prize.

Over time, the production of the J/ψ meson has generated intense theoretical interest due to its sensitivity to gluonic form factors, which describe the distribution of color charge in the proton. From an experimental point of view, measurements of the J/ψ production cross section were accomplished at electron accelerator facilities at SLAC and Cornell at higher energies above 11 GeV. The results from the SLAC experiment[5] corroborated the two-gluon exchange model; however, a data point from Cornell suggested a re-examination of the production mechanism.[6] It appeared that the cross section is much larger closer to threshold than was predicted by the two-gluon exchange model. A three-gluon exchange model was proposed, which explained the unique behavior of J/ψ photoproduction closer to the threshold energy, which is the minimum E_γ needed to produce a J/ψ vector meson on a nucleon.

The mechanism of J/ψ production can be illustrated by relating J/ψ-N scattering with J/ψ photoproduction through the Vector Meson Dominance (VMD) model. In this case, the incoming photon fluctuates into a $c\bar{c}$ pair and becomes a vector meson after the momentum transfer with the target. Close to the threshold energy at 8.21 GeV, the momentum transfer becomes large, causing a dominance of multi-gluon interactions. This t-channel production near threshold becomes more of an elastic collision since the three valence quarks contribute momenta to the production of J/ψ.[7]

The CEBAF facility's upgrade from 6 GeV and 12 GeV provides an ideal experimental set-up to measure the differential and total cross sections of J/ψ photoproduction. The t-dependence of the differential cross section could give more information about the proton gluonic form factor. The total cross section as a function of E_γ would help explain the production mechanism near threshold. The CLAS12 detector in Hall B is capable of detecting and identifying J/ψ mesons using their decay to e^+e^- pairs. Another channel resulting in $\mu^+\mu^-$ decays also occur with the same branching ratio; however, the analysis highlighted in this dissertation emphasize e^+e^- detection since more is currently understood with regards to e^+e^- identification. Two scenarios are possible with CLAS12: tagged and un-tagged photoproduction. With tagged photoproduction, the scattered electron is measured directly by the Forward Tagger of CLAS12 to analyze the properties of the exchanged quasi-real photon. The un-tagged photoproduction, the analysis of choice for this dissertation, does not involve the direct measurement of the scattered electron through the Forward Tagger but rather the missing momentum and missing mass analysis by analyzing the reaction, $ep \to e^+e^-p(X)$, where X is the un-detected scattered electron.

The scope of the dissertation ranges from pre-experiment software development and event reconstruction optimization to the analysis of J/ψ events from RG-A datasets. Since kinematic variables (mass, photon energy, and momentum transfer) rely on well-understood charged particle reconstruction in the CLAS12 forward detector, a thorough mapping of the Torus magnetic field was done to determine the true positions and orientations of the six coils, leading to a better representation of the momentum of the final-state particles. In addition, the development of the CLAS12 Event Builder, a key component of the CLAS12 reconstruction software, aided in the analysis of not only J/ψ photoproduction, but all CLAS12 analyses. Finally, a well-advanced analysis framework, with particle identification, event selection, momentum corrections, fiducial cuts, acceptance studies, background studies, and cross section extraction procedures, was created. As a result, the preliminary differential and total cross section measurements for J/ψ photoproduction are shown and explained in this dissertation.

CHAPTER 2

PHYSICS BACKGROUND

2.1 QUANTUM CHROMODYNAMICS

Quantum chromodynamics (QCD) is the theory that describes the strong interaction, which is the force associated with holding nuclei together. As described earlier, the nucleon contains three valence quarks in a sea of gluons. The fundamentals of QCD draw parallels to the highly successful theory of Quantum Electrodynamics (QED), which accurately describes electromagnetic interactions. Unlike QED, which follows a U(1) local gauge symmetry, QCD's symmetry is associated with the SU(3) local phase transformation, as shown below,

$$\psi(x) \to \;{}'(x) = \exp(ig_s\alpha(x) \cdot \hat{T})\psi(x). \tag{1}$$

In the above transformation, $\hat{T}$ corresponds to a group of generator matrices that are related to the SU(3) symmetry group and $\alpha(x)$ are functions of the space-time coordinate, x. The fact that there are three valence quarks combined with the structure of the SU(3) matrices gives rise to the necessity to incorporate ”color” charge, which are the additional degrees of freedom required to complete the picture. By modifying the Dirac equation with the additional interaction terms for QCD, this allows for the derivation of the interaction vertex of two quarks and a gluon (qqg), as shown in the equation below,

$$g_s T^a \gamma^\mu G^a_\mu \psi = g_s \frac{1}{2} \lambda^a \gamma^\mu G^a_\mu \psi. \tag{2}$$

One of the distinct differences from QED is the presence of eight gluons that are tied to eight generators of the SU(3) local gauge symmetry. For QCD, there are three ”color” states named red (r), blue (b), and green (g). For example, the red (r) wave function is written as,

$$r = \begin{pmatrix} 1 \\ 0 \\ 0 \end{pmatrix}. \tag{3}$$

The interactions between quarks and gluons can be described by the connection between non-diagonal Gell-Mann matrices to quarks that contain a different color charge. Both quarks and gluons can have color charge and anti-color charge. This results in an octet of color charge combinations. The possible combinations of gluon color charge are: $r\bar{g}$, $g\bar{r}$, $r\bar{b}$, $b\bar{r}$, $g\bar{b}$, $b\bar{g}$, $\frac{1}{\sqrt{(2)}}(r\bar{r} - g\bar{g})$, and $\frac{1}{\sqrt{(6)}}(r\bar{r} + g\bar{g} - 2b\bar{b})$.[8]

An important implication of QCD is the concept of color confinement, which postulates that quarks are never observed as free particles. Rather, they are only part of colorless bound states such as mesons and baryons. The wavefunction associated with color for mesonic states is written as,

$$\psi^c(q\bar{q}) = \frac{1}{\sqrt{3}}(r\bar{r} + g\bar{g} + b\bar{b}). \tag{4}$$

For the baryonic case with three quarks in a bound state, the colored wavefunction is constructed as,

$$\psi^c(qqq) = \frac{1}{\sqrt{6}}(rgb - rbg + gbr - grb + brg - bgr). \tag{5}$$

The dynamics of QCD can be encapsulated by its Lagrangian formula, which describes the interactions of quarks and gluons. This allows for the determination kinematic behavior such as the strength of the strong interaction. The Lagrangian for QCD is

$$L = -\frac{1}{4}F^a_{\mu v}F^{a\mu v} + \sum \bar{\psi}_k(iD - m_k)\psi_k. \tag{6}$$

Embedded in the Lagrangian is the gluon field strength tensor, which is formulated as

$$F^a_{\mu v} = \partial_\mu A^a_v - \partial_v A^a_\mu + g f^{abc} A^b_\mu A^c_v. \tag{7}$$

Also, the gauge covariant derivative is utilized in the Lagrangian and it is

$$D_\mu = \partial_\mu - igA^a_\mu T^a. \tag{8}$$

The QCD has a dependence on the strong-interaction coupling constant, g.[9] Using g, the strong fine-structure constant is written as

$$\alpha_s = \frac{g^2}{4\pi}. \tag{9}$$

As discussed earlier, color confinement limits quarks by never allowing the observation of free quarks that are not bound to other multi-quark-gluon states. However, when energy becomes very large, the coupling of the g^2 term will be reduced by a large amount, resulting in asymptotic freedom.[10]

2.2 PARTON MODEL AND SLAC FINDINGS

The parton model, which was first proposed by Richard Feynman, sought to explain the behavior of high-energy collisions involving hadrons like protons. According to this model, nucleons are not point-like particles, but are comprised of constituent point-like particles denoted as partons, which would later be referred to as quarks. The behavior of these partons would be described by parton distribution functions (PDFs).

The kinematic variables of the parton such as energy, momentum, and mass are re-written in terms of the scaling rather than the entire macroscopic proton. For example, the energy, E, is written as xE. In the case where an incoming photon strikes one of the partons in the proton, a momentum distribution can be constructed, which can describe the probability that the struck parton, i, contains a fraction x of the total momentum of the proton p. The sums of the probability parton distributions add up to 1,

$$\sum_i \int dx x f_i(x) = 1. \tag{10}$$

This probability distribution function, $f(x)$,is used to derive the inelastic structure functions, which are

$$F_2(x) = \sum_i e_i^2 x f_i(x) \tag{11}$$

and

$$F_1(x) = \frac{1}{2x} F_2(x). \tag{12}$$

These functions are only dependent on the Bjorken variable, x,.[11]

The significance of this relation, also known as the Callan-Gross relation, is that it describes the elastic scattering from particles with a spin of $\frac{1}{2}$. The structure function that purely describes the electromagnetic interaction, F_2, can be described in the following way,

$$F_2^{ep}(x) = x \sum_i Q_i^2 q_i^p(x). \tag{13}$$

As shown in the above equation, the structure function, F_2, is constructed as the superposition of parton distribution functions (PDFs). Parton distribution functions describe the structural properties of the proton. In the parton model (or quark model to be precise), the proton consists of three valence quarks with two up quarks and one down quark. In reality, it is more complex since there are interactions that occur within the proton that can produce fluctuating $q\bar{q}$ pairs from quarks that interact through gluon exchanges. However, the main contributions are shown in the structure function formalism below,

$$F_2^{ep}(x) = x\sum_i Q_i^2 q_i^p(x) = x\left(\frac{4}{9}u^p(x) + \frac{1}{9}d^p(x) + \frac{4}{9}\bar{u}^p(x) + \frac{1}{9}d\bar{d}^p(x)\right). \tag{14}$$

$F_2^{ep}(x)$ represents the structure functions for electron-proton scattering.[8] For electron-neutron scattering, the structure functions consist of,

$$F_2^{en}(x) = x\sum_i Q_i^2 q_i^n(x) = x\left(\frac{4}{9}u^n(x) + \frac{1}{9}d^n(x) + \frac{4}{9}\bar{u}^n(x) + \frac{1}{9}d\bar{d}^n(x)\right). \tag{15}$$

Due to isospin symmetry, which equates the proton up-quark and neutron down-quark PDFs, the structure functions are

$$F_2^{ep} = 2xF_1^{ep}(x) = x\left[\frac{4}{9}u(x) + \frac{1}{9}d(x) + \frac{4}{9}\bar{u}(x) + \frac{1}{9}\bar{d}(x)\right] \tag{16}$$

and

$$F_2^{en} = 2xF_1^{en}(x) = x\left[\frac{4}{9}d(x) + \frac{1}{9}u(x) + \frac{4}{9}\bar{d}(x) + \frac{1}{9}\bar{u}(x)\right]. \tag{17}$$

The parton model was corroborated by experiments at SLAC. A series of inelastic electron-neutron scattering experiments sought to reveal the sub-structure of the proton. The MIT-SLAC collaboration observed a point-like substructure of the proton. Three spectrometers were used to detect the final-state reaction after impinging high-energy electrons up to 20 GeV into liquid Hydrogen and Deuterium targets.[12]

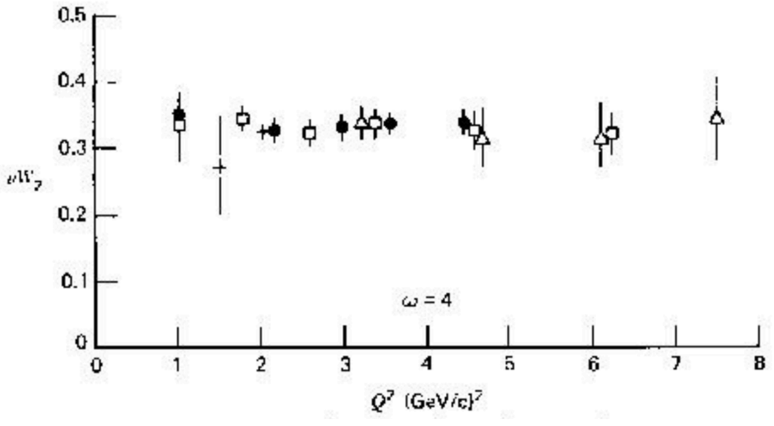

FIG. 1. Deep inelastic scattering at SLAC revealed the sub-structure (partons) of the proton.[11]

2.3 LEPTON-HADRON SCATTERING FORMALISM

As the electron approaches the relativistic limit, where $\beta \rightarrow 1$, the mechanism of the electron elastic scattering is illustrated by the Feynmann diagram in FIG. 2. In FIG. 2, there is a proton (4-momentum p_1) and an electron (4-momentum p_2) that exchanges a virtual four-momentum, q, before the same particles end up in the final-state with four-momenta, p_3 and p_4. The term, $\frac{k'e'}{2M}$, represents the effective anomalous magnetic moment and rest of the interaction term contains Dirac matrices.[13] The following parameter can be constructed:

$$q^2 = \frac{-4E^2 \sin^2 \frac{\theta}{2}}{1 + 2(\frac{E}{M}) \sin^2 \frac{\theta}{2}}. \tag{18}$$

The Mott-Rutherford formula for elastic scattering can be computed by the approximation where the electron energy is very small compared to the rest mass of the proton ($E << M$), as shown below,

$$\left(\frac{d\sigma}{d\Omega}\right)_{Mott} = \frac{\alpha^2}{4E^2 \sin^4 \frac{\theta}{2}} \cos^2 \frac{\theta}{2}. \tag{19}$$

In the elastic case for lepton-hadron scattering where the transferred momentum is large

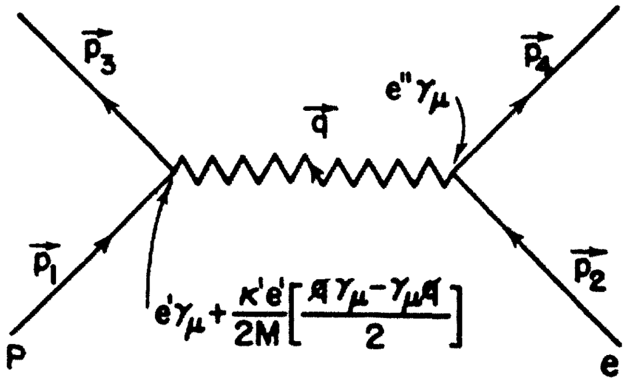

FIG. 2. The Feynmann diagram for the elastic scattering of a proton and electron.[13]

enough and the probe is sensitive to the charge and magnetization distributions inside the nucleon, the cross section will depend on the electric and magnetic form factors. The electric (G_E) and magnetic (G_M) form factors of the proton describe the distribution of charge and magnetization inside the proton. The construction of the elastic scattering formula is as follows,

$$\frac{d\sigma}{dQ^2} = \frac{4\pi\alpha^2}{Q^4}\left[\frac{G_E^2 + \tau G_M^2}{1+\tau}\left(1 - y - \frac{M^2 y^2}{Q^2}\right) + \frac{y^2}{2} G_M^2\right]. \tag{20}$$

The study of the structure of the nucleon is driven by scattering experiments of small probes, such as leptons, impinging on larger targets. In this framework, a high-energy lepton scatters off of a target, which is the nucleon. The scattering, which can be elastic or inelastic, includes the exchange of photons through the electromagnetic interaction. A virtual photon from the incoming electron with a momentum k transfers energy to the hadron. This results in the change of momentum, $k^{'}$, of the lepton in the final-state. The virtuality of the exchanged photon, is formulated as

$$Q^2 = -q^2 = -(k^{'} - k)^2. \tag{21}$$

In the deep inelastic scattering case when the transferred momentum (or virtuality of the exchanged photon) is large, the interaction takes place with partons inside the nucleon.

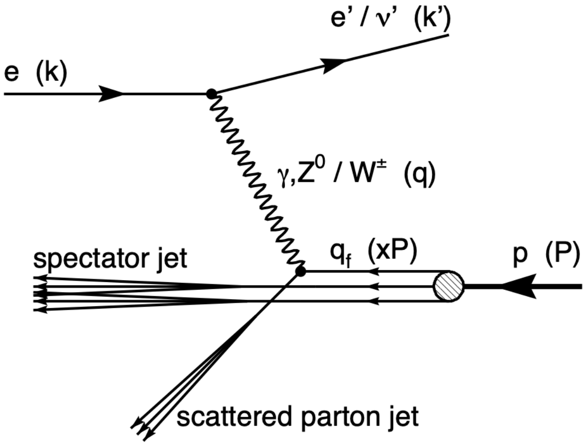

FIG. 3. Lepton-hadron scattering on a nuclear target.[14]

Such interactions are characterized by the momentum fraction of the proton carried by the struck parton. The Bjroken variable, x, is

$$x = \frac{Q^2}{2P \cdot q}. \tag{22}$$

The center-of-mass energy of the interaction is $\sqrt{s}$ and W defines the energy of the virtual photon and proton combined. W^2 is as follows,

$$W^2 = (P^{'})^2 = (P + q)^2 = M_X^2. \tag{23}$$

These kinematic variables can be used to describe both the elastic and inelastic cases.[14]

In the inelastic case, the target is not the entire proton but rather one part (or parton) of the proton. Therefore, the Bjorken variable, x, is needed to describe the scattering process in the inelastic case. For the differential cross section, both the electric (G_E) and magnetic (G_M) form factors are replaced by the structure functions, $F_1(x, Q^2)$ and $F_2(x, Q^2)$. This results in the double differential cross section,

$$\frac{d\sigma}{dQ^2 dx} = \frac{4\pi\alpha^2}{Q^4}\left[\left(1 + (1-y)^2\right) F_2 + \frac{1-y}{x}\left(F_2 - 2xF_1\right)\right]. \tag{24}$$

2.4 J/ψ PRODUCTION CLOSE TO THRESHOLD

At photon energies approaching the threshold production energy of the J/ψ meson, observables that are sensitive to the distribution of gluons in the proton can be measured. These observables also include hidden-color correlations of QCD wavefunctions. The production of charm near threshold can be observed with the following reaction, $\gamma p \rightarrow J/\psi p$, above the threshold energy, $E_{lab} = 8.21$ GeV.

2.4.1 PHOTOPRODUCTION MODELS

As opposed to J/ψ photoproduction at higher energies well above threshold, J/ψ photoproduction closer to threshold cannot occur unless each of the three valence quarks contributes energy to the creation of $c\bar{c}$. Specifically, the valence quarks are required to interact within a confined volume. The scenario in which this is possible is referred to as a proton Fock state, in which the radius of such a state is on the order of the Compton wavelength of the charm quark.

The Vector Meson Dominance (VMD) model plays an important role in relating the production of the vector to elastic $V-N$ scattering, and the cross section of the photoproduction can be written as:

$$\frac{d\sigma_{\gamma N \rightarrow VN}}{dt} = \kappa \frac{3\Gamma(V \rightarrow e^{+}e^{-})}{\alpha m_V} \frac{d\sigma_{VN \rightarrow VN}}{dt}. \tag{25}$$

where κ is a kinematic factor, α is the fine structure constant, Γ is the partial decay, and m_v is the meson mass.

The basis of VMD is the assumption that the incoming photon fluctuates to a $q\bar{q}$ pair, which scatters off the target and forms the outgoing meson. Due to this assumption, J/ψ photoproduction can be related to elastic ψ-N scattering through the following relation,

$$\sigma(\gamma N \rightarrow \psi N) = \left(\frac{4\pi\alpha}{\gamma_{\psi}^{2}}\right) \sigma_{el}^{\psi N}. \tag{26}$$

FIG. 4 provides an illustration of the characteristic scales of the VMD-related J/ψ photoproduction. The incoming photon fluctuates along a certain length, which is described as the longitudinal coherence length of the $c\bar{c}$ pair,

$$l_c = \frac{2E_{\gamma}^{lab}}{4mc^2} = 0.36 fm. \tag{27}$$

As the photon fluctuations occur, the quark anti-quark pair must be located within a certain transverse radius that is determined by the mass of the heavy charm quark,

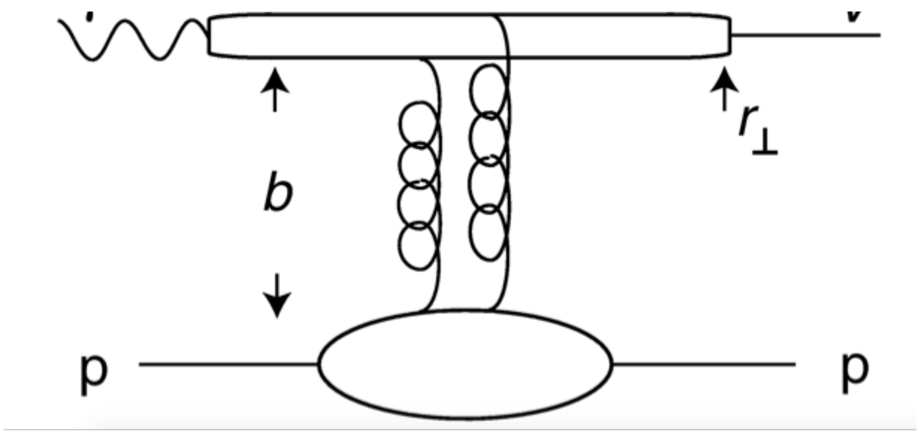

FIG. 4. The Vector Meson Dominance (VMD) model, which gives the characteristic scales of the reaction.[7]

$$r_\perp = \frac{1}{m_c} = 0.13 fm. \tag{28}$$

In addition, as the photon fluctuates into the $c\bar{c}$, it must be within the impact parameter, b, for its approach with the proton's valence quarks,

$$b = \frac{1}{\sqrt{-t}} = 0.13 fm. \tag{29}$$

The $c\bar{c}$ pair becomes a vector meson after moving through the distance characterized by the longitudinal formation length, l_f.

To describe the mechanism of J/ψ photoproduction near threshold in relation to the interaction of the quarks and gluons in the proton, perturbative QCD can be implemented to identify three processes contributing to the cross-section. The first is the leading twist contribution, where there are two spectator quarks. The second results in one spectator quark. In the third component, no quarks are spectators as all the quarks are interacting coherently.

In,[7] the cross section of the J/ψ photoproduction with the two-gluon exchange has the following form:

$$\frac{d\sigma}{dt} = N_{2g}\frac{(1-x)^2}{R^2M^2}F_{2g}(t)^2(s-m_p^2)^2. \tag{30}$$

and the three-gluon exchange has the following form,

$$\frac{d\sigma}{dt} = N_{3g}\frac{(1-x)^0}{R^4M^4}F_{3g}(t)^2(s-m_p^2)^2. \tag{31}$$

These models created a need for experimental data by a potential dedicated electron accelerator facility.

2.4.2 PAST CROSS SECTION MEASUREMENTS

After the discovery of J/ψ, various experiments were performed to study the production mechanisms at different energy ranges. For example, the Stanford Linear Accelerator Center (SLAC) ran an experiment where a bremsstrahlung beam was aimed at liquid Hydrogen and liquid Deuterium targets. Both electron and muon pairs from the decay of J/ψ were measured. The measurements were done at six photon energies ranging from 13 GeV to 21 GeV. The two-gluon exchange mechanism was compared to the data and the two were comparable. However, great interest into J/ψ photoproduction came as a result of the Cornell experiment, which produced a single data point that deviated from the two-gluon exchange model close to the threshold energy.

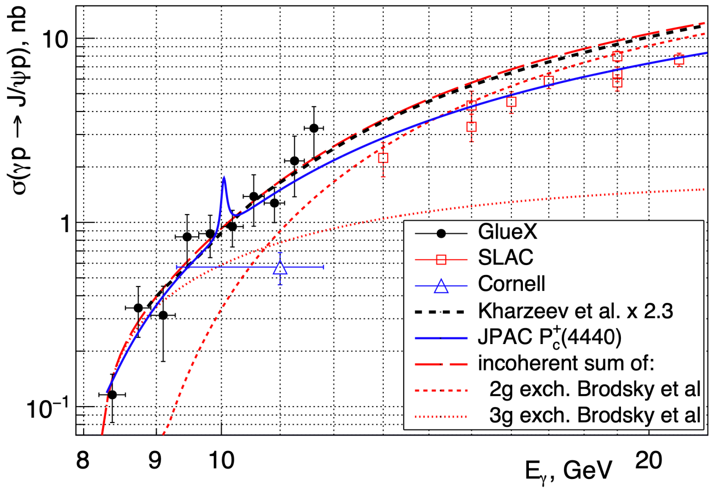

FIG. 5. A superposition of the available historic data from SLAC, Cornell, and JLab.[16]

The most recent data collected for the purpose of corroborating the J/ψ production models was related to the GlueX experiment in Hall D of Jefferson Lab. It was the first experiment where the photon energy was close to threshold. With a maximum beam energy of 11.8 GeV, the GlueX J/ψ experiment utilized a linearly polarized photon beam that originates from an electron beam that was incident upon a diamond radiator. Unlike the CLAS12 experiment, the scattered electron was analyzed and its photon energy was measured with large accuracy. However, the CLAS12 and GlueX experiments both use liquid Hydrogen targets inside Solenoid fields. Based on the data periods in 2016 and 2017, preliminary results were released and published by the GlueX collaboration. By studying the J/ψ photoproduction cross section as a function of photon energy, they concluded that the data do not completely follow either the two-gluon and three-gluon exchange models. However, the data, included in FIG. 5, display the dominance of the three-gluon exchange near the threshold energy.[16]

2.4.3 UN-TAGGED PHOTOPRODUCTION FORMALISM

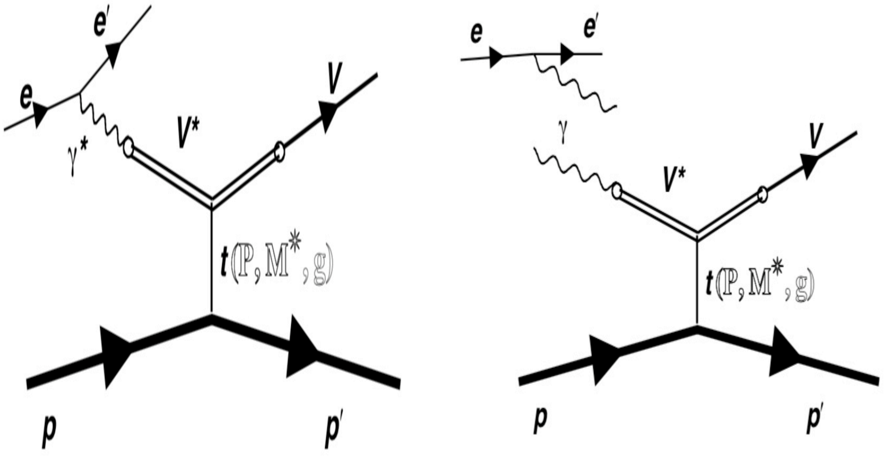

FIG. 6. The photoproduction and electroproduction of vector mesons.

The photoproduction process analyzed in this work is described by the reaction below,

$$ep \rightarrow Vp^{'}(e^{'}). \tag{32}$$

Through electron scattering, a vector meson is produced after impinging on the target proton, leaving the beam electron un-detected. This method of detection is un-tagged photoproduction.

In terms of the measurement of the J/ψ production near threshold, there are two mechanisms that contribute to the process: pure photoproduction and electroproduction, where the un-detected scattered electron has a Q^2 that is small ($Q^2 \sim 0$). For the electroproduction of mesons, the cross section can be interpreted as a sum of the cross sections induced by a transverse (σ_T) and longitudinal (σ_L) components of the virtual photon. The total electroproduction cross section is

$$\frac{d\sigma}{dt} = \Gamma_T \left(\frac{d\sigma_T}{dt} + \epsilon \frac{d\sigma_L}{dt} \right). \tag{33}$$

The flux of the transverse virtual photons are represented by the following:

$$\Gamma_T = \frac{\alpha}{4\pi} \frac{W^2 - m^2}{m^2 E^2} \frac{W}{Q^2} \frac{1}{1-\epsilon}. \tag{34}$$

The ϵ is the ratio of the longitudinal virtual flux and the transverse virtual flux and it is represented as:

$$\epsilon = \left(1 + 2 \frac{Q^2 + q_0^2}{4EE' - Q^2} \right)^{-1}. \tag{35}$$

Using the vector meson dominance (VMD), one can relate σ_T and σ_L to the photoproduction cross section:

$$\sigma_T = \sigma_\gamma \left(\frac{m_{J/\psi}^2}{m_{J/\psi}^2 + Q^2} \right)^2. \tag{36}$$

and,

$$\sigma_L = \left(\frac{m_{J/\psi}^2}{m_{J/\psi}^2 + Q^2} \right)^2 \cdot \frac{Q^2}{m_{J/\psi}^2} \cdot (1-x)^2 \cdot \xi(Q^2, \nu) \cdot \sigma_\gamma, \tag{37}$$

where $\xi(Q^2, \nu)$ is a normalization parameter and x is the Bjorken variable. Since the virtuality, Q^2 is small, the connection between the electroproduction and photproduction cross sections is written as,[17]

$$\frac{d\sigma_e}{dt} = \Gamma_T \frac{d\sigma_\gamma}{dt}. \tag{38}$$

2.5 LHCB PENTAQUARKS

Pentaquarks have been observed in the LHCb experiment at CERN and there a lot of interest into the mechanism that is behind the production of these five-quark systems. The pentaquarks are formed in the following channel,

$$P_c^+ = J/\psi p. \tag{39}$$

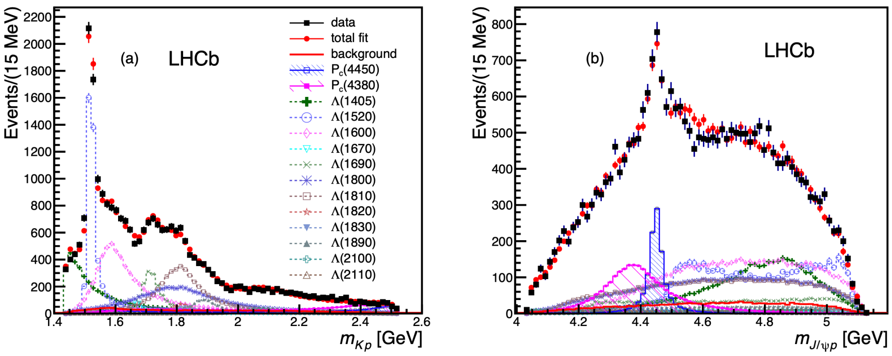

FIG. 7. The two pentaquarks observed in the LHCb experiment.[19]

The resonance associated with the pentaquark can be clearly extrapolated in the $J/\psi p$ invariant mass spectrum at 4449.8 MeV. The mass of P(4450) is relatively close to the sum of the masses of the proton and the J/ψ. The pentaquark resonances are shown in FIG. 7. The existence of these resonances in experimental conditions combined with theoretical limitations makes it convincing that the pentaquarks exists. Specifically, the Okubo-Zweig-Iizuka rule likely rules out the possibility of conventional baryons from decaying into a J/ψ and a proton.[19]

More recently, data published in 2019 from LHCb points to the splitting of the P(4450) resonance into two structures. In this case, the $P_c(4450)$ splits into $P_c(4440)$ and $P_c(4457)$.

It is postulated as the hyperfine splitting between hadrocharmonium constituents. There are two nearly degenerate hadrocharmonium states: $J^P = \frac{1}{2}$ and $J^P = \frac{3}{2}$.[20]

The pentaquarks are produced in the s-channel through the combination of a proton and J/ψ. The incoming photon turns into a J/ψ and then gets absorbed by the proton. The Breit-Wigner expression yields the pentaquark photoproduction cross section of the following reaction,

$$\gamma + p \rightarrow P_c \rightarrow J/\psi + p. \tag{40}$$

This results in the photoproduction cross section, which is

$$\sigma(W) = \frac{2J+1}{4} \frac{4\pi}{k^2} \frac{\frac{\Gamma^2}{4}}{(W - M_c)^2 + \frac{\Gamma^2}{4}} Br(P_c \rightarrow \gamma + p) Br(P_c \rightarrow J/\psi + p). \tag{41}$$

where J is the spin of the pentaquark and Γ is the total width.[17] If the s-channel mechanism exists, pentaquarks should be observed in the photoproduction of J/ψ mesons.

CHAPTER 3

EXPERIMENTAL SET-UP

3.1 OVERVIEW

The experiment of interest in this dissertation was a part of the CEBAF Large Acceptance Spectrometer (CLAS12) physics program at Jefferson Lab. At Jefferson Lab, an electron accelerator, known as the Continuous Electron Beam Accelerator Facility (CEBAF), accelerates and re-circulates electrons at high energies, reaching up to 12 GeV. This beam energy can be adjusted depending on the needs of the experiments. Once the beam is at the maximum energy after several passes, the beam is diverted into Hall B, where the CLAS12 detector is situated. The CLAS12 detector was designed to operate at high luminosity and to capture a larger acceptance of particle detection in order to detect a large fraction of produced secondary products of electron-target interactions. With a combination of magnetic fields, gas tracking chambers, scintillators, Cherenkov counters, calorimeters, a silicon tracker, and micro-mega trackers, an effective and wide-ranging physics program can be established with CLAS12. For un-tagged J/ψ photoproduction, the CLAS12 forward detector is the primary focus for the experiment. Due to the kinematical constraints of the reaction, the three final-state particles all travel at forward scattering angles into the acceptance region of the CLAS12 forward detector.

3.2 CEBAF

The Continuous Electron Beam Accelerator Facility (CEBAF) is an electron accelerator located on the campus of Jefferson Lab. CEBAF is a unique and state-of-the-art facility that utilizes superconducting radiofrequency (SRF) technology to transfer RF energy to electrons, while the electron beam bunches are forced along oscillating electric fields. It relies on various aspects of accelerator technology to achieve its physics goals. The entire accelerator is shaped in the form of a race track with two arcs containing re-circulating magnets, as shown in FIG. 8. The two straight sections of the accelerator provide SRF cavity boosts to pump RF energy for the purpose of accelerating the electron beam bunches. The injector is the source of the beam and is the starting point of the accelerator.[21]

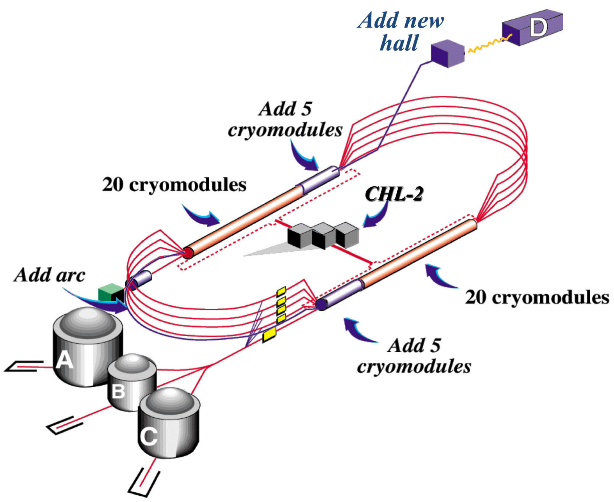

FIG. 8. CEBAF facility including the accelerator and the experimental halls[21]

3.3 CLAS12 DETECTOR

The CEBAF Large Acceptance Spectrometer (CLAS12) detector includes magnets, trackers, scintillator counters, calorimeters, and Cherenkov counters designed to study QCD and the structure of the nucleon. FIG. 9 gives a visual overview of the entire system, including the forward and central detectors.[22] The CLAS12 detector has the capability of efficiently detecting both charged and neutral particles over a large proportion of the solid angle. It is located in Experimental Hall B, to which the beam travels to after achieving the beam energy required by the experiment. The CLAS12 forward detector consists of a superconducting toroidal magnet that generates an azimuthal field. Charged particles have curved trajectories in the field that are analyzed by the drift chambers (DC) to calculate the momentum and vertex information of the particle. The FD also encompasses several detectors associated with particle identification including the High-Threshold Cherenkov Counter (HTCC), the Low-Threshold Cherenkov Counter (LTCC), the Electromagnetic Calorimeter (ECAL), and the Forward Time-Of-Flight (FTOF) scintillator counters. The polar angle coverage of the CLAS12 Forward Detector ranges from 5 degrees to 35 degrees. At higher scattering angles, the CLAS12 Central Detector is capable of detecting charged particles from 35 degrees to 125 degrees. The Solenoid magnet combined with the Central Vertex Tracker (CVT) provides the ability to calculate the momentum and vertex information from the analysis of the curvature of tracks. PID-related detectors in the CD are the Central Time-Of-Flight (CTOF) counter and the Central Neutron Detector (CND).

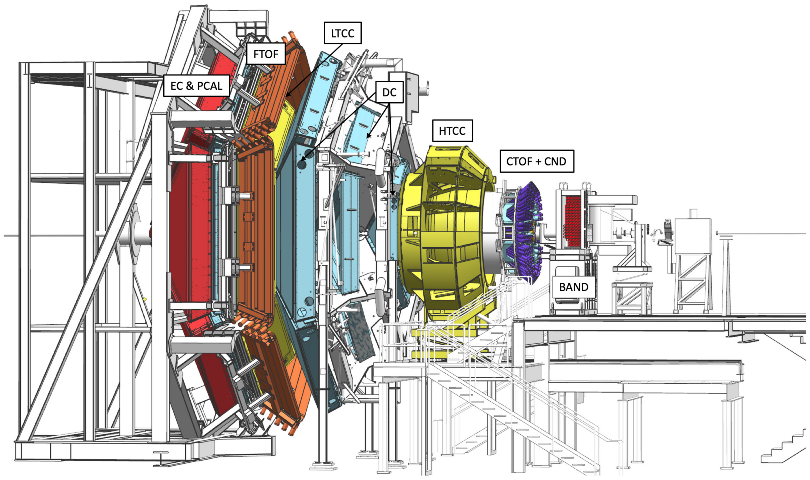

FIG. 9. A diagram of CLAS12 showing both the Forward and Central detectors and their subsystems[22]

3.3.1 BEAMLINE

The Hall B beamline allows for the safe and effective delivery of the electron beam from CEBAF to the physics target in the experimental hall. As a whole, the beamline provides the capability for experimenters to monitor the beam in real-time and allows for operators to alter the characteristics of the beam as necessary. One of the challenges for the 12 GeV upgrade was to keep a multitude of detectors and systems safe from the levels of radiation from the beam, which is in close proximity. To mitigate this issue, shielding was introduced in the region which is downstream from the Solenoid to avoid radiation damage to the CLAS12 detectors. In terms of the design of the system, the Hall B beamline is generally divided into two components. First, there is a "2C" line from the Beam Switch Yard (BSY). This portion of the beamline ranges from the CEBAF accelerator towards Hall B. Also, there is the second main region of the beamline, which is the 2H line that stretches from the upstream end of the hall to the beam dump in the downstream end. Upstream of the CLAS12 detector, there are a series of beam augmentation devices (quadrupoles and corrector magnets) which keep the beam size within tolerances and centered on the target, as observed in FIG. 10. In addition, there are corrector dipoles, which also improve the characteristics of the beam.[23]

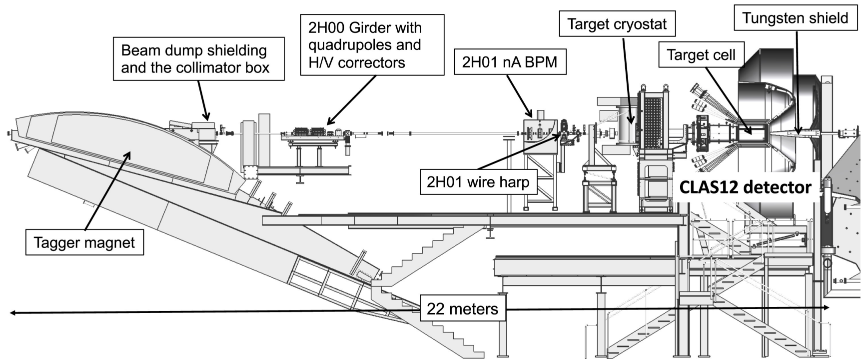

FIG. 10. A visual representation and schematic of the Hall B beamline[23]

3.3.2 TARGET

Located within the Solenoid magnet, the cryogenic target for CLAS12 provides a source of nucleons for the incoming beam of electron for various scattering experiments. For CLAS12, the two most common targets are liquid Hydrogen and liquid Deuterium. The rationale behind using liquified gas is to get enough density to satisfy luminosity requirements. As far as the dimensional characteristics, the target is 5 cm long in the form of a Kapton cone with a 23.66 mm upstream diameter and a 15.08 mm downstream diameter, which is shown in FIG. 11. On each end of the target, there are entrance and exit windows in the path of the electron beam. The target cell possesses a beam halo monitor that can be used for observing the beam in real-time. Surrounding the target cell is the scattering chamber, which is comprised of a Rohacell XT110 foam.[23]

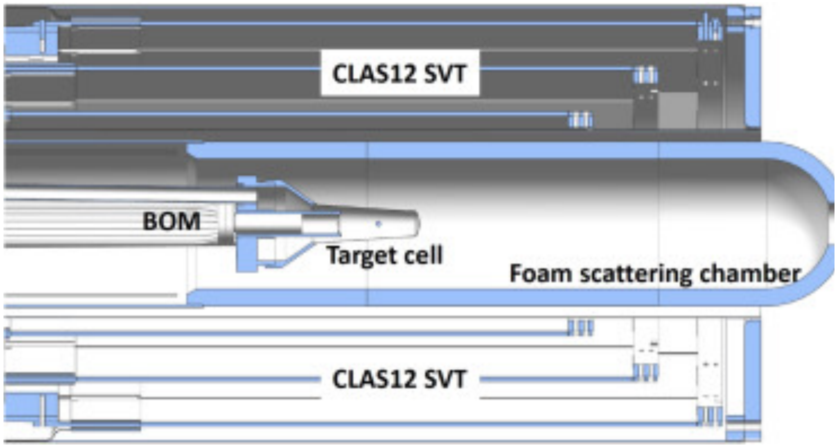

FIG. 11. CLAS12 target chamber which is impinged by the beam[23]

3.3.3 TORUS MAGNET

The CLAS12 Torus magnet allows for the presence of a toroidal magnetic field that can be used in conjunction with the drift chambers to measure the momentum of charged particles at forward scattering angles. It is a superconducting magnet that operates at ultra-cold temperatures. Comprising of six coils that form a series electrical connection, there are described as double-pancakes and have shapes similar to trapezoids, which is displayed in FIG. 12. The material is made up of copper-stabilized NbTi Rutherford cable. In order to supply Helium that is lowered to supercritical temperatures, the Torus Service Tower delivers the liquid to the six coils in order to transfer its operating temperature.

The field itself is Toroidal, which results in curved inward and outward bending charged particles. The maximum strength of the field can reach 3.6 T near the bore in the inner portion of the coil. Depending on the run conditions, the operating current can vary but its maximum current is 3770 A. Other characteristics of the Torus magnet include the coil-winding in which there are a total of 1404 turns (117 X 2 X 6).[24]

3.3.4 SOLENOID MAGNET

Just like the Torus magnet, the Solenoid magnet is designed to utilize superconducting

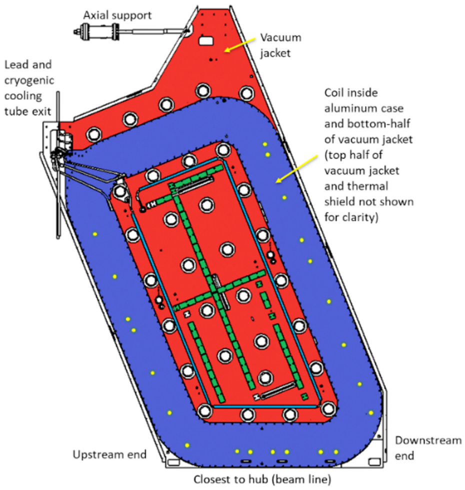

FIG. 12. The design of the Torus magnet[24]

wires that take advantage of the absence of electrical resistance. This results in powerful magnetic fields. The Solenoid, shown in FIG. 13, is described as a series of helically layer-wound coils that are cooled to ultra-cold temperatures. The Solenoid field offers several benefits regarding the desired physics goals of the CLAS12 program. It is mainly noted for providing the particles in the central region with a magnetic field that can induce helical tracks in the Central Vertex Tracker in order to reconstruct the momentum and vertex information. In addition to central tracking reconstruction, the Solenoid offers benefits and satisfies requirements for the CLAS12 program. For example, running at high-luminosity creates a higher rate of radiation that can be detrimental to the longevity of tracking detectors; therefore, the inclusion of the Solenoid field can act as an effective shield. In addition, running a highly-polarized target also requires a homogeneous magnetic field that is offered by the Solenoid magnet.[24]

In terms of the design and specification of the Solenoid, the five coils comprise of NbTi and they are connected in series with a current of 2416 Amps. The resulting magnetic field strength is 5 T. The first two inner coils are situated in a thick-walled stainless steel bobbin. The next two coils are the intermediate coils that are milled into the outer coil. The fifth coil is known as the shield coil. In total, there is 5096 turns. In order to operate the Solenoid, a 45 K supply temperature is necessary.[24]

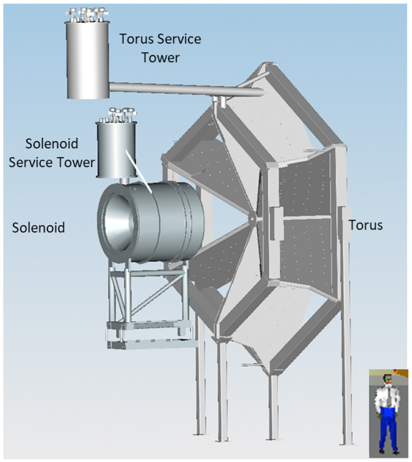

FIG. 13. The design of the Solenoid magnet[24]

3.3.5 DRIFT CHAMBERS (DC)

A component of the CLAS12 Forward tracking system is the drift chambers (DC), which are in FIG. 14. The DC allows for the reconstruction of the momentum and vertex information of charged particles that originate from the target. The tracing of the curvature of the charged particle tracks through the magnetic field is directly associated with the momentum of the track. That curvature can be quantified due to the ability of the DC to measure the time of the electron avalanche to precisely determine the position of the hit.

The CLAS12 physics program requires tracking detectors that can detect multi-particle events in a large geometrical acceptance. Due to reactions with small cross sections, the DC must be able to effectively reconstruct charged particle tracks at higher luminosities. One of the highest priorities of these CLAS12 DC trackers was the need for optimal momentum resolution. Many run groups contain experiments where exclusive reactions are analyzed by missing mass and invariant mass calculations. The resolution optimized to detect the resonances within their natural widths.

The CLAS12 DC was designed to accommodate these goals. It includes a total of 18 planar chambers. For each region, there are 2 superlayers with 6 layers each. Between the wires of two adjacent superlayers, there is a 6 degree separation. Many of the design characteristics were adapted from CLAS, but some modifications were made, including the

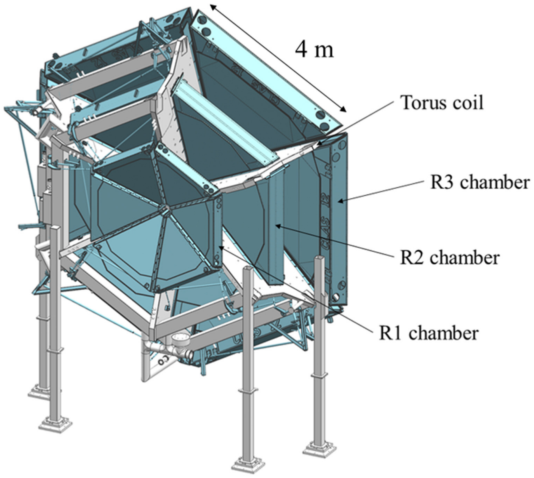

FIG. 14. An overlook of the CLAS12 drift chambers which contain a combination of sense and field wires to reconstruct the trajectory of charged particles in the magnetic field[25]

positioning of the DC compared to the position of the target. One of the design features of the DC was the smaller cells, which allow for more precise and robust track curvature reconstruction. The hexagonal shape of the cells creates less need for excessive amounts of wires. The diameters of the sense and field wires allow for greater strength and less of a chance for breakage. The DC for all six layers are self-supporting. The advantage is that it is easier to move for maintenance; however, this creates a bowing of the endplates on the order of 1-2 mm. That fact makes it more important for the DC to be analyzed for the wire tension, which can affect DC track reconstruction due to the varied length of the field and sense wires and the timing difference caused by the effect.[25]

3.3.6 ELECTROMAGNETIC CALORIMETER (ECAL)

For the CLAS12 upgrade, accommodations were required for the detection of high-energy electrons as well as photons and neutrons. Due to electrons with energies that can reach 12 GeV, electromagnetic showers needed to be absorbed by an extra layer of calorimeter. By doing this, the total radiation length of the material would be extended. The addition that was made to the CLAS12 EC was the pre-shower electromagnetic calorimeter (PCAL). The entirety of the EC can be described by six independent electromagnetic sampling calorimeters

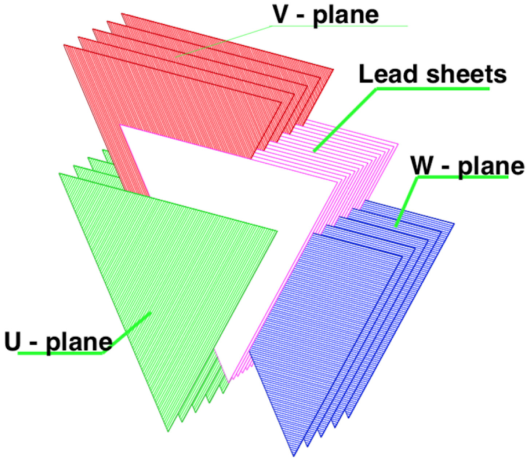

FIG. 15. A visual overlook of the Electromagnetic Calorimeter which contains three layers of material for sampling calculations of charged and neutral particles[26]

comprising of lead and scintillating material. The main purposes of the PCAL/ECAL is to provide solid trigger and particle identification capabilities. The PCAL/ECAL utilizes a triangular hodoscope geometry with a stereo readout, as shown in FIG. 15.[26]

3.3.7 FORWARD TIME-OF-FLIGHT (FTOF)

To properly identify hadrons in the CLAS12 forward detector, a detector is required to determine the speed of each track as a function of the momentum, which is determined primarily by the drift chambers. If the pathlength is known, then the speed as a function of momentum should be calculated by knowing the time-of-flight throughout that corresponding pathlength. The Forward Time-of-Flight (FTOF), illustrated in FIG. 16, is an effective detector due to its ability to precisely measure the time at which a charged particle passes through the scintillator material. Scintillators rely on the fact that charged particles, moving at speeds approaching the speed of light, excite atomic electrons in the scintillator material after which atomic electrons emit light going back to the ground state. That light is collected through the scintillator material and transferred to the photomultiplier tubes, which allow FTOF reconstruction to properly measure the time. The difference between that time and the RF-corrected start time is the time associated with the trajectory of the particle. The

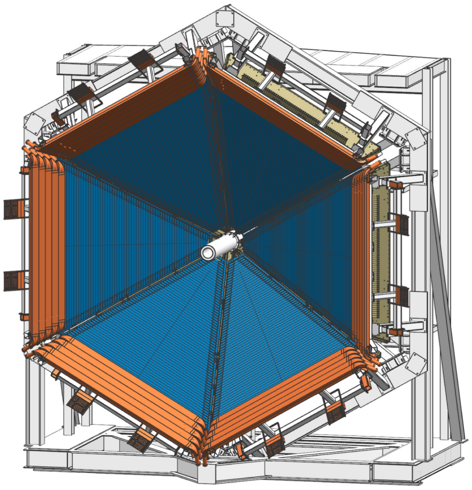

FIG. 16. An overview of the FTOF which allows for hadron identification[27]

FTOF detector system contains three layers of scintillators: Panel 1A, Panel 1B, and Panel 2. Panel 1A contains 23 scintillators, Panel 1B contains 62 scintillators, and Panel 2 contains 5 scintillators. In total, there are 540 scintillation counters with double-ended readout. They ranged from 17 cm to 426 cm. Two key features of the FTOF are excellent timing resolution and trigger capabilities that are flexible. The timing resolution of the FTOF ranges from 50 ps to 200 ps. The timing resolution is dependent ons the length of the scintillators. In general, shorter scintillators yield sharper resolutions than longer scintillators. The FTOF detectors play a vital role in the CLAS12 trigger system because several charged particles rely on a detector hit in FTOF to trigger the acquisition of that event.[27]

3.3.8 HIGH-THRESHOLD CHERENKOV COUNTER (HTCC)

To accomplish the physics goals of CLAS12, a robust and efficient electron detection system had to be developed to not only identify electrons, but to reject other particle identification candidates. In the CLAS12 forward detector, the High-Threshold Cherenkov Counter (HTCC) was built to detect electrons at scattering angles that range from 5-35 degrees and the entire azimuth range. Cherenkov counters take advantage of the physical principle, known as Cherenkov radiation, that occurs when a particle is traveling faster than the speed of light in a specific medium. In this case, high-speed particles, mostly electrons and pions, travel through Carbon Dioxide gas at 1 ATM of pressure. The HTCC is located directly in front of the drift chambers, before the heavy influence of the Torus magnetic field; therefore, the electrons and pions make straight tracks through mirrors, that capture light. For the purposes of particle identification, the HTCC relies on the minimum threshold momentum to help data analysts distinguish particles using the momentum calculated by the drift chambers. The minimum electron momentum threshold is 15 MeV. In terms of pions, the minimum pion momentum threshold is at 4.9 GeV. The material that was used to construct the HTCC consisted of multifocal mirrors that consist of 60 lightweight ellipsoidal mirrors. Within each sector, there are two half-sector mirrors that concentrate the Cherenkov radiation upon eight phototubes. In the entire HTCC, there are 48 channels that correspond to photomultiplier tubes (Electron Tube 9823QKB). Several priorities were established with regards to the usage of the HTCC. These include solid timing, high efficiency, and robust rejection of charged pions beyond 4.9 GeV.[28]

3.3.9 CENTRAL DETECTOR

For charged particles with higher scattering angles beyond the CLAS12 FD, the Central Detector (CD) can measure the momentum and identity of these particles. Under the influence of the Solenoid field, these particles have trajectories in the Central Vertex Tracker (CVT) where the momentum is measured by analyzing the helical tracks. The CVT consists of two detectors: the Silicon Vertex Tracker (SVT) and the Barrel Micromegas Tracker (BMT).[29] For neutral particle identification, the Central Neutron Detector (CND) has the ability to detect neutrons ranging from 200 MeV to 1 GeV.[30] Charged particle identification is made possible by the Central Time-Of-Flight (CTOF), which has a hermetic barrel of 48 scintillation counters with 25 cm radii. The average timing resolution of the CTOF is 80 ps.[31]

3.3.10 DATA ACQUISITION SYSTEM

With a combination of efficient and functional detectors, targets, and magnets, there is also a robust data acquisition system which allows for the storage of information on an event-by-event basis. The hardware components of the detectors record amplified analog signals that result from the interaction of particles with the materials. These analog signals are converted into digital signals using Analog-to-Digit Convertors (ADCS) and Time-to-Digit Convertors (TDCs) and then transferred to the network-based CLAS12 data acquisition (DAQ) system. The main purposes of the DAQ is to organize the information stemming from the CLAS12 detectors and transfer that information to the tape storage. In addition to the storage requirements, the DAQ system also has the capability to monitor data in real-time, which is an important priority for the optimal running of beamline experiments. The current performance of the CLAS12 DAQ, whose schematic is shown in FIG. 17, includes an event rate of 30 kHz and a data rate of 1 GB/s. In terms of the design of the DAQ, the data collection originates from front-end components, which are specifically called Readout Controllers (ROC[32]).

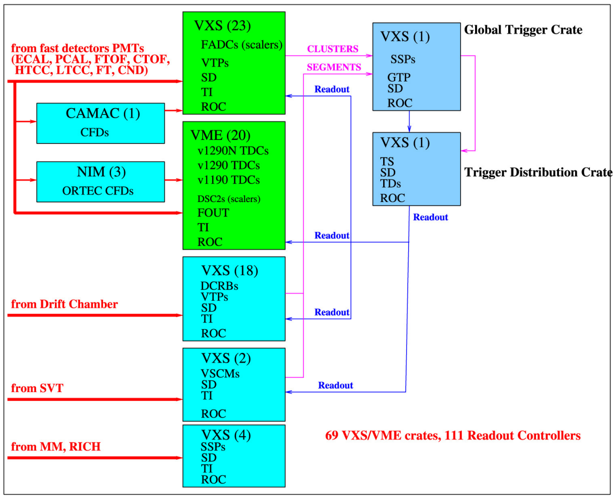

FIG. 17. Overview of the data acquisition system which has an event rate of 30 kHz[32]

3.3.11 TRIGGER SYSTEM

For each CLAS12 run period, there are a series of criteria that dictate the collection of data from the CLAS12 detectors by the CLAS12 DAQ. The system that is responsible for making a decision to record the data is called the trigger system. This trigger system is versatile and is efficient at isolating events based on the physics requirements within each of the run groups. Examples of triggers for Run Group A include electron triggers, opposite sector triggers for muons, the MesonEx trigger, and others. One requirement for the successful activation of the trigger system is an adequate trigger latency period, which had to be at least 8 microseconds. It is also required that the DAQ run at a very high rate with a greater than 95 percent live-time. Overall, the CLAS12 trigger is dependent on seven detectors: the HTCC, DC, FTOF, ECAL, CTOF, CND, and FT. The design of the trigger system contains three distinct stages of trigger activation. Firstly, the trigger system obtains values from the FADC and DCRB information. Using that information, data is processed based off of the specific detector. Secondly, calculations related to the timing and the location of hits for different portions of detectors are recorded for the triggers defined by the physics run group. The final stage is when a decision is made to keep or discard the event based off of the criteria. The schematic of the CLAS12 trigger system is illustrated in FIG. 18.[33]

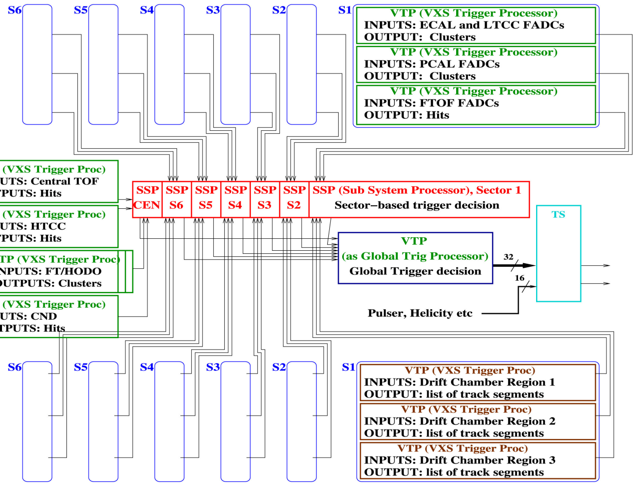

FIG. 18. A schematic of the trigger system which can accommodate different physics goals[33]

3.4 CLAS12 RECONSTRUCTION SOFTWARE

Nuclear and particle physics experiments require a software framework that possesses longevity and adaptability due to the long-term analysis after data collection. For CLAS12, the software framework and reconstruction of events contain a multitude of common analysis software tools for users to adopt. Due to the combination of systems, there is also a need for many services associated with each detector. The objectives of the software framework include event reconstruction, calibration, monitoring, CLAS12 physics analysis, detector geometry, and access to the CCDB database.

CLARA, which is a framework that uses data-stream processing, is the core of the architecture of the software framework. It is a modular design where the essential basic units are services put together by pipes. The coding language used was Java, for its portability and its ability to construct applications on diverse kinds of systems.[34]

3.4.1 EVENT BUILDER

The development of the CLAS12 Event Builder (EB), from 2016 to 2017, was an important step towards assembling a software reconstruction package that has the ability to effectively organize all of the relevant information of a physics event captured by the CLAS12 detector. COATJAVA, which is the JAVA-based reconstruction package that is a part of the general CLARA analysis framework, is a collection of services. Most of those services are associated with individual detectors where the values of ADCs and TDCs are converted into physical quantities such as energy and time. What makes the CLAS12 Event Builder (EB) service unique is that it receives information, in the form of data banks, and uses that information to tie everything together. The objective of the EB is to provide data analysts with important event-specific values such as particle identification quantities, event helicity, and accumulated charge. This makes it possible for the analysts to filter their events at the post-processing stage for individual final states.

The order in which the EB is utilized is important. During the reconstruction stage of data processing, the EB is first called as a service after the other detector services complete their calculations and output their data banks. This includes hit-based drift chamber tracking. Hit-based tracking is solely dependent on the position of DC wires and does not rely on timing since that information is not yet available for DC reconstruction. The CLAS12 EB uses the hit-based tracks and matches those track trajectories to the positions of hits in other detectors in the FD. Using a trigger assignment algorithm, a trigger particle (usually an electron) is used to calculate the event start time. That event start time is utilized by hit-based tracking and the entire process is re-done using the refined tracks. The specifics of those calculations will be explained in the next sections.

One of the ways in which event information is organized is geometrically matching track

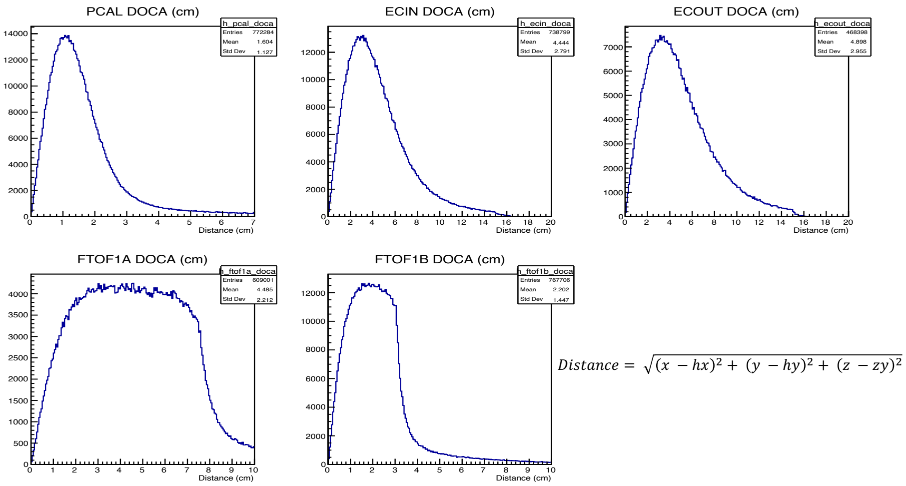

$$Distance = \sqrt{(x - hx)^2 + (y - hy)^2 + (z - zy)^2}$$

FIG. 19. Distance of the particle trajectory's closest approach to the detector hit.

trajectories with the hits in the individual portions of the CLAS12 detector. For example, when an electron comes out of the target vertex, it will make a curved path in the presence of the combined Torus and Solenoid magnetic fields. This curvature is quantified as momentum in the DC. Beyond the DC, there is a sharp drop-off in the magnitude of the magnetic field. Therefore, the particle's trajectory becomes more of a straight line towards the detector material. The EB calculates the distance of closest approach (DOCA) for all of the hits in all of the layers of detectors. This geometrical matching process plays a vital role in determining the characteristics of the particle beyond the momentum and vertex information. FIG. 19 is a representation of the DOCA values of simulated electrons in all layers of the forward calorimeters. A visual representation of a particle's trajectory nearing the proximity of the detector hits is illustrated in FIG. 20. The magnitude and the resolutions of the DOCA values are dependent on the hit position resolutions of the detectors. In the EB code, the cut thresholds are applied based on the spatial resolutions for the detectors. The EB output banks show the results of the hit association between the particle and detector responses.

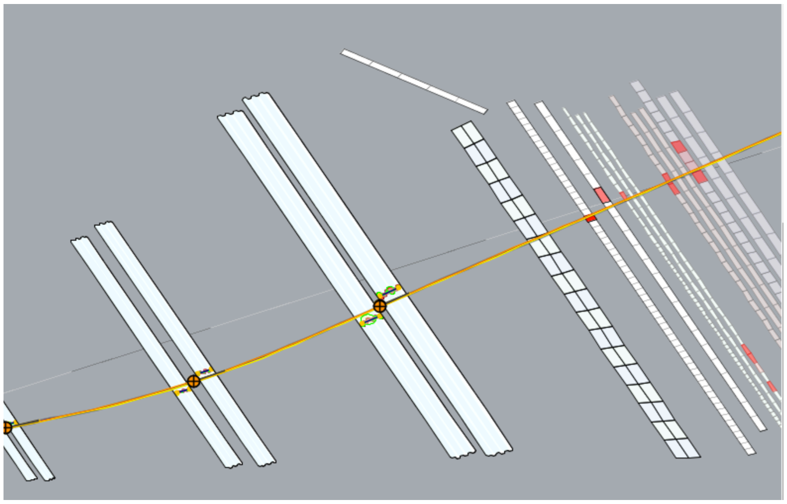

FIG. 20. CED display of a charged particle track penetrating the material of the CLAS12 forward detector

In order for accurate reconstruction of time-based tracking and particle identification, the timing values within events need to be understood. The times reported by the detector responses are absolute values from a DAQ trigger clock. To use the TDC information reported by detectors, the time of the interaction that created the event must be found. Therefore, calculating the event start time is a necessary step to allow for the absolute timing values to be utilized for tracking reconstruction and particle identification in various CLAS12 detectors. As stated earlier, the EB is called after hit-based tracking and information collected at that stage is used by the EB. During hit-based tracking, a trigger candidate is identified for the purpose of calculating the event start time. The rationale behind using the characteristics of the electron is the fact that the speed of the electron in virtually constant and known. In addition, the electron identification does not require information from detector times. Instead, they depend on values such as the sampling fraction in the ECAL and the number of photoelectrons in the HTCC. The EB possesses an algorithm that searches for electron candidates and ranks them depending on particle characteristics such as the momentum.

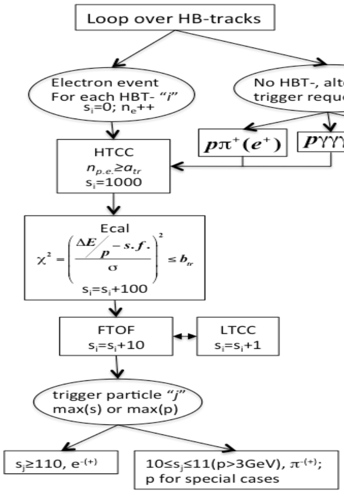

FIG. 21. A visual representation of the software trigger particle selection

Once an electron candidate is selected, the absolute timing value from a layer of FTOF and the pathlength of the electron to FTOF are used to calculate the event start time, which is the time corresponding to the electron's vertex position. As shown in FIG. 21, the EB has a special routine that uses a hierarchal approach to determining the best electron candidate based on the detector responses after hit-based tracking. The electron vertex time is defined as follows,

$$t_0^r = t_r - t_{tof}. \tag{42}$$

where t_r is the absolute time value reported by a component of FTOF. t_{tof} is the calculated time-of-flight based on the reconstructed pathlength from the interaction point to the detector hit position divided by the speed of light. Although t_0^r is a good approximation for the time of the beam-target interaction, various uncertainties involved with the calculation of that time creates a necessity to correct that time and reduce that uncertainty to allow for more precise timing-based particle identification. The method that is used involves the usage of the RF accelerator signal to further improve the calculation. The RF time, t_{RF}, which is measured in the TDC, contains a value called the trigger jitter, t_0. This time is written as,

$$t_{RF} = M \times \delta t + t_j. \tag{43}$$

where M can be a very large integer, δt is the CEBAF beam bunch separation time, and t_j is the time jitter. A new term, Δt, is defined to quantify the difference between the vertex time, t_0^r, and the reported RF time, t_{RF}. By combining the previous formulas, the Δt term is expressed as,

$$\Delta t = (t_0^r - t_j) - M \times \delta t + C. \tag{44}$$

where C is the RF offset. As a part of the calibration process, the C value is measured to ensure that the beam bunch arrival at the target and the TDC detection of the RF signal are synchronized. Once the RF offset is subtracted out, the extension of the production vertex needs to be taken into account. This is due to the reality that the interaction point for the start of each event is not a point-like target. The production vertex shift is considered in the term, Δt^r, as

$$\Delta^{t^r} = t_0^r - t_{RF} - \frac{z_t - z_0}{c} + m \times \delta t. \tag{45}$$

The terms, z_t and z_0, refer to the track production vertex and center of the target, respectively. After Δt^r is quantified, the RF-correction term, Δt_{RF}^{corr}, can be calculated, which is then used to finalize the event start time, t_0.[35] The RF-correction term is

$$\Delta t_{RF}^{corr} = Mod(\Delta t^r, \delta t) - \frac{\delta t}{2}. \tag{46}$$

and the event start time is

$$t_0 = t_0^r - \Delta t_{RF}^{corr}. \tag{47}$$

This event start time, t_0, is used by DC time-based tracking to improve the reconstruction of charged particles and it is also included in the time-based particle identification for particles constructed in the event builder.

The identification of charged particles in the CLAS12 EB relies on varying combinations of measured physical quantities from different subsystems. For electrons and positrons, the following conditions need to be satisfied.

- Correct charge of the track
- Contains clusters in ECAL and the HTCC

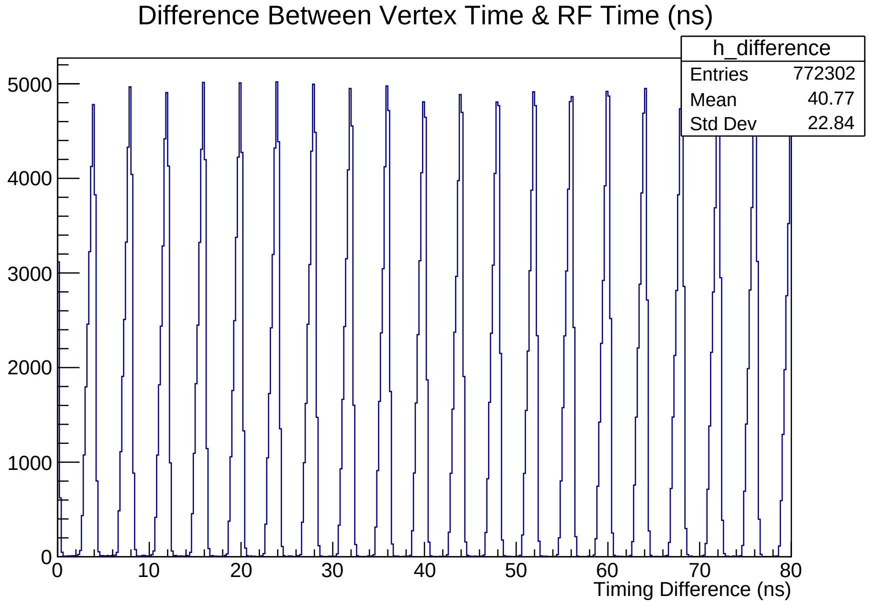

FIG. 22. The difference between the electron vertex time and the reported RF time in the Fall 2018 RG-A dataset

- Minimum PCAL energy is 60 MeV
- Number of photoelectrons is greater than 2
- The energy-dependent ECAL sampling fraction falls within 5σ of the expected mean

The identification of charged hadrons is performed by comparing the expected and measured vertex times based on the values when the mass of those particles is assigned in those calculations. To achieve this, the deviation of the particle's vertex time from the event start time is quantified. If it comes within 5σ of the expected value, then it will be identified accordingly. The following equation describes the calculation:

$$\Delta t(i) = t_0 - \left[t_{FTOF} - \frac{L}{\beta_i(p)} \right]. \tag{48}$$

where t_{FTOF} is the time the particle intersects the time-of-flight detector plane.

Neutral particles, such as photons and neutrons, are also identified in the EB. For photons in the forward detector, the EB searches for clusters in the three layers of ECAL that are not associated with any charged track in the DC. This means that the geometrical matching tests did not pass the specified thresholds for the DOCA values. These clusters are assumed to be from either neutrons or photons. To identify the neutral particles, the distance from the production vertex to the cluster position in the ECAL are used together with the cluster time to calculate the speed of the neutral particle. The EB assigns the photon ID to the clusters that have β greater than 0.9. The ones with β less than 0.9 are assumed to be neutrons.

The CLAS12 EB relies heavily on the CCDB database because there are several run-dependent variables that affect particle identification. More specifically, EB uses constants that are unique to the various detectors and subsystems.

- Electron sampling fraction fit parameters for mean and standard deviation
- Photon sampling fraction
- User-determined software trigger
- PID Hypotheses
- Target Position
- Detector Hit Position Resolutions
- Detector Timing Resolutions
- Cherenkov Counter Photoelectrons

In COATJAVA, the reconstruction service in the CLARA framework, the data is stored in the form of HIPO output banks. Each major subset of banks corresponds to an individual reconstruction service engine. The EB contains a specially designed series of banks. This network of banks creates a way in which data analysts can associate particles, whose tracks can originate in the DC, CVT, or FT, and their associated detector hits. FIG. 23 shows the contents of REC::Particle and FIG. 24 shows the contents of REC::Cherenkov, which is an example of one of the detector banks when hit and tracks become associated.

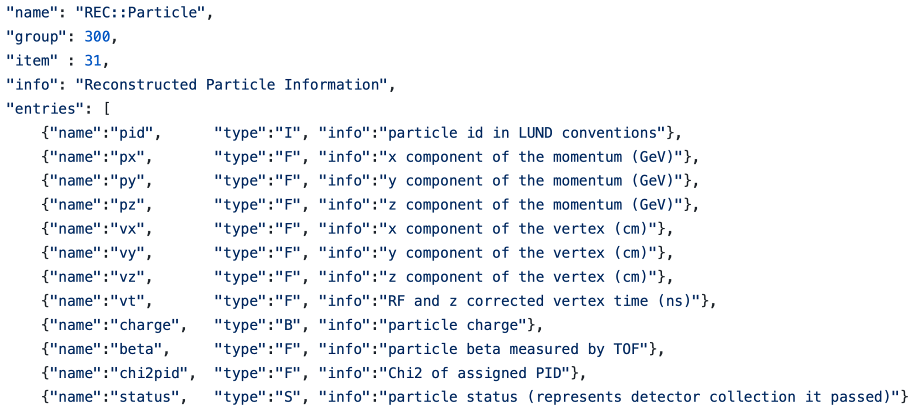

```
"name": "REC::Particle",
"group": 300,
"item" : 31,
"info": "Reconstructed Particle Information",
"entries": [
    {"name":"pid",      "type":"I", "info":"particle id in LUND conventions"},
    {"name":"px",       "type":"F", "info":"x component of the momentum (GeV)"},
    {"name":"py",       "type":"F", "info":"y component of the momentum (GeV)"},
    {"name":"pz",       "type":"F", "info":"z component of the momentum (GeV)"},
    {"name":"vx",       "type":"F", "info":"x component of the vertex (cm)"},
    {"name":"vy",       "type":"F", "info":"y component of the vertex (cm)"},
    {"name":"vz",       "type":"F", "info":"z component of the vertex (cm)"},
    {"name":"vt",       "type":"F", "info":"RF and z corrected vertex time (ns)"},
    {"name":"charge",   "type":"B", "info":"particle charge"},
    {"name":"beta",     "type":"F", "info":"particle beta measured by TOF"},
    {"name":"chi2pid",  "type":"F", "info":"Chi2 of assigned PID"},
    {"name":"status",   "type":"S", "info":"particle status (represents detector collection it passed)"}
```

FIG. 23. The contents of the REC::Particle bank

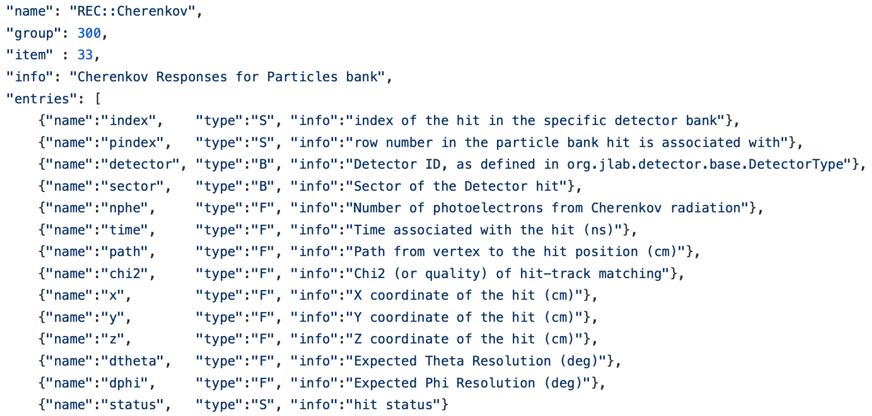

```
"name": "REC::Cherenkov",
"group": 300,
"item" : 33,
"info": "Cherenkov Responses for Particles bank",
"entries": [
    {"name":"index",    "type":"S", "info":"index of the hit in the specific detector bank"},
    {"name":"pindex",   "type":"S", "info":"row number in the particle bank hit is associated with"},
    {"name":"detector", "type":"B", "info":"Detector ID, as defined in org.jlab.detector.base.DetectorType"},
    {"name":"sector",   "type":"B", "info":"Sector of the Detector hit"},
    {"name":"nphe",     "type":"F", "info":"Number of photoelectrons from Cherenkov radiation"},
    {"name":"time",     "type":"F", "info":"Time associated with the hit (ns)"},
    {"name":"path",     "type":"F", "info":"Path from vertex to the hit position (cm)"},
    {"name":"chi2",     "type":"F", "info":"Chi2 (or quality) of hit-track matching"},
    {"name":"x",        "type":"F", "info":"X coordinate of the hit (cm)"},
    {"name":"y",        "type":"F", "info":"Y coordinate of the hit (cm)"},
    {"name":"z",        "type":"F", "info":"Z coordinate of the hit (cm)"},
    {"name":"dtheta",   "type":"F", "info":"Expected Theta Resolution (deg)"},
    {"name":"dphi",     "type":"F", "info":"Expected Phi Resolution (deg)"},
    {"name":"status",   "type":"S", "info":"hit status"}
```

FIG. 24. The contents of the REC::Cherenkov bank

CHAPTER 4

TORUS FIELD MAPPING PROJECT

4.1 OVERVIEW

Successful reconstruction of charged particles in the Forward Detector (FD) of CLAS12 requires a robust track reconstruction software, knowledge of drift chamber (DC) alignment, and precise knowledge of the magnetic field of the Torus. Due to subtle deviations of superconducting coil positions from either installation or manufacturing, there is the possibility that imprecise knowledge of those positions could compromise the resolution of the reconstructed charged tracks. Thus, a project was enacted to measure the Torus field at specific locations particularly sensitive to the field in order to study those field differences from the pre-determined coil movements from field models based off of the ideal coil shapes. Using minimization algorithms, data sets from the measured Torus data and the model Torus data were placed in a chi-squared function. The coil positions were calculated and those results were relayed to the engineers who produced a new full grid for reconstruction.

In order to achieve the benchmarks regarding tracking, the ideal drift chamber position resolution should be approximately 300 micrometers, with the 12-layer chambers located at approximately 2, 3, and 4 meters from the target. The best-case fractional momentum resolution is approximately 0.3% for high-momentum and low-angle tracks such as scattered electrons. The overall goal for the magnetic field measurement is to know the magnitude of the field, regardless of the positional and material aspects of the coils, to 0.1%.

4.2 MEASUREMENT PROCEDURE

The CLAS12 acceptance is rather large for charged particles going in the forward direction; therefore, it is imperative that we understand the field values in all of the acceptance. However, practically, it is not feasible to measure the field in all of the CLAS12 forward detector coverage. The measurement positions have to be situated in an area of the acceptance where the magnetic field is strong and also in a field's region that has been deemed sensitive to deviations of coil positions and shape imperfections. The region most sensitive to those effects is closer to the bore, where the momentum resolution is projected to be the highest due to a stronger magnetic field.

The measurement of the Torus field was accomplished with precise instruments, known as Hall Probes, that were enveloped in holder fixtures that allowed for accurate movement in discrete increments parallel to the beamline and in various fixtures in the XY plane. In the XY plane, there were four positions for each sector (one at a 30 cm radius and three at a 46.5 cm radius). In each of the positions, a Hall probe was inserted and pushed along a fixture that was parallel to the beamline in 5 cm increments, as shown in FIG. 25. LabView software was utilized for data collection and the field strength in cartesian coordinates was monitored in real-time. For each measurement position, a separate Carbon tube provided a path for the Hall probe to slide through. To ensure the reproducibility of the data, the magnetic field mapping team interchanged the tubes and compared the results for each sector.

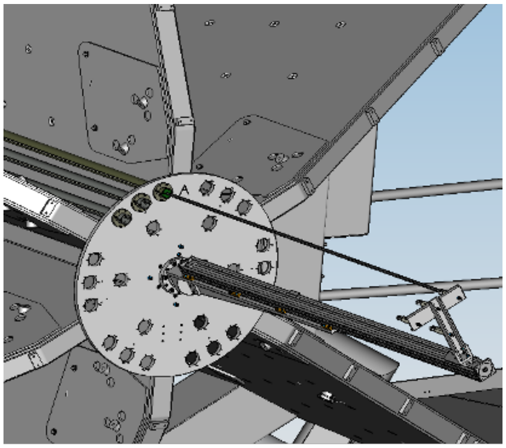

FIG. 25. Visual representation of the field mapping apparatus

4.3 BASIC ANALYSIS OF MEASURED DATA

After the field mapping measurements were finalized in November 2016, basic analysis was done on the raw data to evaluate the data quality, reproducibility, and systematics. In a local coordinate system, the field measurements were analyzed for each sector and cartesian coordinate.

FIG. 26 is an illustration of the coordinate system convention. The weaker, local x-component is perpendicular to the large, local y-component. As shown in FIG. 27-30, the precision varied based on the location of the measurement in the XY plane. Hole A yielded a 0.3% precision among the six sectors and Holes B, C, and D yielded 0.9%, 0.4%, and 0.9% precisions, respectively.

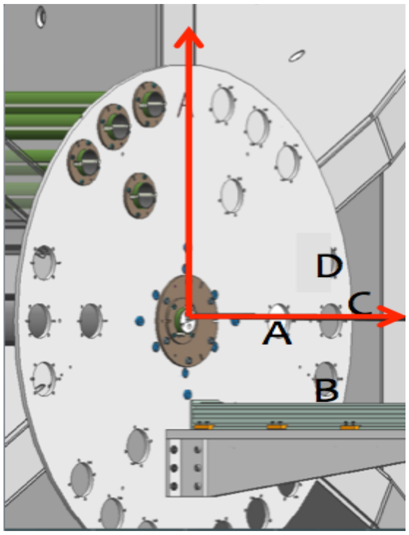

FIG. 26. Explanation of the local coordinate system for field measurements. The x-axis bi-sects each sector (through Holes A and C) and the y-axis is perpendicular.

In addition to the y-component, the x-component of the field is also valuable to look at, as shown in FIG. 31 and FIG. 32. Holes A and C bi-sect each sector, meaning that the x-component of the field should be zero. This constraint is helpful in determining a systematic error, caused by potential, unwanted rotation of the Hall Probes as they slide parallel to the beamline. The analysis displays non-zero values of the x-component at those locations, adding validity to the hypothesis regarding potential rotation of the Hall Probe.

Although this physical motion is small (∼1 degree), it is enough to skew the data. Therefore, a correction to the raw data was implemented by quantifying the angle depending on the x and y components at those positions. FIG. 33 show the dependence of the z-position on the rotation of the Hall Probe in a specific tube.

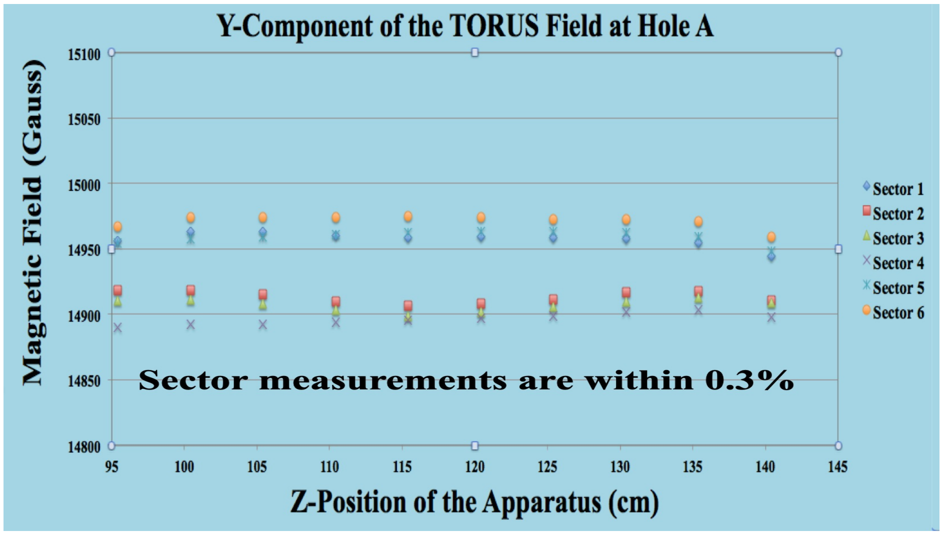

FIG. 27. Hole A Y-component of the field.

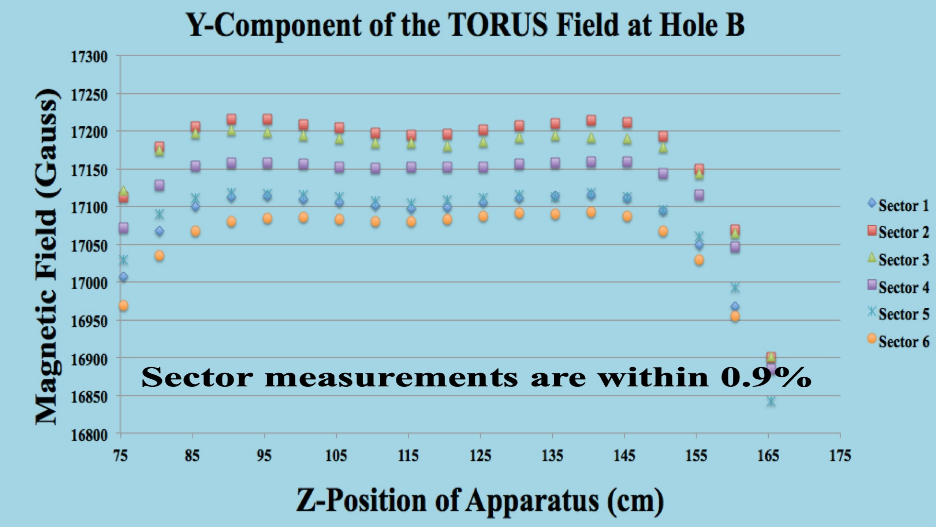

FIG. 28. Hole B Y-component of the field.

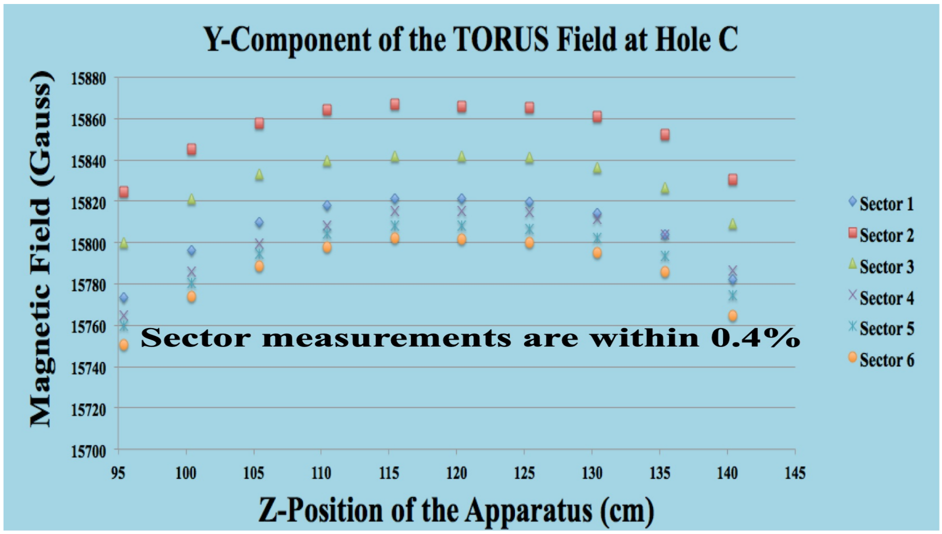

FIG. 29. Hole C Y-component of the field.

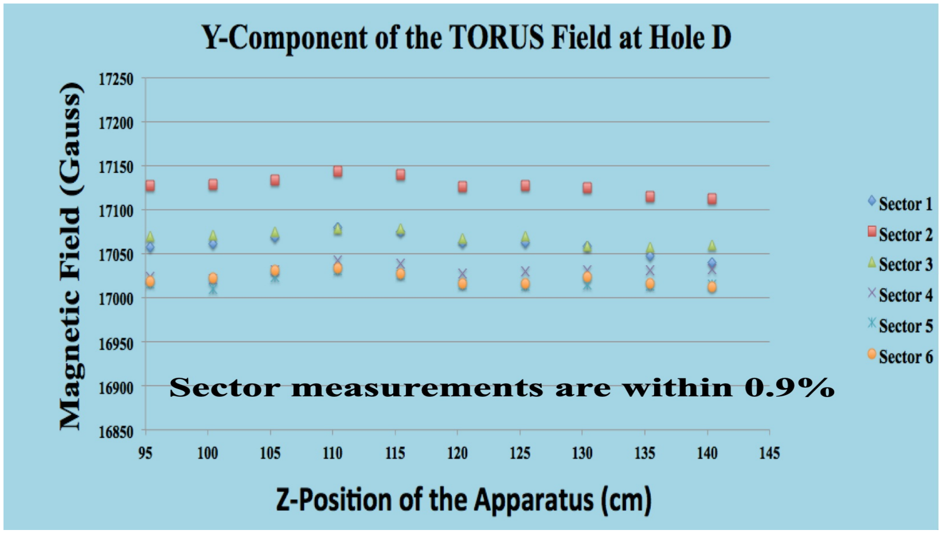

FIG. 30. Hole D Y-component of the field.

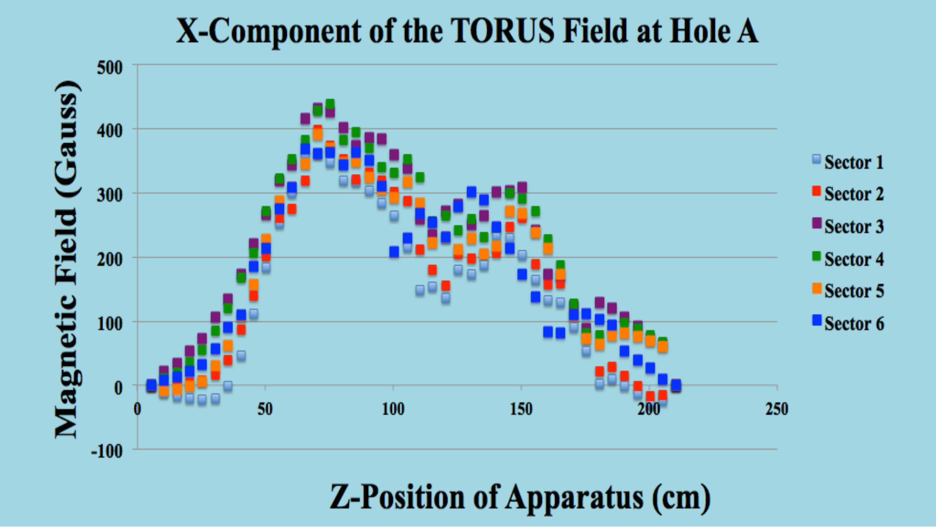

FIG. 31. Hole A X-component of the field.

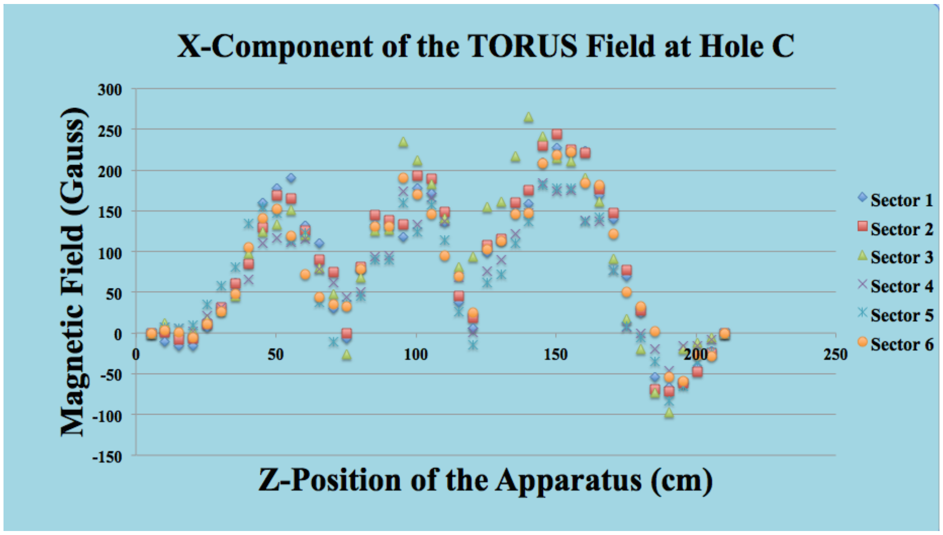

FIG. 32. Hole C X-component of the field.

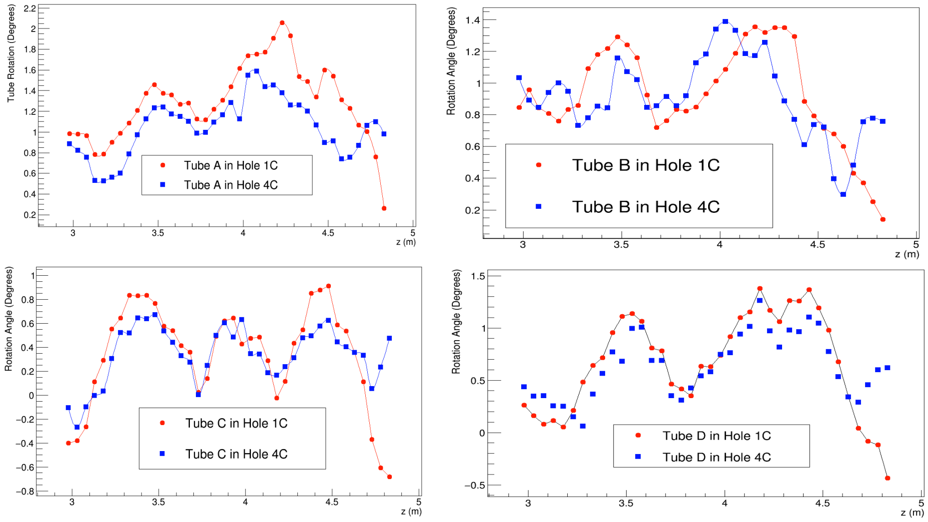

FIG. 33. The rotation of Hall probes in various carbon tubes.

4.4 CALCULATING THE COIL POSITIONS

The fitting procedure is done by minimizing a χ^2 function with 18 α_j parameters for each coil movement (6 coils and 3 degrees of freedom). The degrees of freedom include: motion along the beamline, radial motion away from the hub, and azimuthal motion transverse to the plane of the magnet coil. The α_j coefficients linearly scale with the size of the unit distortion field values. The formalism is displayed by the following sequence of equations, which contain different field model values in each of the measurement positions. The chi^2 function is written as,

$$\chi^2 = \sum_{p=1}^{24} \sum_{i=1}^{3} \frac{\Delta B_{meas}(x_i, p) - \Delta B_{calc}(x_i, p)}{\delta B(x_i)}, \tag{49}$$

while $\Delta B_{meas}(x_i, p)$ and $\Delta B_{calc}(x_i, p)$ are written as,

$$\Delta B_{meas}(x_i, p) = B_{meas}(x_i, p) - B_{ideal}(x_i, p) \tag{50}$$

and

$$\Delta B_{calc}(x_i, p) = \sum_{c=1}^{6} \sum_{j=1}^{3} C\alpha_j [B_{ideal}(x_i, p) - B_{dist}(x_i, p)]. \tag{51}$$

- $B_{meas}(x_i, p)$ is the measured field value reported at the measurement position, p, for one of the cartesian coordinates (x , y, z) denoted as x_1, x_2, and x_3, respectively.

- $B_{calc}(x_i, p)$ is the calculated model-generated field value reported as the measurement position.

- $B_{dist}(x_i, p)$ is the calculated model-generated field that is intentionally distorted by moving one of the six coils (denoted $c = 1$ to $c = 6$) in one of the degrees of freedom (denoted α_1 to α_3).

- $B_{ideal}(x_i, p)$ is the calculated model-generated field at the measurement position in the designed locations where no coils are moved in any direction.

- $\delta B(x_i)$ is the weight applied to each cartesian component, x_i, of the magnetic field value

4.5 FIELD MAP ITERATIONS AND MODEL ADJUSTMENTS

TABLE 1. The first iteration of the fit results (measured in centimeters) using the block model of the Torus coils.

Coil	Radial	Downstream	Azimuthal
A	12.5295	9.9118	0.0748273
B	10.5152	15.6313	0.624114
C	9.38943	13.9002	1.03096
D	8.81748	13.1716	0.079318
E	10.5103	10.673	2.43371
F	12.4902	16.0749	1.76178

Throughout the course of the field mapping analysis, there have been several iterations of the field maps. The details are listed below.

- Extracted coil positions by fitting measured data with the original, block model used until January 2018
- Extracted coil positions by fitting measured data with upgraded model with corrected coil geometry by partitioning the coils into 17 segments with varying current densities in April 2018[36]
- Extracted coil positions by fitting measured data with previous model with an ad hoc correction to the upstream corner in February 2020.
- Extracted coils positions by fitting measured data with coil-dependent geometry without the ad hoc correction to the upstream corner in January 2021.

The results are summarized in Tables 1-4.

TABLE 2. The second iteration of the fit results (measured in centimeters) using the optimized double-pancake model of the Torus coils.

Coil	Radial	Downstream	Azimuthal
A	0.36185	0.217562	0.250904
B	0.311987	1.67751	0.40883
C	0.458769	3.04286	0.728354
D	0.519575	4.36706	0.606732
E	2.21523	2.51131	0.0660279
F	1.68347	0.23668	0.0198553

TABLE 3. The third iteration of the fit results (measured in centimeters) using the optimized double-pancake model as well as an ad hoc correction to the upstream corner.

Coil	Radial	Downstream	Azimuthal
A	0.431708	1.01172	0.609696
B	0.286486	1.76846	1.59645
C	1.3984	0.837393	2.04734
D	3.80696	0.518406	0.876729
E	2.41042	0.775945	1.72266
F	0.758226	0.827278	1.10946

TABLE 4. The fourth iteration of the fit results (measured in centimeters) using the coil-dependent geometry rather than average coil shapes.

Coil	Radial	Downstream	Azimuthal
A	0.715183	2.13879	0.707513
B	0.403613	0.139149	1.51374
C	2.94549	0.737226	1.90719
D	3.25602	1.04489	0.813265
E	3.38049	2.15203	1.62828
F	0.0887242	0.478248	0.909076

4.6 EFFECT OF COIL MOVEMENTS ON FIELD AGREEMENT

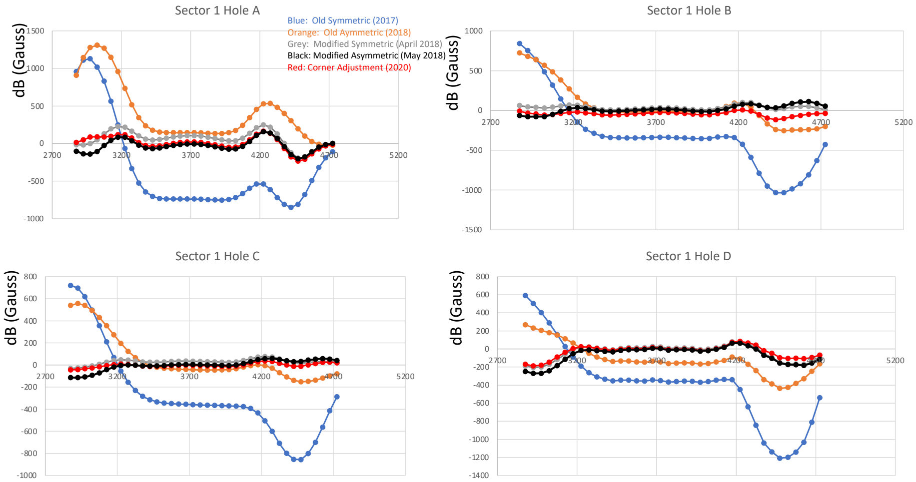

FIG. 34. Sector 1 Field Map/Model Comparison Evolution (2017-2020)

FIG. 34-45 show the difference between the magnitude of the measured field and the model field, as described by the equation below,

$$\Delta B(z_{Hall}) = B_{model}(z_{Hall}) - B_{meas}(z_{Hall}). \tag{52}$$

In each of these plots, there are various iterations of fitting results that are summarized in the previous section. Overall, the trend over time was the production of field models that more closely aligned with what was observed in the measured data from the field mapping procedure.

By combining the detailed analysis of the field, drift chamber alignment, and careful calibration of the DC, tracking resolution can be improved to a satisfactory level for Run Group A. FIG. 46 shows the elastic peak, which should ideally center around the mass of the proton. The mean and width of the elastic peak was quantified as a function of scattering angle and the sector. The improvement between field maps shows the effect of the fitting routine for one of the fitting iterations. The mean value of the elastic peak is closer to its ideal position of 938 MeV, however, there is still a dependence of the peak position on the

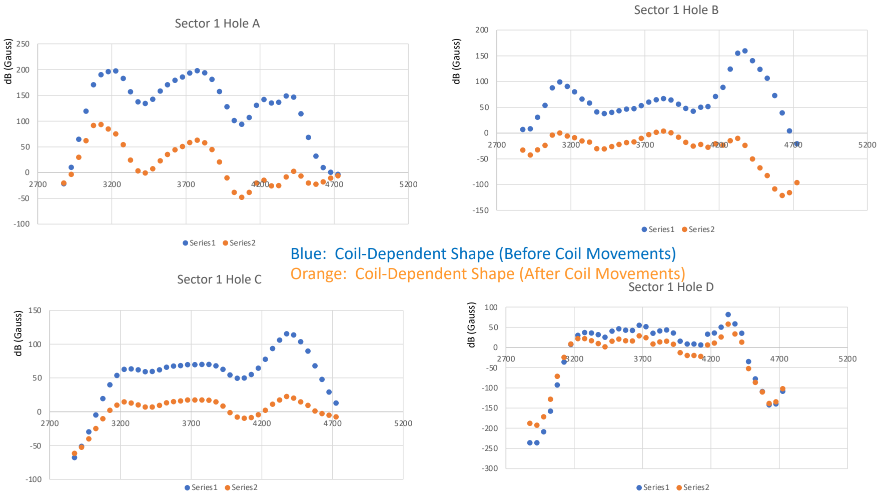

Blue: Coil-Dependent Shape (Before Coil Movements)
Orange: Coil-Dependent Shape (After Coil Movements)

FIG. 35. Sector 1 Field Map/Model Comparison Evolution (2021 Iteration)

scattering angle of the electron. More work is needed to understand this dependence. In terms of the agreement between the latest model and the measured data, the majority of z-position field values fall within 100 Gauss in Hole A (30 cm) and within 50 Gauss in Holes B, C, and D (46.5 cm). Additional studies are for the regions near the coil corners would be ideal to understand the model's depiction coil geometry and how that affects the knowledge of the magnetic field at low scattering angles.

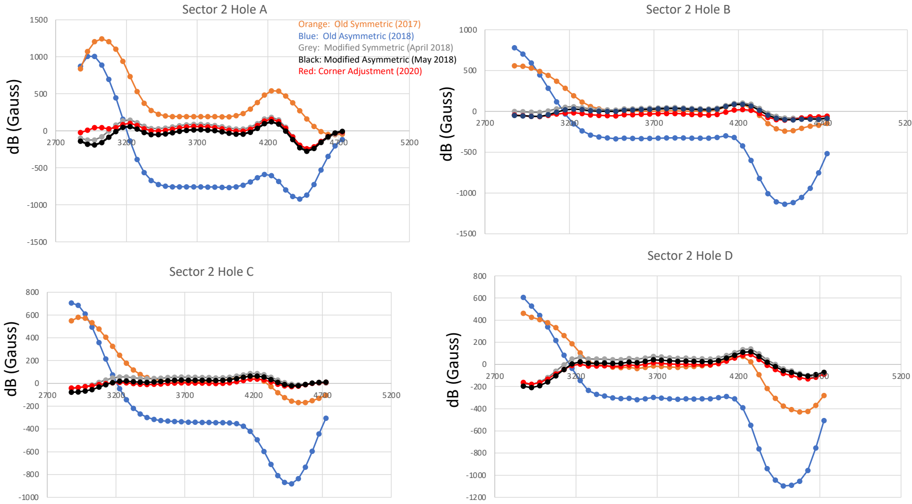

FIG. 36. Sector 2 Field Map/Model Comparison Evolution (2017-2020)

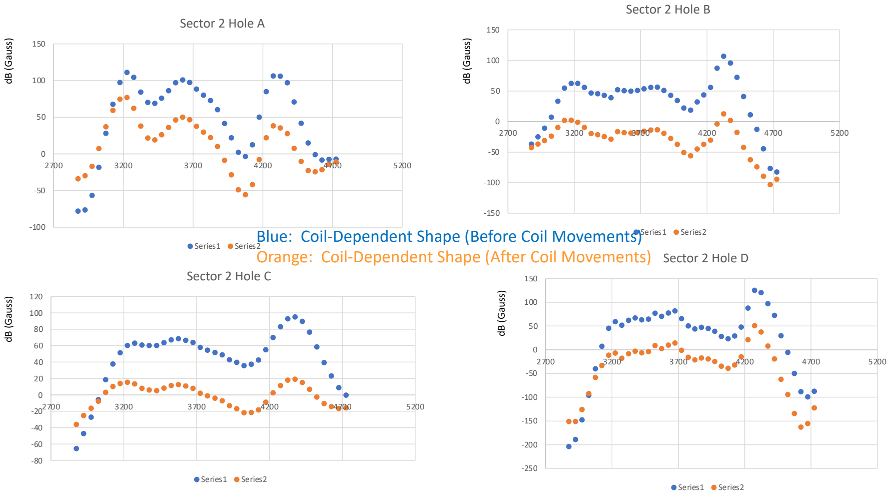

FIG. 37. Sector 2 Field Map/Model Comparison Evolution (2021 Iteration)

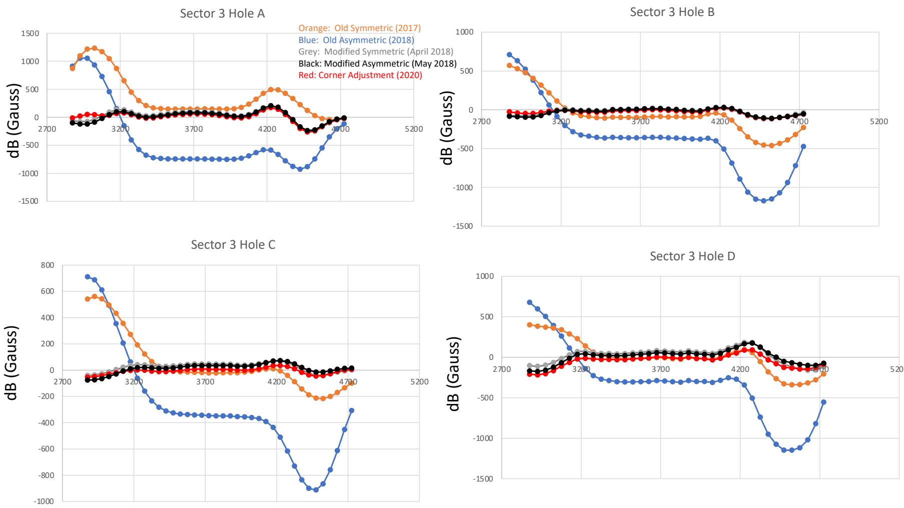

FIG. 38. Sector 3 Field Map/Model Comparison Evolution (2017-2020)

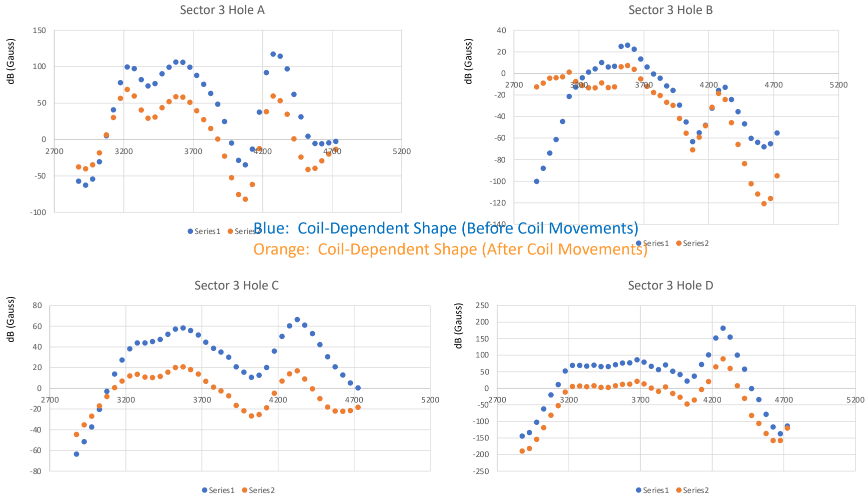

FIG. 39. Sector 3 Field Map/Model Comparison Evolution (2021 Iteration)

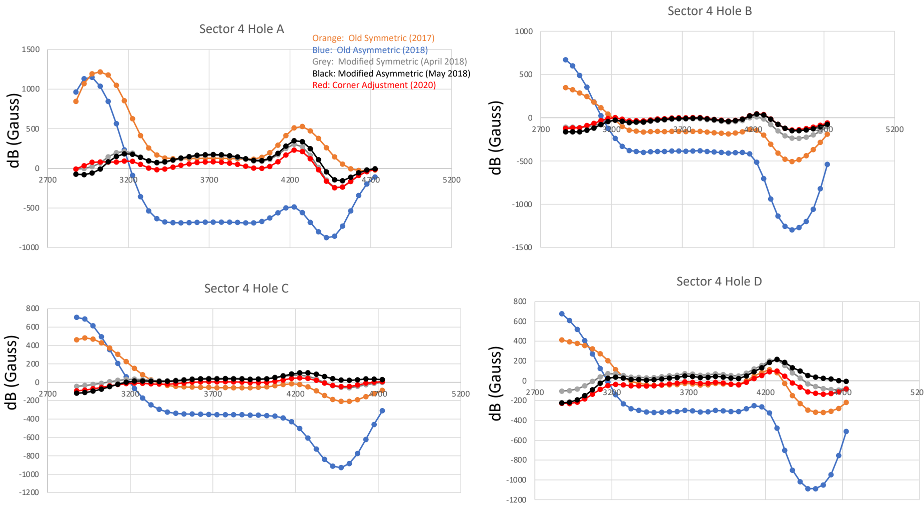

FIG. 40. Sector 4 Field Map/Model Comparison Evolution (2017-2020)

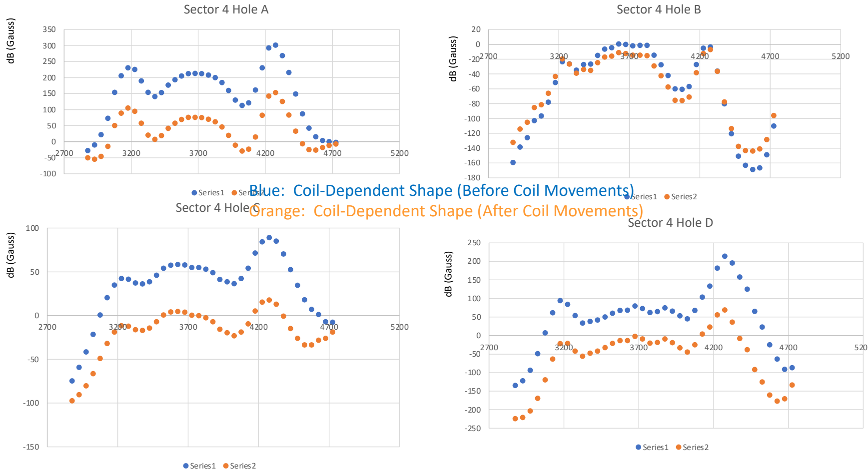

FIG. 41. Sector 4 Field Map/Model Comparison Evolution (2021 Iteration)

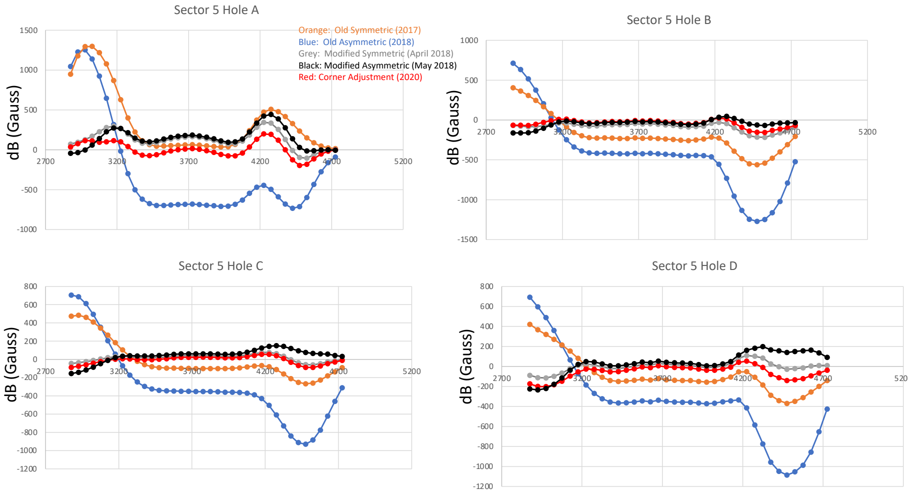

FIG. 42. Sector 5 Field Map/Model Comparison Evolution (2017-2020)

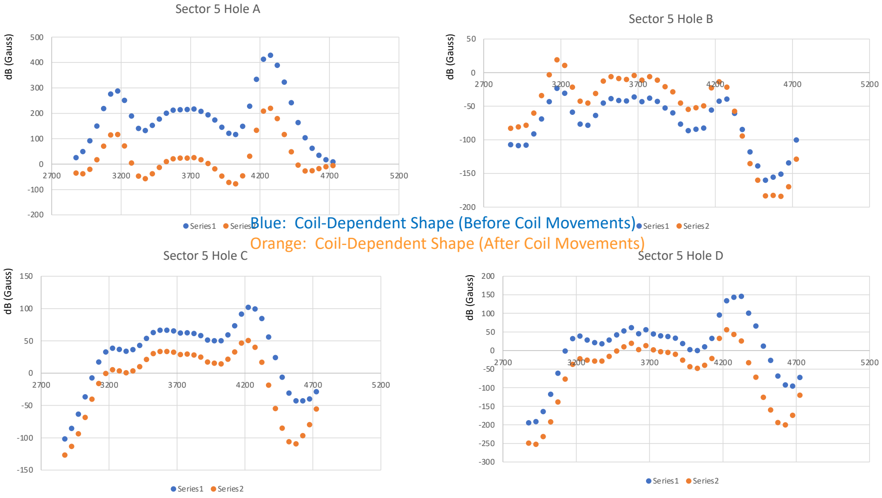

FIG. 43. Sector 5 Field Map/Model Comparison Evolution (2021 Iteration)

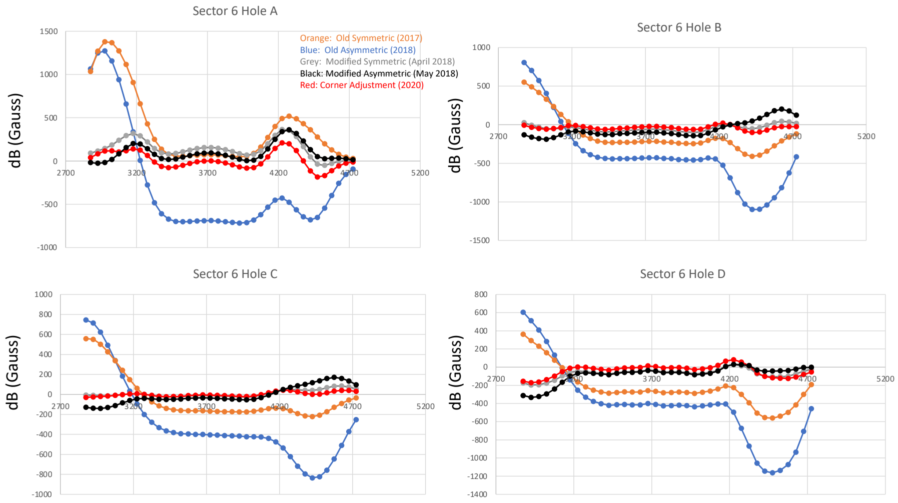

FIG. 44. Sector 6 Field Map/Model Comparison Evolution (2017-2020)

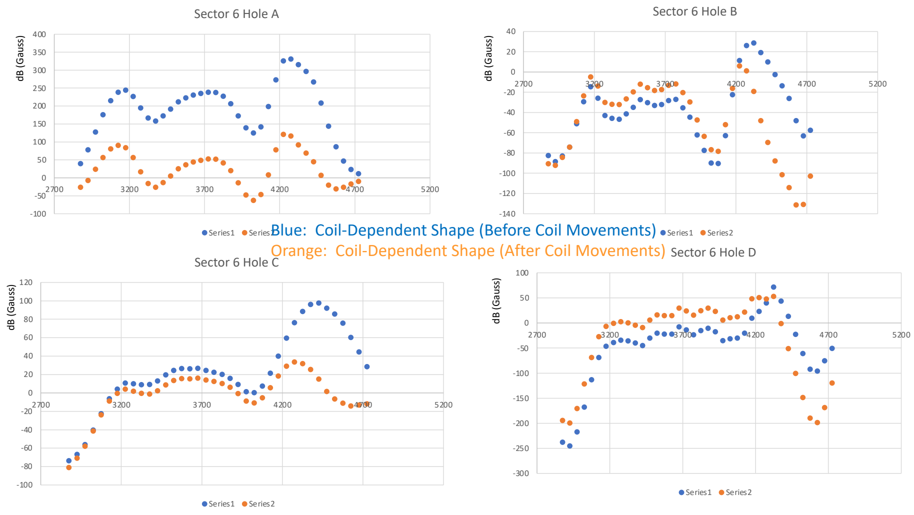

FIG. 45. Sector 6 Field Map/Model Comparison Evolution (2021 Iteration)

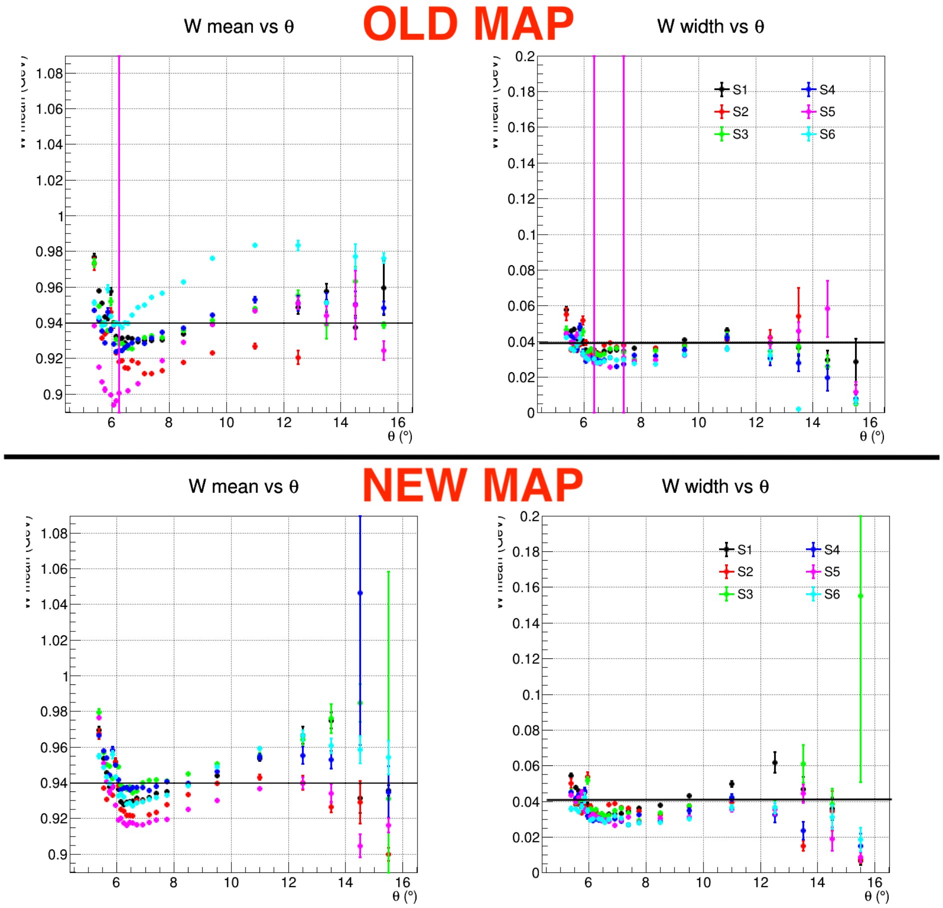

FIG. 46. Effect of 2020 map on elastic peak position and width[37]

CHAPTER 5

J/ψ ANALYSIS FRAMEWORK

5.1 OVERVIEW

This analysis framework's objective is to analyze J/ψ photoproduction events through the reaction, $ep \rightarrow e^+e^-p^{'}X$, where X is the electron that scattered from the liquid Hydrogen target from the incoming electron beam. For the detection of the J/ψ resonance, the invariant mass of the e^+e^- pair is calculated by the following:

$$m_{e^+e^-} = \sqrt{E^2_{e^+e^-} - p^2_{e^+e^-}}. \tag{53}$$

The energy conservation for the total reaction is given by,

$$E_\gamma + m_p = E_{e^+} + E_{e^-} + E_p. \tag{54}$$

This describes the energies of the incoming beam and the target in the initial state with the final state particles and the target, which is the proton, in the final-state. The energy conservation also gives the formula for one of the kinematic observables for the J/ψ cross sections, which is the photon beam energy,

$$E_\gamma = E_{e^+} + E_{e^-} + E_p - m_p. \tag{55}$$

Another observable that is calculated in the analysis is the transferred momentum, $-t$, which is defined as:

$$-t = 2m_p(E_p - m_p). \tag{56}$$

The selection of quasi-real events was done by constraining the kinematics so that photoproduction events with a scattered electron with very forward angles ($\theta \sim 0$) are preserved. In this scenario, $Q^2 \sim 0$. Q^2 is defined in the following way,

$$Q^2 = 2E_b p_{miss}(1 - \cos(\theta_{miss})). \tag{57}$$

For this event selection, the transverse missing momentum components, $\frac{P_x}{P}$ and $\frac{P_y}{P}$, and the square of the missing mass, M_x^2, were calculated to ensure they are very small. The calculations of the missing momentum, missing energy, and missing mass are described by the following formalism where each i-iteration is one of the three final-state particles and E_b is the beam energy. The kinematic variables for the quasi-real event selection are,

$$p_{x,miss} = 0 - \sum p_{x,i}, \tag{58}$$

$$p_{y,miss} = 0 - \sum p_{y,i}, \tag{59}$$

$$p_{z,miss} = E_b - \sum p_{z,i}, \tag{60}$$

$$p_{miss} = \sqrt{p_{x,miss}^2 + p_{y,miss}^2 + p_{z,miss}^2}, \tag{61}$$

$$E_{miss} = E_b + m_p - \sum E_i, \tag{62}$$

and

$$m_{miss}^2 = E_{miss}^2 - p_{miss}^2. \tag{63}$$

5.2 RG-A CONFIGURATION AND DESCRIPTION

Starting in 2018 after the Hall B engineering run, the first major group of experiments began with the resumption of beam operations. This group of CLAS12 experiments was known as Run Group A (RG-A). In Hall B, run groups are joint experiments that share a common experimental set-up, including the magnetic field setting, the target, and beam currents. The J/ψ photoproduction experiment was a part of RG-A and different experiments had to communicate and negotiate the terms of the experiment settings. The overall objective of RG-A was to perform simultaneous measurements for a wide variety of physics topics. In total, RG-A includes 13 experiments that were developed by the CLAS collaboration and approved by Jefferson Lab's Program Advisory Committee (PAC). These experiments are classified into five different sub-categories.

- Deep Exclusive Processes: The objective of these studies is to access Generalized Parton Distributions (GPD's), which are describe correlations between longitudinal and transverse positions of partons. Examples of deep exclusive processes include π^0 production, Deeply Virtual Compton Scattering (DVCS), and deep ϕ production.[38]

- Deep Inclusive and SIDIS: Semi-inclusive deep inelastic scattering is analyzed to establish the kinematic region over which SIDIS pion production can be connected to next-leading-order QCD in terms of parton distributions and parton fragmentation functions.

- Quasi-Real Photoproduction: Using photoproduction, experiments include the study of Timelike Compton Scattering (TCS) and J/ψ photoproduction near threshold. TCS can help enhance the understanding of Generalized Parton Distributions (GPD's) and J/ψ photoproduction can help study the gluonic form factors of the proton.

- Nucleon Structure: These studies analyze the spectrum of N^* states in electroproduction channels, which allows for the study of N^* structure.[39]

- MesonEx Program: The CLAS12 Forward Tagger can be utilized to study the meson spectrum at low Q^2 values. Exotic hybrid mesons, which are quark-antiquark-gluon bound states, are important for the understanding of hadron structure.[40]

To satisfy the physics requirements of these five categories, a series of experimental run conditions were developed. These conditions are related to the configurations of the beam energy, beam current, the DAQ, and the trigger systems. A summary of the run conditions are listed below.

- Torus Magnet: At full field, run with both polarities, with in-bending electrons (75 percent of the time) and out-bending electrons (25 percent of the time)

- Solenoid: At full field

- Beam Current Ranges From 5 nA to 75 nA

- Liquid Hydrogen with occasional data taking on the empty target cell

- Beam Energy: 10.6 GeV (Fall 2018) and 10.2 GeV (Spring 2019)

5.3 DESCRIPTION OF RG-A DATASET

The data analyzed for J/ψ photoproduction consists of different run periods that contain varying experimental configurations, such as the beam energy and the Torus polarity.

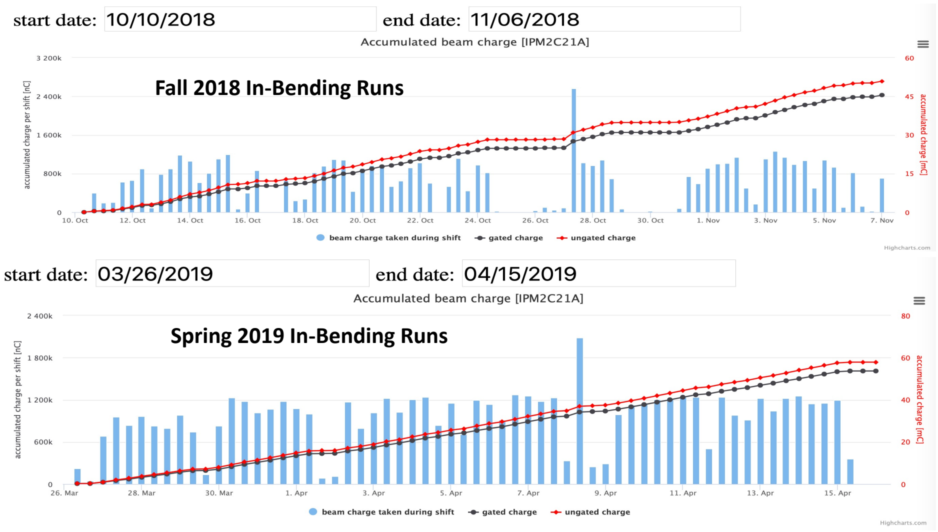

FIG. 47. Gated and ungated accumulated charge for the run periods being analyzed.

Each run consists of a period of time where conditions remain constant. For the purpose of calibration, certain runs were either accepted or discarded depending on the quality of the data and the consistency of the experimental conditions. There are four large groups of datasets that were analyzed for extracting differential and total cross sections for J/ψ photoproduction. The largest dataset was the Fall 2018 in-bending dataset, which ranges from Run 5032-5419. It's total accumulated charge is 45 mC and the set beam energy was 10.6 GeV. The out-bending counterpart for the Fall 2018 dataset was not included due to issues with efficiency. Lastly, a series of runs from the Spring 2019 RG-A period were calibrated and processed. Unlike the Fall 2018 datasets, the Spring 2019 dataset had a set beam energy of 10.2 GeV and consists purely of runs with an in-bending Torus polarity. Since the beam energy was 400 MeV lower, the expected number of detected J/ψ resonances was expected to be lower since the cross section of its production is highest when the beam energy is higher. The accumulated charge associated with the Spring 2019 was 54 mC. FIG. 47 displays the gated and ungated charge plots.

5.4 POST-PROCESSING DATA SKIM

When the run data is processed through the CLARA framework, the data is organized in the form of output banks. The primary banks that are utilized for data analysis are from the

CLAS12 Event Builder (EB). The EB banks consist of four-vector and vertex information as well as the associated detector hits for each of the charged tracks and neutral tracks. However, directly reading the un-altered HIPO files is not a pragmatic task due to the large size of these files. Therefore, an additional post-processing step is necessary after the reconstruction phase of the CLARA framework. A series of data skims filter these HIPO files so that only the relevant physics events are preserved, depending on the experiment of the data analyst's choice. In the case of J/ψ and Timelike Compton Scattering, skim1 is the selected data filter. There are several conditions that the algorithms accept in the skim. They are listed below.

- an electron, positron, and 2 positive particles
- a positive muon, a negative muon, and 1 forward detector proton
- an electron-positron pair with momentum greater than 2 GeV
- an di-muon pair with momentum greater than 2 GeV
- minimum ionizing particle PCAL, ECIN, and ECOUT energy cuts at 0.110, 0.100, and 0.200 GeV, respectively

5.5 ELECTRON AND POSITRON IDENTIFICATION (P $<$ 5 GEV)

The default PID algorithm from the CLAS12 Event Builder, the last stage of event reconstruction, encompasses cut values for various detectors, which have their own calibration constants that affect particle ID. Below the 4.9 GeV/c momentum, the EB identification of electrons and positrons is effective and less susceptible to pion contamination because the HTCC can be used as a veto for any non-electron track whose momentum is less than 4.9 GeV/c. The identification of these particles comes from a combination of information stemming from the CLAS12 DC, ECAL, HTCC, and FTOF.

Firstly, electrons and positrons leave a unique sampling fraction in the ECAL:

$$SF = \frac{E_{total}}{p}. \tag{64}$$

The total energy is the sum of the cluster energies of the three layers of the calorimeter. The momentum of the track is calculated by the DC reconstruction. The values of the mean and width of the total sampling fraction are parametrized as a function of the total energy lost by

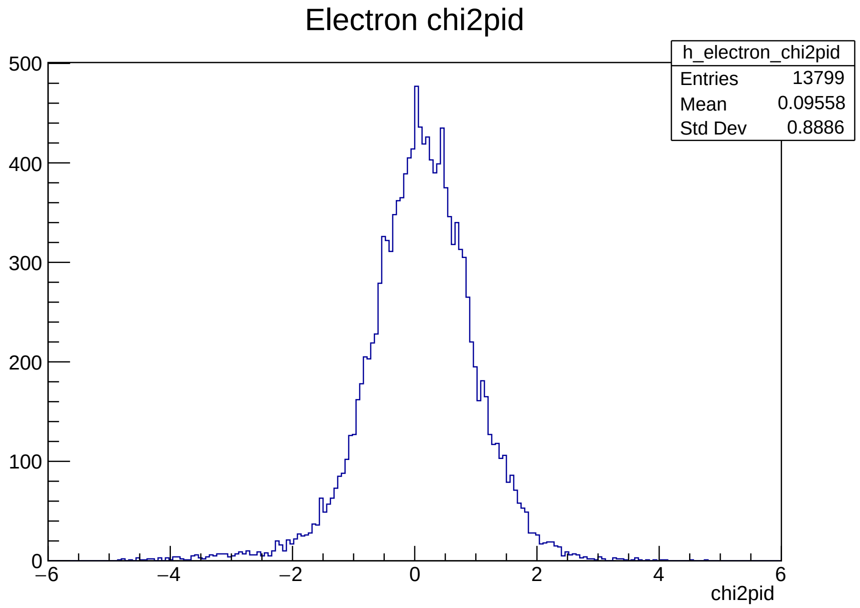

FIG. 48. The electrons and positrons are selected by the CLAS12 event builder and are evaluated by their "chi2pid", which is a measure of how well the sampling fraction compares to the energy-dependent parametrization

the particle in ECAL. Particles whose sampling fractions come within 5 sigma of the expected mean pass the sampling fraction requirement. The electron "chi2pid" value, as shown in FIG. 48, is an event builder quality factor that quantifies how closely the expected and calculated sampling fractions are, as shown by the formula below where σ_p is the resolution of the sampling fraction,

$$\chi^2 = \frac{SF_{meas}(E) - SF_{calc}(E)}{\sigma_p}. \tag{65}$$

The minimum PCAL energy cut provides an additional constraint as electrons and positrons are observed to deposit more than 60 MeV in that layer. This cut provides mitigation of pion misidentification. FIG. 49 displays the PCAL cluster energy of reconstructed electrons from an RG-A data sample in which there are almost no electrons with deposited energy below 100 MeV.

Lastly, the HTCC is involved with the identification of electrons and positrons. These particles leave behind a trail of Cherenkov radiation due to their high speed through material

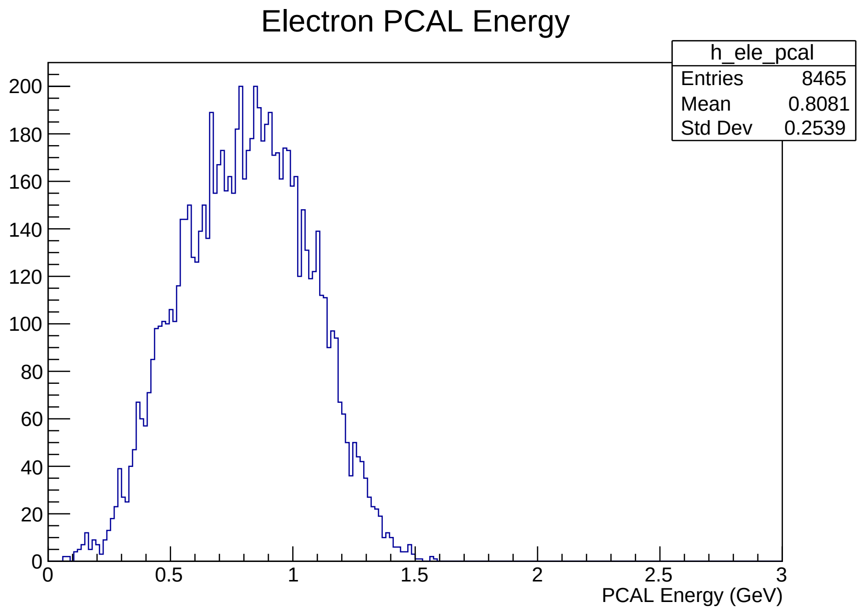

FIG. 49. The electron's energy as measured by the PCAL layer, which shows the 60 MeV minimum energy cut.

at a rate faster than the speed of light in that medium. It takes a minimum of 4.9 GeV to leave a detectable Cherenkov response for the possibility of pion identification. The number of photoelectrons is reconstructed from the analysis of ADC values of HTCC PMTs. A minimum of 2 photoelectrons is needed for e^+e^- ID, as shown in FIG. 50.

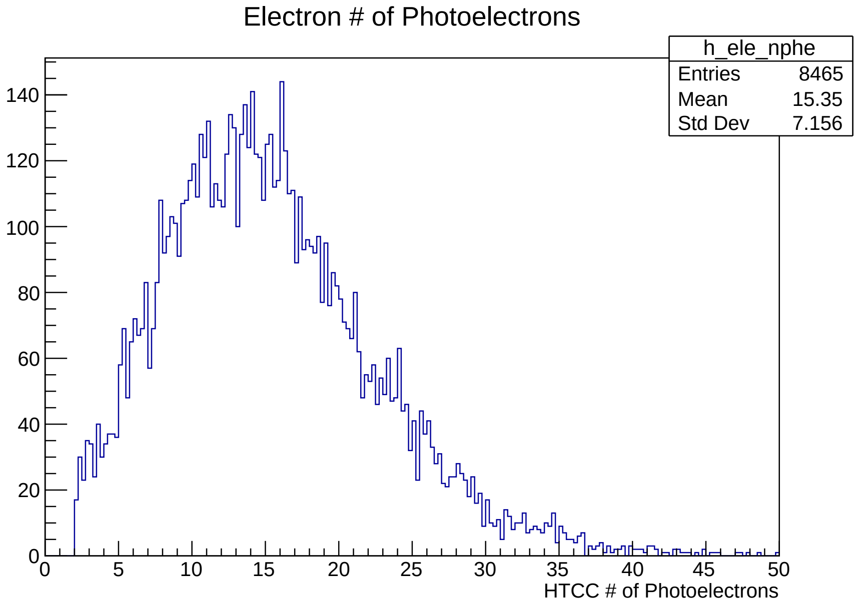

FIG. 50. The number of photoelectrons measured in the HTCC is a requirement for electron and positron identification.

5.6 POSITRON IDENTIFICATION ABOVE 5 GEV

While the standardized CLAS12 Event Builder PID is sufficient for clean identification of electrons and positrons, the rate of pion contamination is higher when momenta go beyond 5 GeV. There are events where a pion can pass the required cuts for electrons/positrons since the values for the PCAL energy, ECAL sampling fraction, and HTCC number of photoelectrons can overlap with a certain percentage of pion events.

Therefore, additional cuts had to be developed to mitigate the probability that a high-energy pion passes through positron ID cuts. This is especially important for J/ψ photoproduction since electrons and positrons can have momenta up to 9 GeV.

Evidence of pion contamination exists in both MC and RG-A data by way of exclusive events and non-exclusive events. In terms of MC data, these effects were studied by simulating single pion events generated beyond 5 GeV. As shown in FIG. 51, the total number of events were compared between the initial MC sample and the number of events with a detected positron. According to this reconstruction, 6% of pions get mis-identified as positrons. This subset of the original reconstructed events was then analyzed to determine key characteristics that could be used to mitigate the contamination observed in RG-A data.

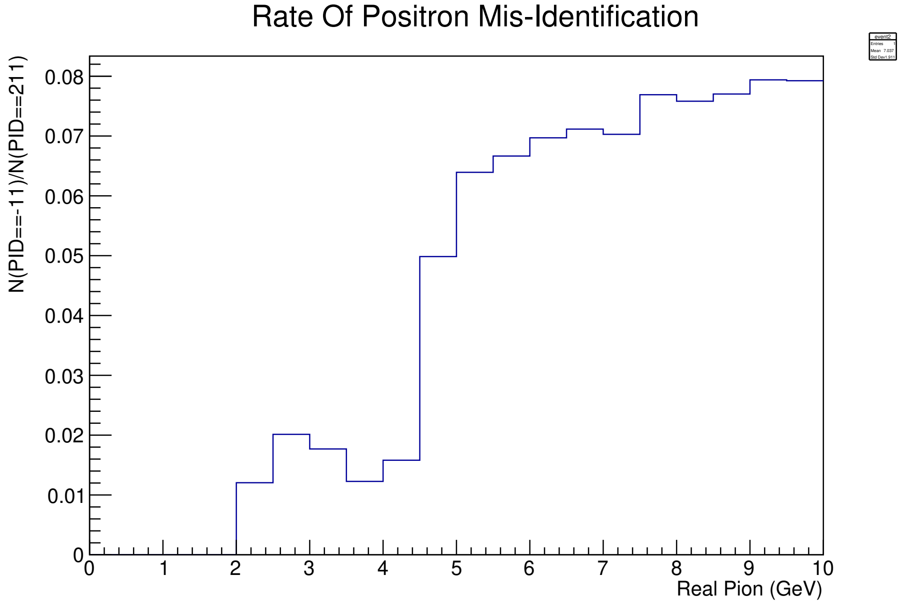

FIG. 51. Using MC data, a comparison between the original generated quantity of high-energy pions and the ones mis-identified as positrons was analyzed.

For the RG-A dataset, there is clear qualitative evidence of pion contamination. For example, the kinematics of the e^+e^-p events were analyzed by observing the scattering angle as a function of momentum, as shown in FIG. 52. The positron's kinematics show that there is a statistically significant cluster of events above 5 GeV. That cluster is due to pions passing the event builder standardized cuts.

Another exclusive reaction that can be studied for the purpose of pion contamination involves the final-state with a pion (identified as a positron) and an electron accompanied by a missing neutron, as shown here:

$$ep = e^{'}\pi^{+}(n) \rightarrow e^{'}e^{+}(n). \tag{66}$$

FIG. 53 contains events, which all contain a reconstructed low-energy (below 4.5 GeV) electron and a reconstructed high-energy positron. The requirement imposed on the electron

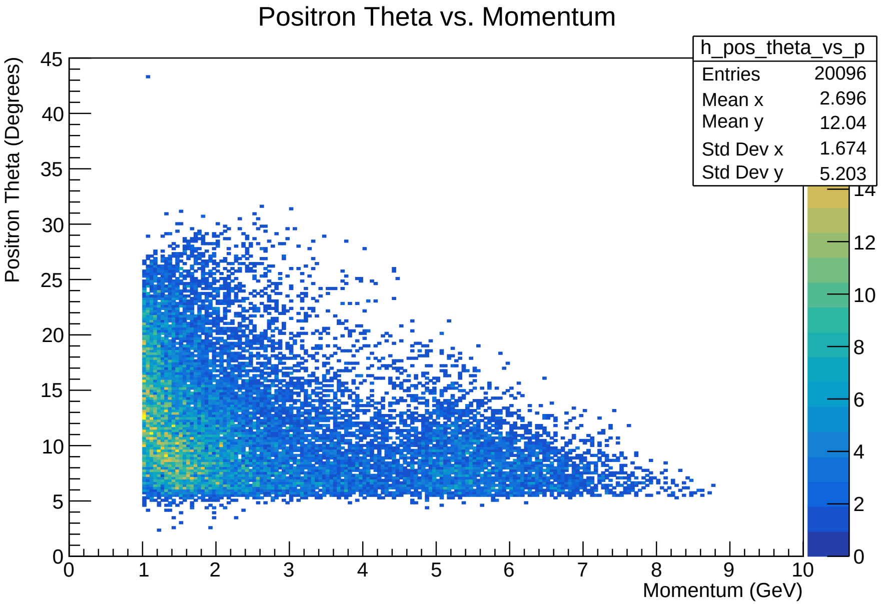

FIG. 52. In the RG-A dataset, the positron scattering angle as a function of the momentum was analyzed and a visible cluster of events above 5 GeV indicate pion contamination at that energy range.

was motivated by the need to ensure that the electron's identity is certain. By having the momentum below 4.5 GeV, the ambiguity over pion contamination is lessened. The missing mass was calculated by assigning the pion mass to the positron. The visible peak above the background is a clear indication of pion contamination in the identified positron sample of the RG-A dataset.

Studies were done for the responses from ECAL regarding both the longitudinal and lateral shower profiles for individual layers for the purpose of developing additional criteria for positron identification and increasing the probability of a true positive ID. For instance, the PCAL sampling fraction contains observable distinctions between the response due to a pion and one due to a positron. The rejection power can be further enhanced by measuring the 2D profile of the ECIN sampling fraction vs. the PCAL sampling fraction, as shown in FIG. 54. Such a cut, $SF_{ECIN} = 0.2 - SF_{PCAL}$, can reject a significant fraction of pions while preserving positrons.

Lateral shower profile quantities such as the number of strips in the cluster(for U, V, W views) were studied for the purpose of distinguishing positrons and pions. Even though

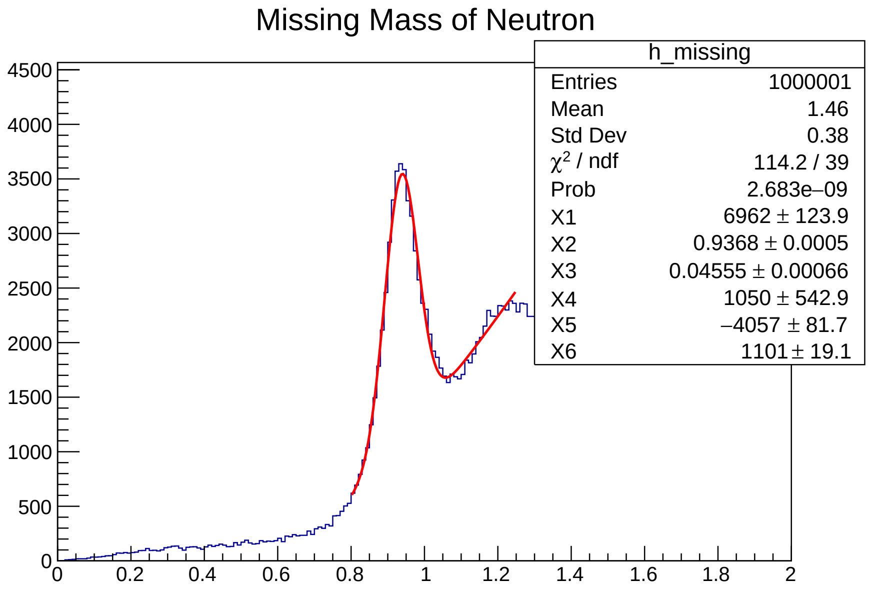

FIG. 53. Missing neutron peak, which is used to estimate mis-identified positrons

a fraction of high-energy pions may share the same sampling fraction as a positron, the number of strips hit have different distributions for each view and layer, as shown in FIG. 55. High-energy pions tend to leave wider distributions for the number of strips hit (labeled DU, DV, and DW in the EB) than that of positrons. Therefore, these offer pion rejection power.

Second moments, Eq. (55), were also analyzed among samples of positrons and pions that were mis-identified as positrons. As observed in the deposited number of strips, 2nd moments showed differences between the two datasets, corroborating the usage for pion rejection cuts. As displayed in FIG. 56, each layer of the calorimeter shows a wider 2nd moment distribution for pion showers than for showers left behind by positrons:

$$M_2 = \frac{\sum (x-D)^2 ln(E)}{\sum ln(E)}. \tag{67}$$

Using the exclusive reaction with the missing neutron, the pion rejection power of these combination of cuts can be studied. Starting with no additional cuts and only the standard event builder cuts, it is observed that these additional cuts for positrons reduces the number of missing neutrons by several factors, as shown by FIG. 57.

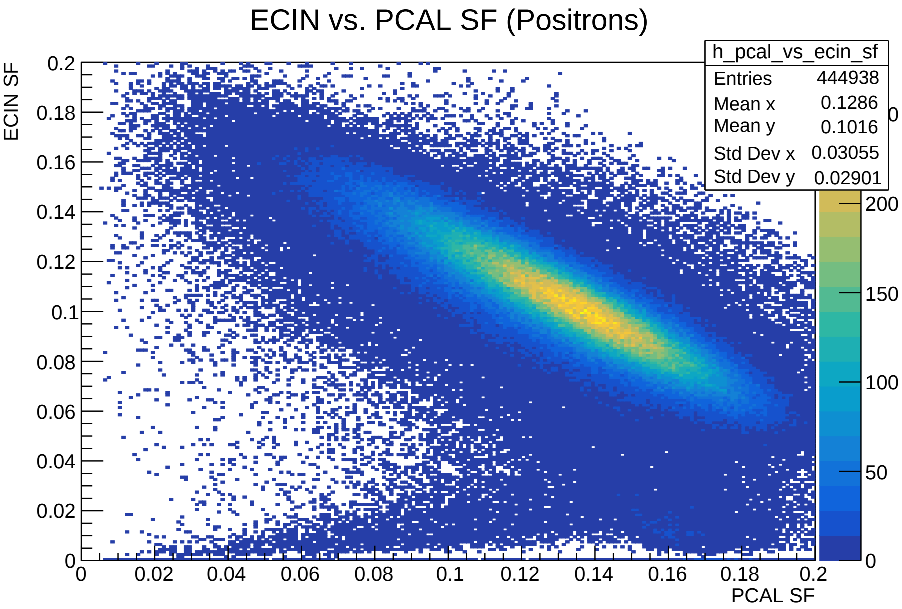

FIG. 54. The correlation between the ECIN sampling fraction and the ECOUT sampling fraction was determined

Machine learning, in the form of multi-variate analysis, is an effective tool for distinguishing signal vs. background events when the algorithm is trained with reliable data where there is a clear distinction between the two.

In addition to the CLAS12 Event Builder, the ROOT TMVA package can allow various observables such as the ECAL sampling fractions and the 2nd moments to determine the optimal cut value by calculating the probability that a candidate particle is a signal (positron) or background (pion). The ROOT TMVA package contains a robust framework for machine learning. Machine learning, which is a large component of artificial intelligence, provides the ability to train algorithms to make autonomous decisions based on aspects of pattern recognition. Therefore, the intelligence of a machine learning method is dependent on the quality of the training data. MC datasets for positron events and pion events (mis-identified as positrons) provided the machine learning algorithms with training input data. Using the training sample, the ROOT TMVA package allowed for the calculation of classifier cut efficiencies, ROC curves, and statistical correlation plots. The normalized signal and background distributions are displayed in FIG. 58. The distributions are the input parameters

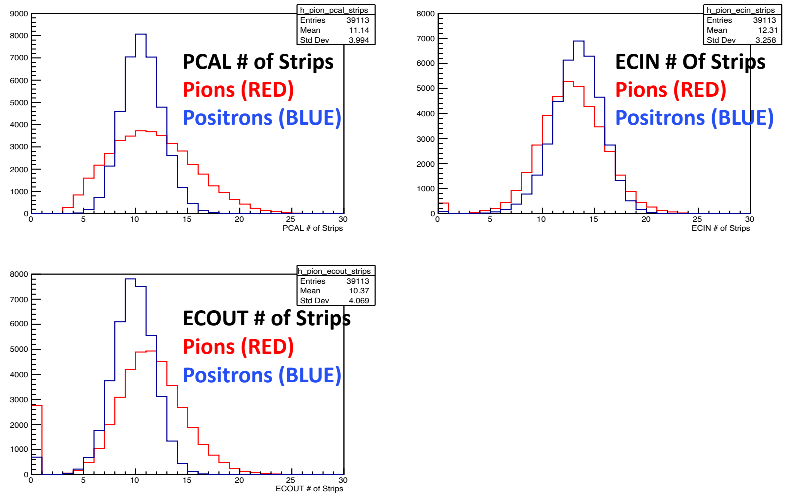

FIG. 55. The number of strips hit in layer of the calorimeter were analyzed for both real positrons (blue) and mis-identified pions (red).

that the MVA relies on to calculate an aggregate MVA cut value that is studied for efficiency.

The input parameters chosen were the PCAL sampling fraction, the ECIN sampling fraction, the ECOUT sampling fraction, the 2nd moment sum for PCAL, ECIN, and ECOUT. The number of strips were not included in the MVA training because there is a linear correlation between the number of strips and the 2nd moment for each view of each layer of the ECAL. Generally, it is good practice to eradicate unnecessary, correlated variables in machine learning.

The ROOT TMVA package contains tools for statistical analysis regarding classifier methods, such as the likelihood, Boosted Decision Tree, or multi-layer perceptron algorithms. Receiver operating characteristic (ROC) curves were created to assess each MVA algorithm's ability to reject background and enhance efficiency. Curves towards the upper right portion of the canvas represent the most robust methods. One of those methods was the Boosted Decision Tree (BDT).

The BDT method was analyzed using a training sample of signal (real positrons from MC) and background events (mis-identified pions from MC). The signal efficiency, the background rejection, and the significance curves are superimposed in FIG. 59. The green curve, which represents the significance, was analyzed to find the maximum value. The BDT cut value that corresponded with the maximum value was -0.01. This indicates that applying that cut

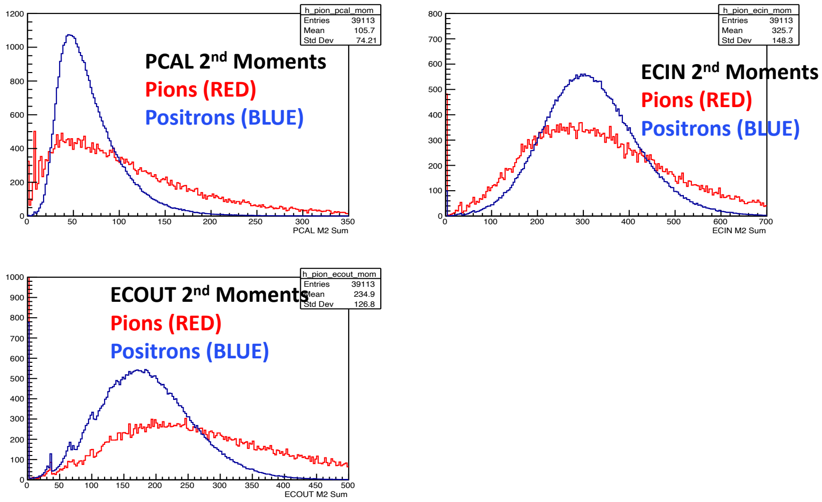

FIG. 56. The second moments in each layer of the calorimeter were analyzed for both real positrons (blue) and mis-identified pions (red)

value would reject large amount of pions while preserving the vast majority of positrons.

The MVA BDT cut that was optimized through training samples can be further investigated by utilizing exclusive reactions, such as the missing neutron peak and analysis of the invariant mass near the J/ψ peak. The neutron peak yield is proportional to the amount of mis-identified positrons (or the background) and the J/ψ yield is proportional to the signal strength. From an experimental point-of-view, quantifying the J/ψ peak above the background is a secure strategy for measuring the amount of positron events. By varying the BDT cut value, these quantities can be studied for systematic effects. As shown in FIG. 60, the BDT cut value of -0.01 is a valid place to apply the positron ID due to the high background rejection with simultaneous signal efficiency. In FIG. 61 a normalized ROC curve, showing the background rejection (missing neutron peak strength) and signal efficiency (the number of J/ψ events) observed in the RG-A dataset, indicates a robust classification method.

For the analysis of J/ψ photoproduction, only advanced MVA cuts were applied on positrons with momenta above 5 GeV in the final-state reaction. For electrons, only cuts that are based on the CLAS12 Event Builder are utilized. This is because π^- contamination is not prevalent in the phase space that is analyzed for this study. In addition, the lepton number conservation places constraints on the final reaction. When there are well-identified lower energy positrons, the higher energy corresponding negative particles have to be electrons.

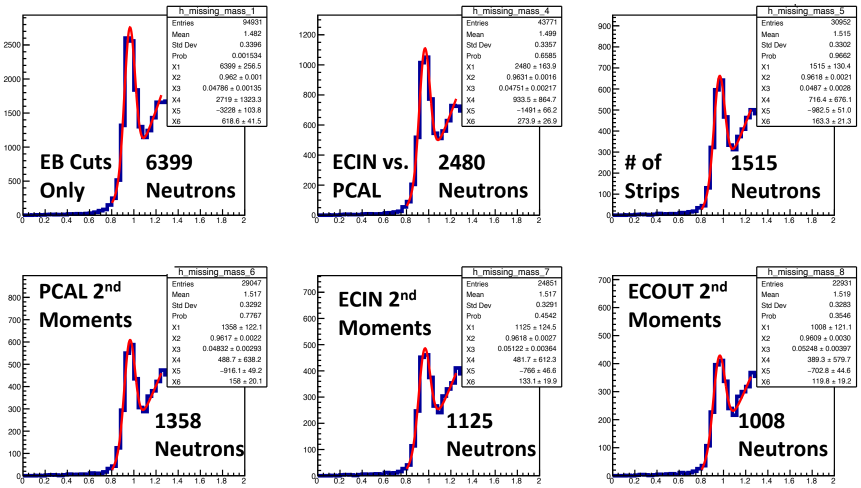

FIG. 57. Gaussian distributions on top of the background were fitted to the peaks to quantify the number of neutrons as a benchmark for pion-positron rejection

Therefore, the likelihood of π^- contamination is very low.

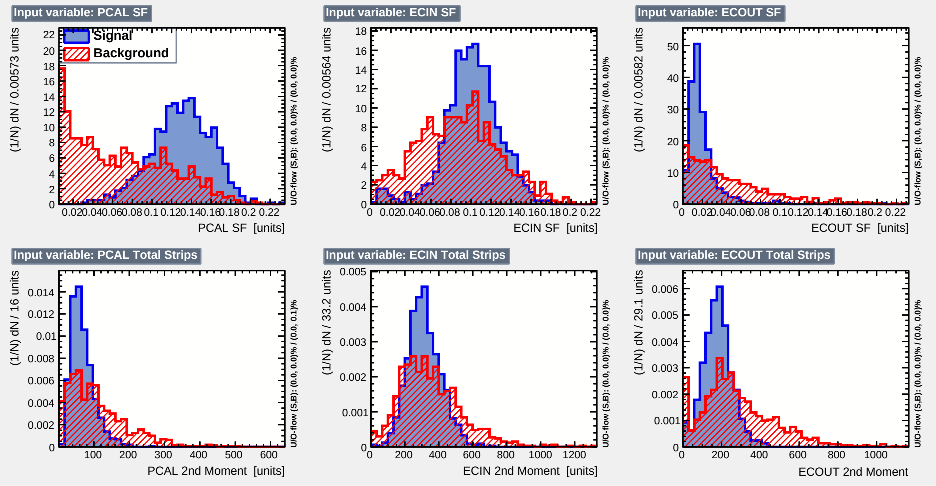

FIG. 58. As displayed by the ROOT TMVA GUI, the input training variables were normalized and used to allow MVA algorithms to determine efficiency cuts for the purpose of classifying signals and backgrounds

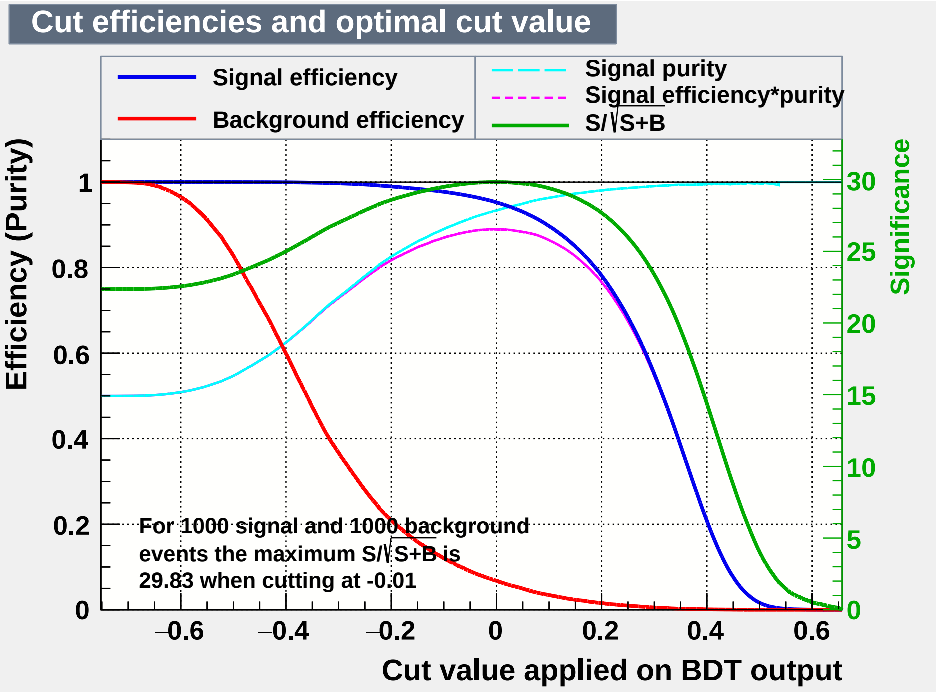

FIG. 59. The Boosted Decision Tree (BDT) was analyzed for both the background and signal efficiency to determine the optimal cut for classification.

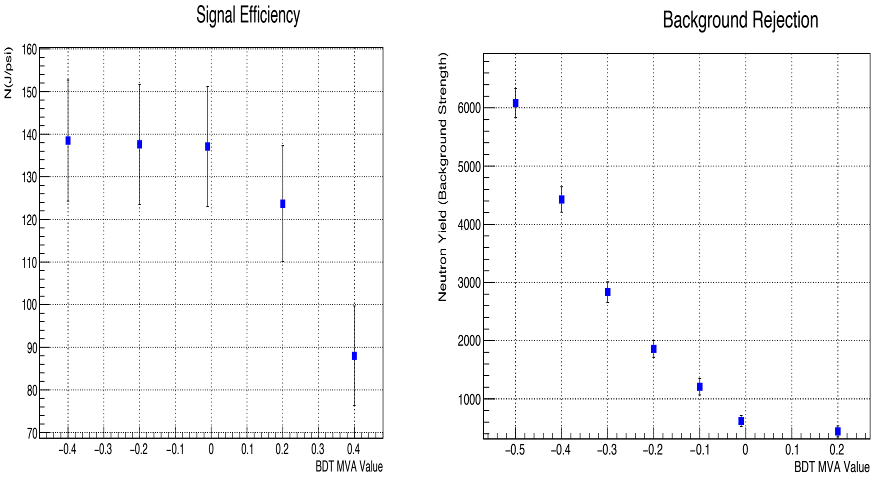

FIG. 60. Effect of the advanced positron ID cuts on J/ψ yield and the number of neutrons in the resonance.

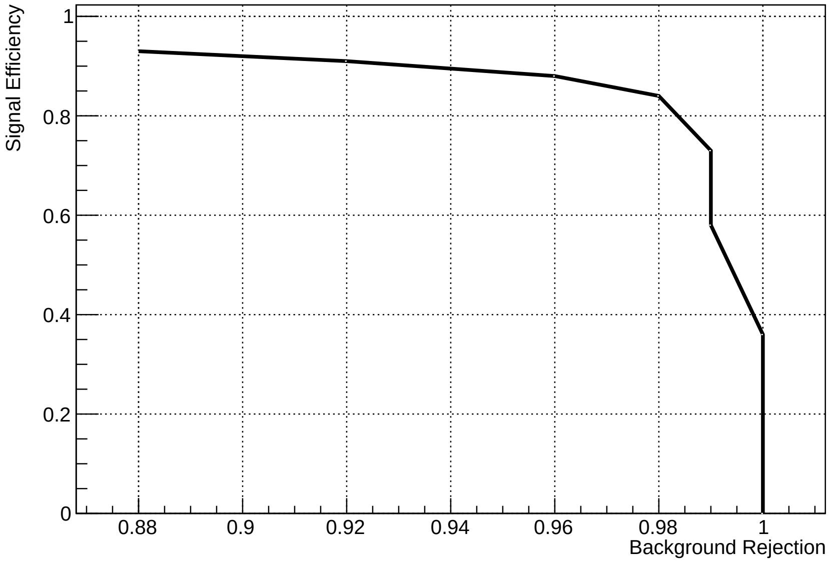

FIG. 61. ROC curve from signal and background from RG-A positron ID analysis.

5.7 PROTON IDENTIFICATION

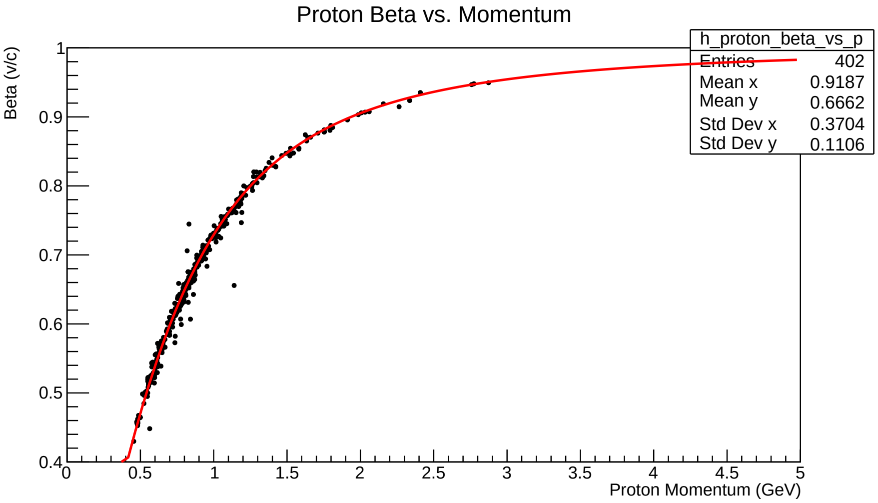

FIG. 62. Using FTOF and DC to quantify the beta vs. momentum for PID.

In addition to electron and positron identification, accurate proton identification is necessary for the measurement of the J/ψ cross section, as well as other observables. Due to the kinematical constraints of J/ψ photoproduction, the scattering angle of the proton is low enough that nearly all prospective recoil proton end up in the CLAS12 forward detector. The advantage to this is that the CLAS12 forward detector has better tracking angular and momentum resolutions as well as good timing resolution from FTOF. Detecting hadrons, such as protons, requires the calculation of the speed as a function of momentum. The momentum is calculated by the DC tracking from the curvature of the track in the presence of the magnetic field. The speed, or beta of the track, can be known due to the fact that the pathlength is calculated by the DC tracking and the time-of-flight of the proton is calculated by FTOF's reconstruction, as shown in FIG. 62. Depending on the location of the hit, the resolution in FTOF will varies, which affects the quality of the proton PID.

For the purpose of J/ψ photoproduction analysis, protons are identified using the standardized CLAS12 Event Builder cuts. In the CLAS12 event builder, the measured vertex time (based off of the FTOF information) is compared to the expected vertex time (for various hadrons). If the closest match for those vertex times is the proton, then the final PID

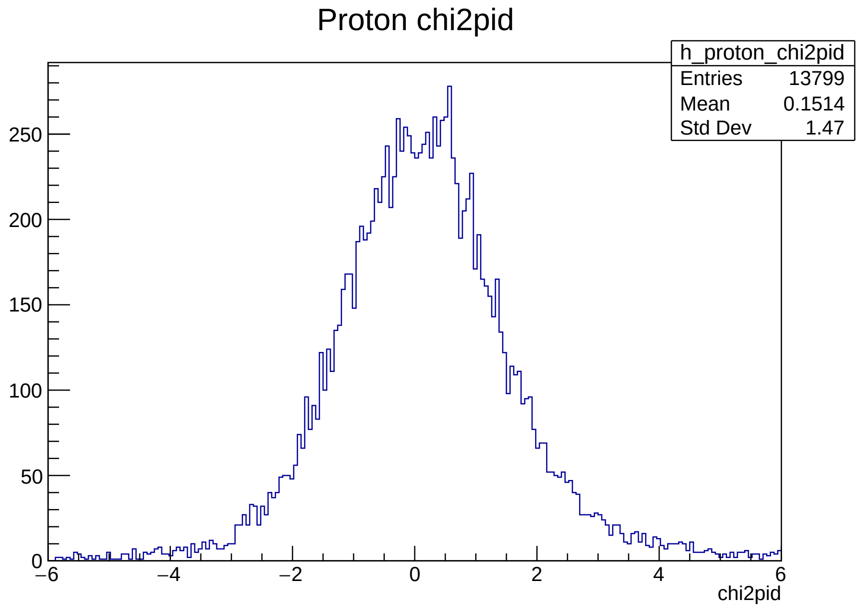

FIG. 63. The CLAS12 event builder preserves hadrons' "chi2pid" value for hadron ID quality.

value will indicate that it is 2212, the numeric identity for a positive proton identification. In addition to the PID hypothesis, the CLAS12 Event Builder also assigns a value called chi2pid, which is a quality factory based off of the difference of the vertex times and the expected timing resolution, which is dependent on the FTOF layer and component. This is shown in FIG. 63

5.8 RADIATED PHOTONS FROM ELECTRONS AND POSITRONS

Calculations that involve the momenta of the electron-positron pair, such as the invariant mass, can be sensitive to the effects of radiative energy loss by the electrons and positrons. As the electrons move from the vertex to the CLAS12 FD, energy can be lost from radiation at the vertex in the target, in the scattering chamber, on the materials of the SVT closure, HTCC windows, and mirrors - essentially any material that precedes the drift chambers. The fraction of radiated photons will be detected in the ECAL and the ones that have been radiated before the electron reaches the drift chambers can be easily identified. The measured energy of the radiated photons can be used to reconstruct the momentum of electrons and positrons at the production vertex. It is important to take this effect into

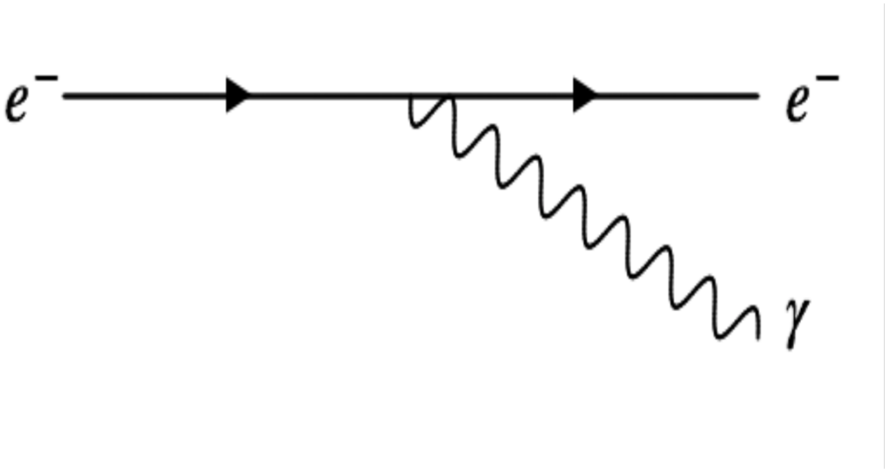

FIG. 64. A visual representation of the loss of energy by the radiation of photons from the original particle.

account, so that events could be preserved for correct exclusivity cuts and correct invariant mass measurements.

Photons are detected by identifying hits in ECAL that are unassociated with track in the DC. For the selection of radiated photons in J/ψ analysis, a 0.7 degree cut is applied to the difference between the polar angle of the electron (or positron) and a photon reconstructed by ECAL. As shown in FIG. 65, these events were observed in the RG-A dataset by analyzing the difference in polar and azimuthal angles, as well as the momenta. In addition, insight into the sources of radiation from the interaction of the electrons, which are in proximity to the target and Solenoid field, can be analyzed by studying the effect of the electron momentum on the difference in phi angle between the electron and the photon. This is illustrated in FIG. 66, which clearly indicates the presence of three bands of radiation.

Another consideration that has to be made is that not all radiative photons are identified as photons in the CLAS12 event builder. Neutral particle identification in the event builder involves analysis of un-matched hits in the PCAL/ECAL. In order to discriminate between photons and neutrons, the event builder's PID algorithm relies on the timing information in the calorimeter to calculate the speed of the particle. Due to imperfections in ECAL timing association, some photons are mis-identified as neutrons. Therefore, for the purpose of correcting e^+e^- momenta from radiative photons, it is important to accept any neutral

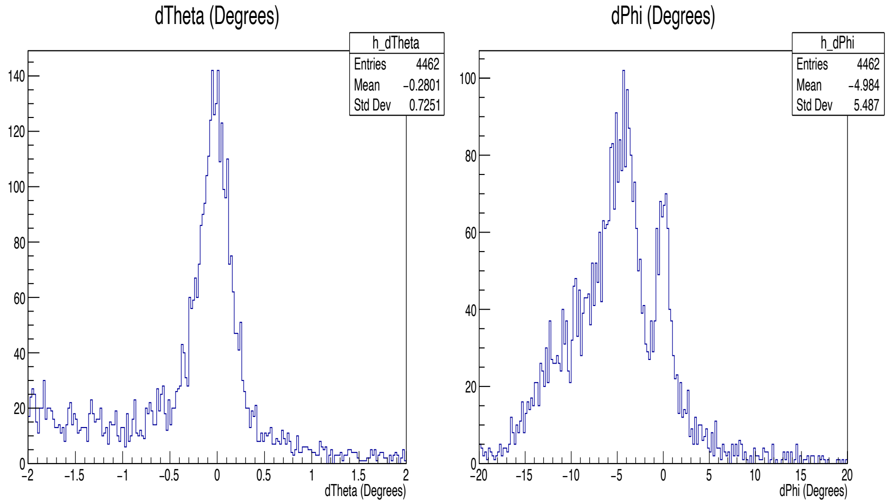

FIG. 65. The difference in the θ and ϕ angles between the original lepton and the photon. The dϕ distribution is after the cut on dθ.

particle, regardless of the event builder PID, that passes the scattering angle difference cut between the presumed photon and the electron/positron. FIG. 67 shows the β vs. momentum distribution for any neutral particle that passes the 0.7 degree cut that is applied between the e^+ or e^- and the associated radiated photon. There are clearly events that pass that scattering angle difference cut, but do not pass the CLAS12 event builder's β cut at 0.9. When a photon is mis-identified as a neutron, the momentum must be re-calculated by using the energy-dependent sampling fraction parametrization for photons. This function is described below:

$$SF = 0.250\left(1.029 - \frac{0.015}{E} + \frac{0.00012}{E}\right). \tag{68}$$

In addition to considering the EB-determined PID value of the radiated photon, the number of photons that are associated with a specific e^+ or e^- has to be analyzed. Due to the fact that the overwhelming majority (over 99 percent) of e^+ and e^-'s that lose energy have no greater than 2 photons, only a maximum of 2 photons is accepted and the superposition of the momenta is taken into account.

The effects of the radiative photon corrections on improving the quality of physical quantities can be observed in MC and the RG-A dataset. Using MC data, analysis was done by

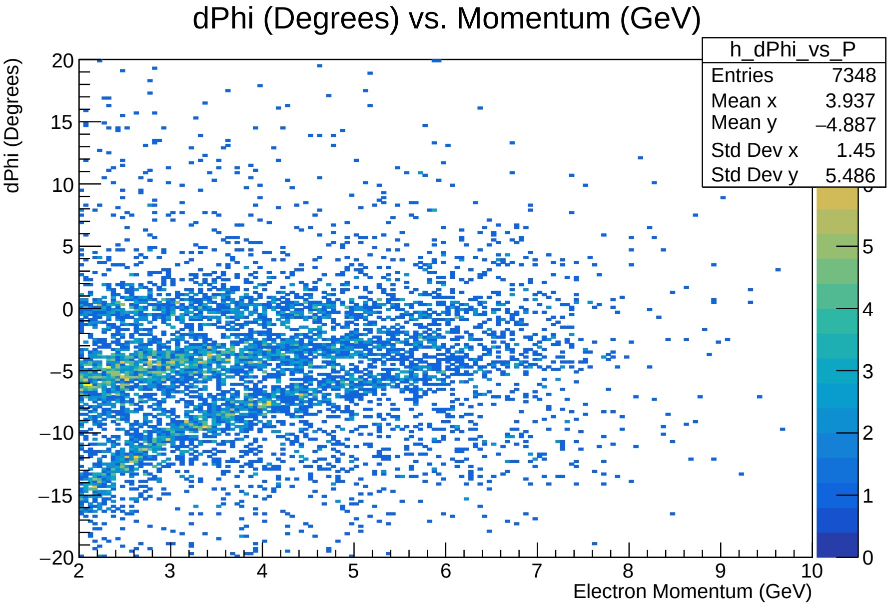

FIG. 66. The difference in phi angle as a function of the original lepton momentum.

comparing the invariant mass and the transverse missing momentum fraction before and after the corrections. As shown in FIG. 68, there was a substantial improvement in the J/ψ peak in MC events, where there was at least one electron or positron associated with a radiated photon. In addition, the shape of the transverse missing momentum fraction was enhanced for the same subset of events, which can be observed in FIG. 69. Overall, the radiative photon correction has benefits for recovering events from resonances that contain radiative tails. With regards to J/ψ cross section measurements, reducing events lost due to radiative energy losses will boost statistics and improve event selection.

In the RG-A dataset, the same effect was studied for quasi-real photoproduction events. Specifically, the ϕ peak was studied before and after those corrections. The signal strength at the ϕ resonance was enhanced, as displayed in FIG. 70. From the analysis of the data, approximately 25 % of e^+e^- events have at least one radiated photon from either particle.

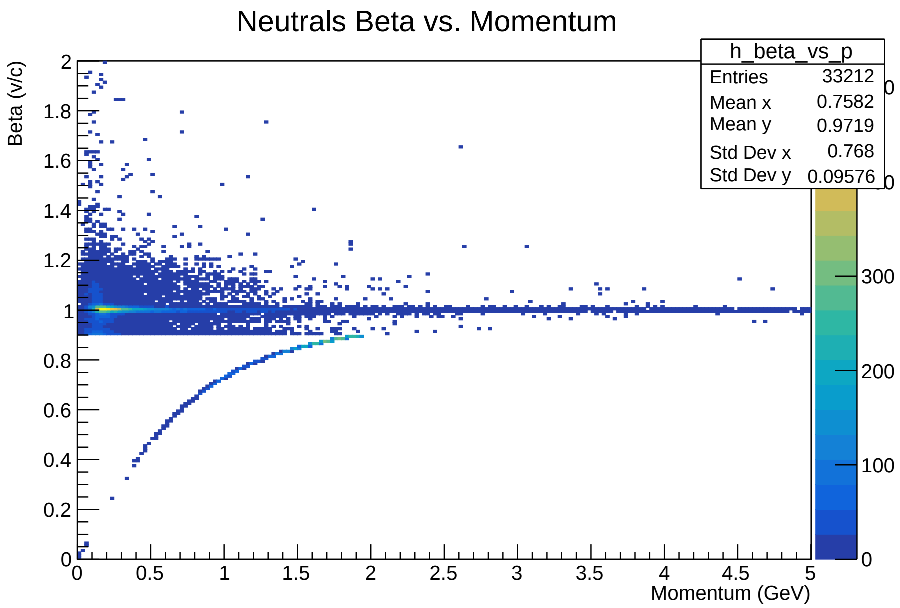

FIG. 67. The β vs. momentum distribution for any neutral particle that passes the scattering angle difference cut.

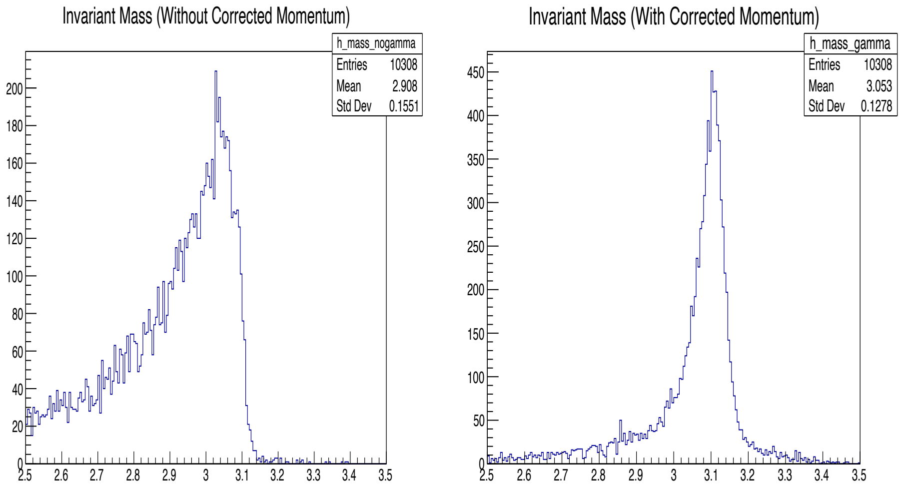

FIG. 68. The improvement of the invariant mass peak after radiated photon corrections in events with at least one electron with radiation.

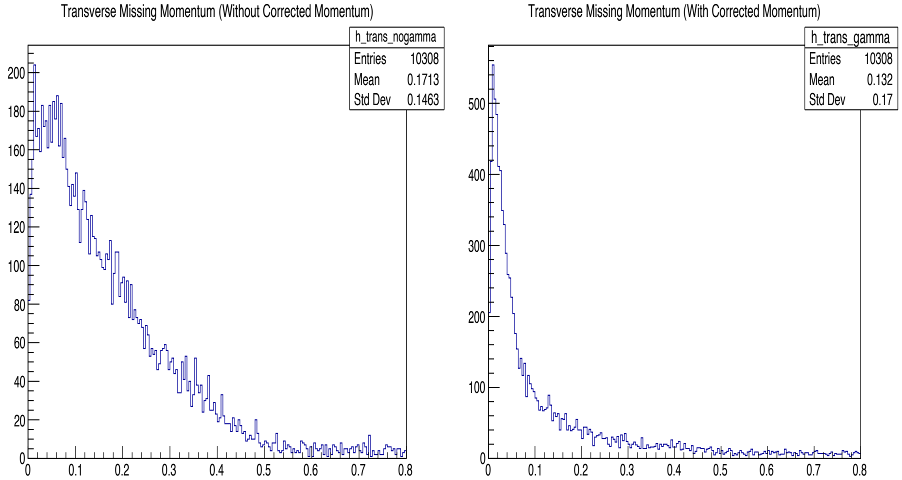
Transverse Missing Momentum (Without Corrected Momentum)

Transverse Missing Momentum (With Corrected Momentum)

FIG. 69. The improvement of the transverse missing momentum after radiated photon corrections in events with at least one electron with radiation..

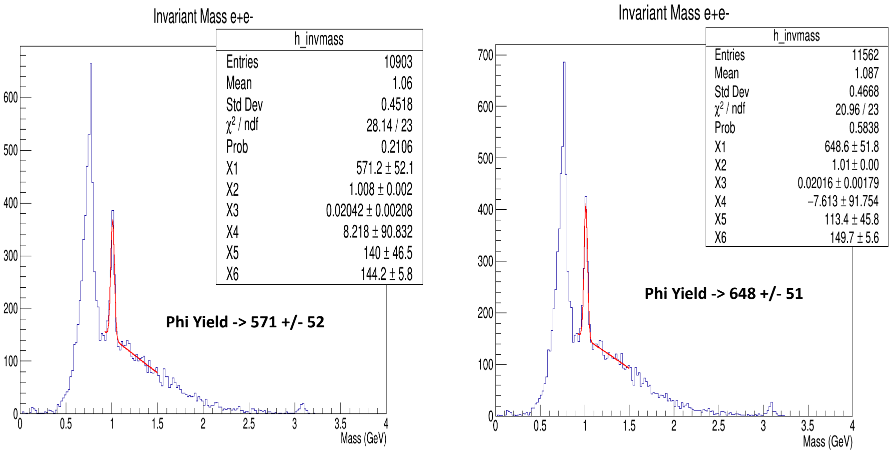
Invariant Mass e+e-

Invariant Mass e+e-

Phi Yield -> 571 +/- 52

Phi Yield -> 648 +/- 51

FIG. 70. The phi resonance yield before and after momentum corrections in the RG-A dataset.

5.9 MISSING NEUTRON MOMENTUM CORRECTIONS

As described in the previous section, some of the electrons and positrons that originate from the decay of J/ψ can have their momentum corrected by taking into account radiative effects. However, while this may improve the signal strength of the J/ψ peak, it will not necessarily adjust the J/ψ peak position to its natural position of 3.097 GeV. This is because electron and positron momentum reconstruction relies on a series of independent variables. These can include the following.

- The precision of the knowledge of the Torus field
- The precision of the knowledge of the DC alignment
- The DC reconstruction algorithms
- DC calibration

From the invariant mass distributions for quasi-real photoproduction, there is clear evidence that the momenta associated with J/ψ di-leptons have varying degrees of drift from the correctly reconstructed values. This was concluded after observing the variation of the J/ψ peak position for different photon energy ranges and more specifically, the momenta of the electron and positron in the final state. Due to the opposite charge of the electron and positron, the trajectories of those two particles are bent in opposite directions in the Torus field. It is logical to anticipate differing effects of the electron and positron momentum on the reconstructed invariant mass peak. For example, at higher electron scattering angles, the momentum reconstruction deviates the furthest from the real momentum of those electrons.

Therefore, the superposition of these potential effects can result in the deviation of the peak positions of not only the J/psi resonance, but also other resonances in exclusive reactions. Therefore, it is necessary to develop scaling factors for the momenta of the electrons and positrons that depend on the kinematics of those particles. One effective strategy is to analyze exclusive reactions that generate enough statistics to do fit analysis and also have the same kinematic coverage of the e^+e^- particles.

One such reaction is the missing neutron analysis where an e^- and π^+ are both detected in the CLAS12 FD with the neutron going un-detected. The first important check that was made was to verify that the final-state electron occupies the same kinematic coverage as the MC J/ψ predicts. For the electrons involved in the J/ψ decay, a lower momentum correlates with higher scattering angles and a higher momentum correlates with lower scattering angles.

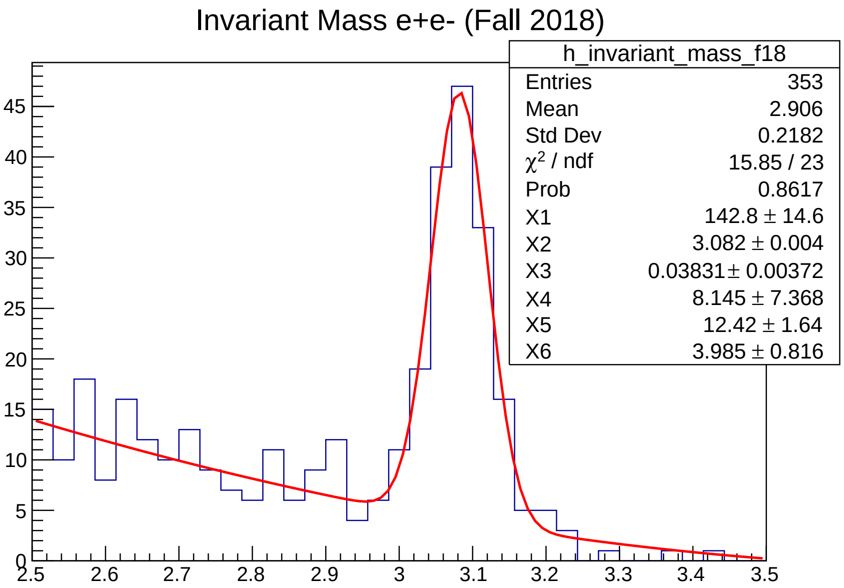

FIG. 71. The position of the J/ψ peak without any momentum corrections besides radiative photon momentum addition.

This is an important observation because the scattering angles are tied to the strength and precision knowledge of the Torus field. The missing neutron final-state is advantageous over other exclusive processes because the kinematic coverage overlaps well with that of the J/ψ final-state electrons and positrons, as shown in FIG. 72.

In order to ensure the clear correlation between the electron momentum and the peak position of the missing neutron, the π^+ in the final-state needs to be constrained. Ideally, the kinematics of the π^+ must be fixed at a narrow scattering angle range so that the dominant factor in the missing neutron peak position is the behavior of the e^- and not the π^+. The analysis of the π^+'s in the final-state was achieved by selecting events under the missing neutron peak and observing the θ vs. p distribution. A common angular range for π^+ throughout the electron binning was 7.5 to 12.5 degrees, which is illustrated by the RG-A Fall 2018 events in FIG. 73.

As shown in FIG. 74, the lower momentum bins for the electron show a higher shift in the neutron peak than the shifts observed for the higher momentum bins where the electron scattering angle is lower. After the calculation of the peak positions, the scaling factors for

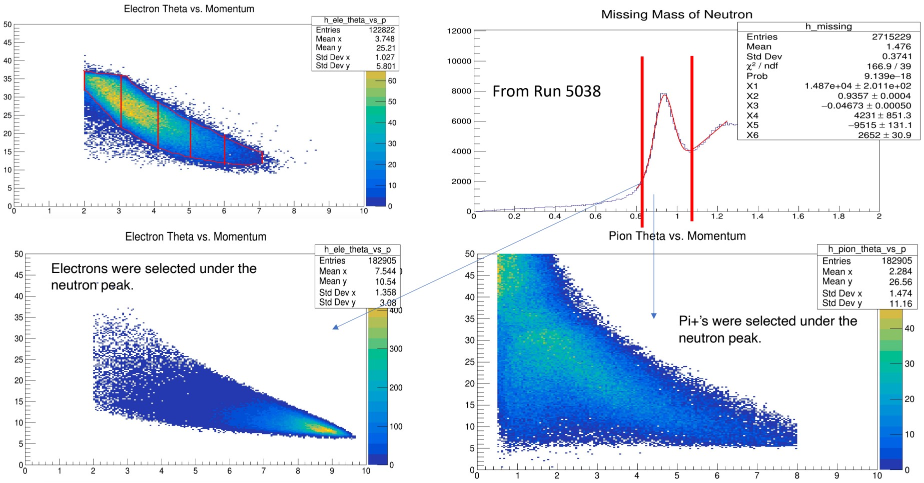

FIG. 72. The display of the J/ψ electron kinematics and the kinematics of electrons and pions under the missing neutron peak.

the electron momenta were calculated by determining the percent change needed to shift the missing neutron peak to the correct position of 0.9396 GeV. The same exact procedure was applied to the study of positron momentum corrections. The only difference was that an out-bending dataset was used instead of the in-bending dataset from Fall 2018. The identified out-bending electron in the same final-state can essentially behave as a positron. The neutron peak position was then analyzed as a function of the ”positron momentum”. Once those means were quantified, a scaling coefficient that would force the neutron peak position into the correct one was calculated. The scaling was performed manually by adjusting the e^+ or e^- by small percent increments until the peak position was positioned at 0.9396 GeV. The parametrization of the percent change as a function of the in-bending and out-bending electron momentum is displayed in FIG. 75. The resulting corrections, ϵ_{e^-} and ϵ_{e^+}, are written as,

$$\epsilon_{e^-} = 2.718 * e^{-0.8404(x-2.0)}. \tag{69}$$

and

$$\epsilon_{e^+} = 0.08(x - 2.0) + 0.11. \tag{70}$$

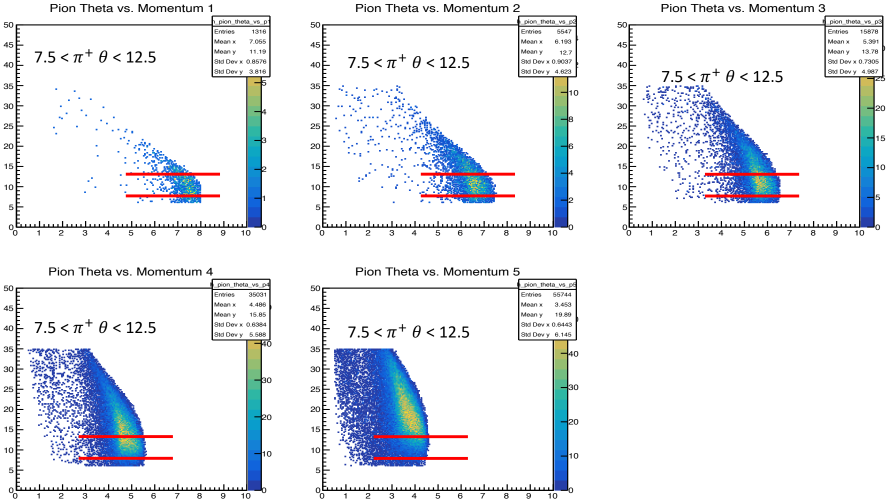
Pion Theta vs. Momentum 1

Pion Theta vs. Momentum 2

Pion Theta vs. Momentum 3

Pion Theta vs. Momentum 4

Pion Theta vs. Momentum 5

FIG. 73. The behavior of pions in events selected under the missing neutron peak.

As a result of the parametrization of the electron momenta scaling factors, the J/ψ peak positions were compared to assess the effectiveness of the momentum corrections. This is illustrated in FIG. 76.

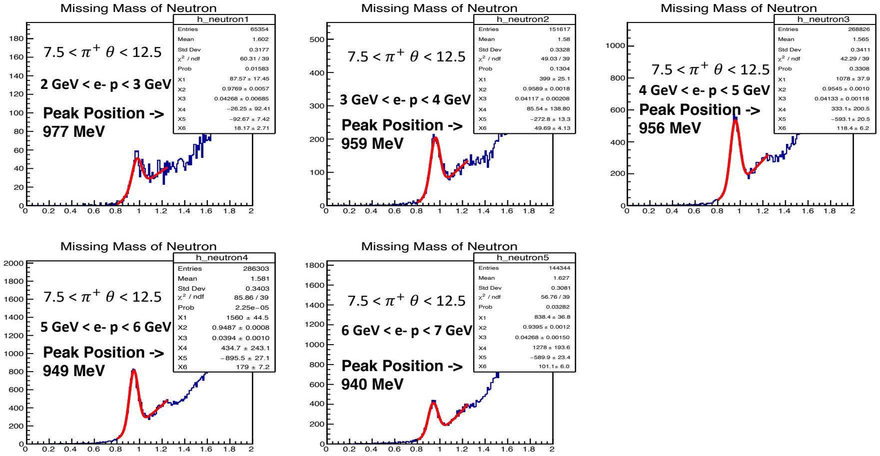

FIG. 74. The effect of the electron momentum/theta on the reconstructed peak position of the missing neutrons.

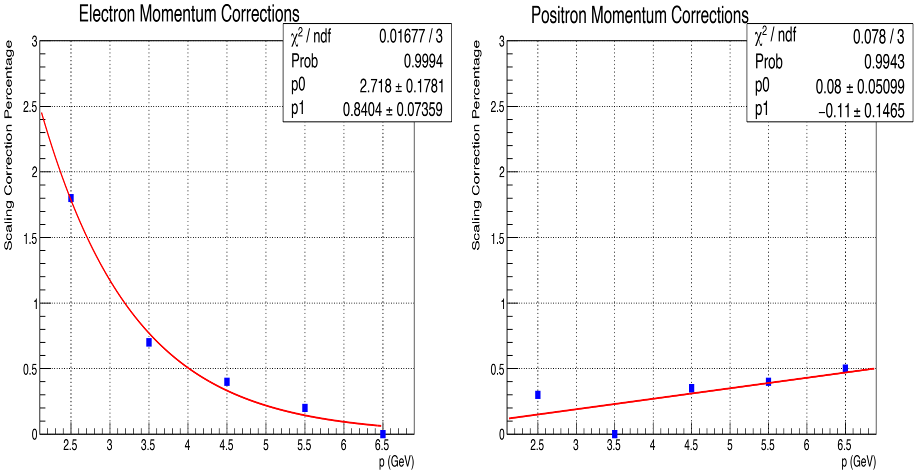

FIG. 75. The parametrization of the percent change of the electron and positron momenta for correcting the missing neutron peak.

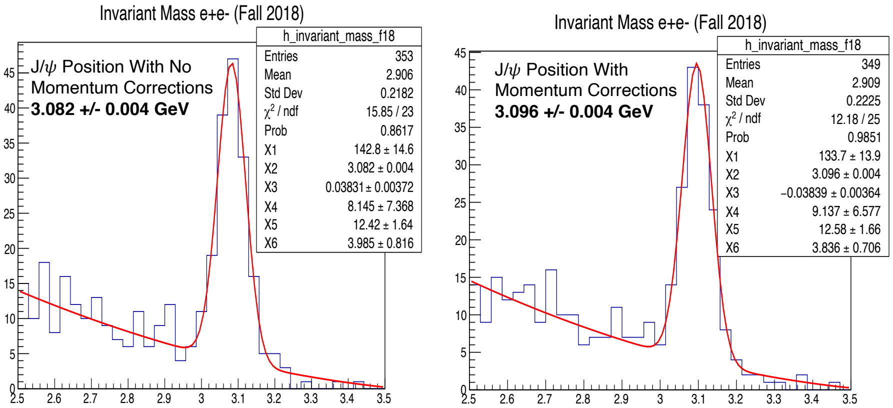

FIG. 76. The progression of the J/ψ resonance position for the un-corrected case, only electrons corrected, and both leptons corrected.

5.10 PCAL FIDUCIAL VOLUME

Reliable electron and positron identification from the decay of J/ψ depends heavily on the reconstruction of energy clusters in all layers of the ECAL. Each of these leptons deposits energy longitudinally, leaving a distinct sampling fraction profile that depends on the momentum of the particle. In order to accurately measure these quantities, different regions of PCAL needed to be analyzed to validate their ability to capture the full extent of the electromagnetic shower. Towards the edges of the PCAL, the reconstruction of the energy clusters will be ineffective due to shower leakage, causing the sampling fraction value to be unreliable. Because the PCAL has a greater surface area than ECIN and ECOUT, it is only necessary to define geometric boundaries for PCAL. Several steps were taken to understand the electron sampling fraction as a function of different independent variables. The analysis was done with Run 5038 of the Fall 2018 RG-A run.

As observed in FIG. 77-78, 9 cm cuts, applied to LV and LW, would be suitable for electron and positron identification since the corrected sampling fraction saturates beyond those values. By applying the 9 cm cuts, it ensures that the showers are properly measured by the ECAL.

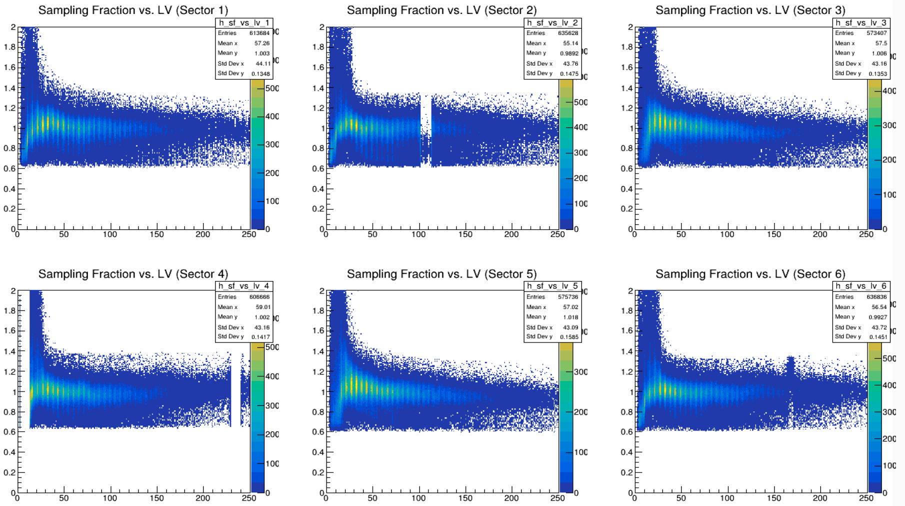

FIG. 77. The energy-corrected sampling fraction was studied as a function of the PCAL V position.

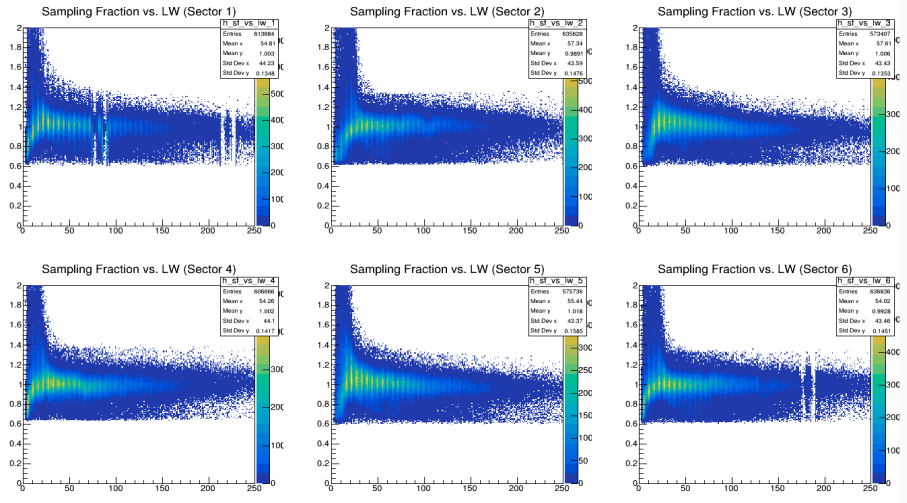

FIG. 78. The energy-corrected sampling fraction was studied as a function of the PCAL W position.

5.11 PROTON ENERGY-LOSS CORRECTIONS

After protons have been detected from FTOF and DC by comparing the measured vertex time and the expected vertex time based on the particle's hypothesized mass, additional corrections were made to the momentum of these protons due to expected energy losses of the protons as they pass through the target, the scattering chambers, SVT enclosure, and the HTCC components. From MC studies, it was observed that the proton momentum difference between the generated and reconstructed values contained a dependence on momentum. For protons with lower energies, the magnitude of the discrepancy was higher due to the energy lost through the CLAS12 forward detector. These differences were highlighted in FIG. 79. The momentum reconstruction difference, dP, was parametrized as a function of momentum by fitting slices of momentum with a Gaussian distribution. The parametrization was done at angles below 27 degrees since protons in the JPsiGen simulations are in that kinematic range. The change in proton total momentum is the following:

$$p_f = p_i + 0.0398946 - 0.0748125 * p_i + 0.0395764 * p_i^2. \tag{71}$$

where p_i is the initial momentum and p_f is the final momentum.

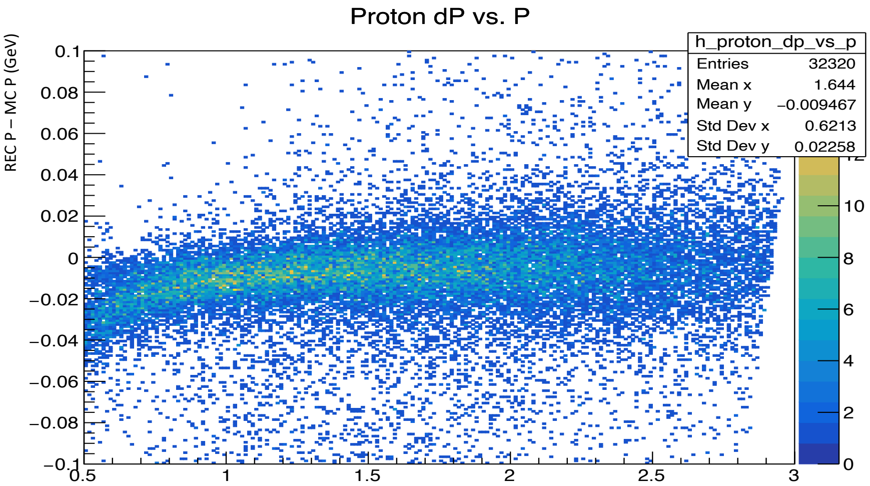

FIG. 79. The difference between the reconstructed and MC momenta of protons.

5.12 EVENT SELECTION FOR J/ψ PHOTOPRODUCTION

After the three final-state particles were identified based on their momenta and detector responses, additional constraints were applied to preserve events with properties of quasi-real photoproduction, which is the case when an un-tagged electron scatters at 0 degrees. Kinematic constraints for quasi-real photons include Q^2 and M_X^2 values that approach zero. These values ensure the virtuality of the photon and that the identity of the scattered electron is valid. The photon's energy is also a cut that is used in this analysis. Since the minimum energy threshold for J/ψ photoproduction is at 8.21 GeV, that is the region where the cut should be applied. However, due to detector resolution effects, the cut was placed at 8.1 GeV.

5.12.1 KINEMATIC VARIABLES OF UN-DETECTED SCATTERED ELECTRON

The analysis of exclusivity variables for this reaction relies on the behavior of quasi-real photoproduction in both simulation (GEANT-4 Monte-Carlo) and results from the selected Fall RG-A dataset. To limit the quasi-real photon's virtuality, the transverse missing momentum components of the un-detected scattered electron were studied in detail in MC and comparisons were made to the RG-A dataset. Also, the missing mass of the reaction was calculated and studied for events in both the MC and RG-A datasets. As displayed in FIG. 80, $\frac{P_x}{P}$ and $\frac{P_y}{P}$ possess symmetric shapes with peaks around zero, as expected for quasi-real photons. The magnitude of the widths rely on the performance of the CLAS12 track reconstruction. The square of the missing mass also possesses a symmetric distribution with its centroid close to zero, which indicates its identity as an electron scattering at very forward angles, an indication of quasi-real photoproduction.

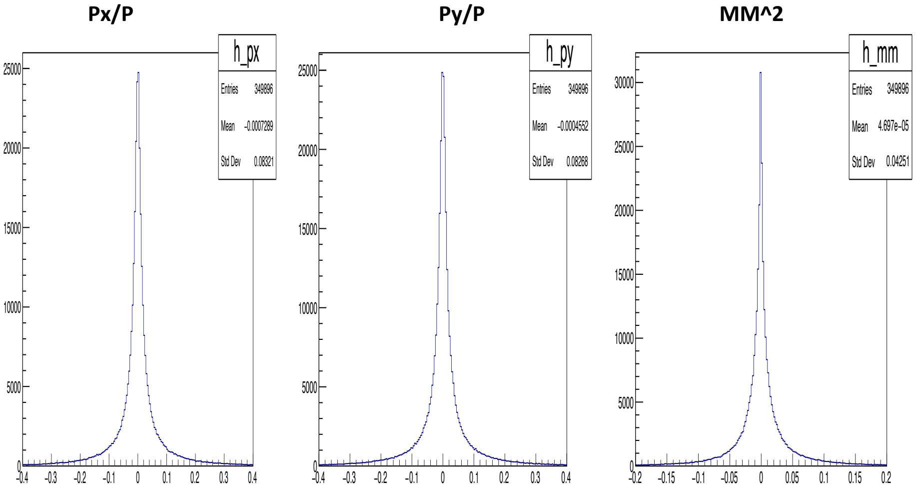
Px/P

Py/P

MM^2

FIG. 80. One-dimensional MC distributions for the missing momentum and missing mass of the un-detected scattered electron for quasi-real photoproduction

In addition to constraining the characteristics of the un-detected scattered electron, cuts were developed in relation to the trajectory of the final state particles. Due to the high invariant mass, the kinematics of the reaction forces the scattered proton to travel into the CLAS12 FD. As predicted by MC studies, the protons for the in-bending Torus polarity mostly fall below a 27 degree scattering angle. The electron and positron, which originate from the decay of J/ψ, end up in opposite sectors of the CLAS12 FD. According to the MC data, the difference in the ϕ angle falls above 150 degrees or below -150 degrees. This is shown in FIG. 81.

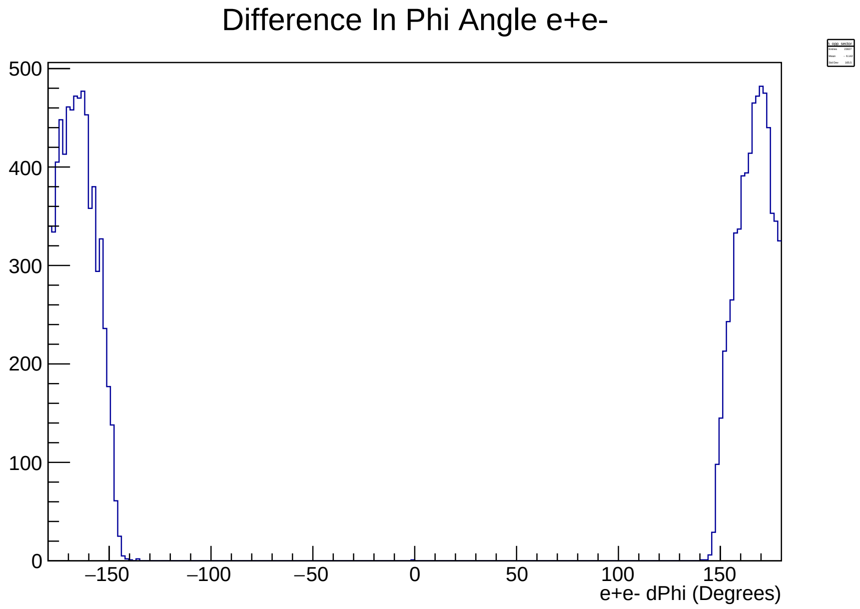

FIG. 81. The phi angle difference in the electron and positron for MC-simulated J/ψ photoproduction.

5.12.2 EFFECT OF PHOTON ENERGY ON EXCLUSIVITY VARIABLES

In addition to understanding the 1D distributions for the exclusivity variables, the dependence on photon energy was quantified. The missing momentum and the missing mass have differing behaviors in different parts of the photon energy range, as shown in FIG. 82. There is a broadening of the missing momentum components due to resolution effects and there exists a tightening of the missing mass as the photon energy increases. Optimizing the event selection in that way allows for more effective rejection of non-photoproduction events whether they originate from pion contamination or other non-photoproduction events. Using the J/ψ photoproduction MC data, which included 50 nA background merging, the resolutions of the variables were plotted as a function of photon energy. These resolutions were the results of the fitting parameters of Gaussian distributions in 100 MeV photon energy bins. To ensure the most realistic resolution, background merging was implemented in the MC data processing. These studies show that the σ values for the missing momentum and missing mass depend strongly on the photon energy and that should be taken into account when applying exclusivity cuts, which can benefit the analysis by enhancing selection and

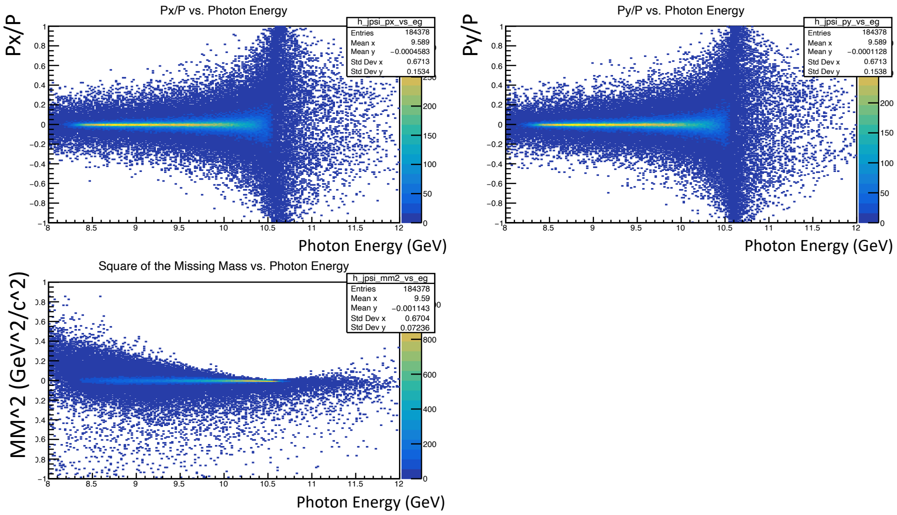

Px/P vs. Photon Energy

Py/P vs. Photon Energy

Square of the Missing Mass vs. Photon Energy

FIG. 82. Two-dimensional MC distributions for the missing momentum vs. photon energy and missing mass vs. photon energy of the un-detected scattered electron for quasi-real photoproduction

reducing background events. As the photon energy increases, the σ values increase for the missing momentum, as shown in FIG. 83 and FIG. 84. The other exclusivity variable, M_X^2, has the opposite trend, as displayed by FIG. 85.

Once the behavior of the exclusivity variables were studied with small photon energy binning, the projected MC resolutions were compared to the resolutions observed in the RG-A dataset. In order to measure the resolutions in the RG-A dataset, the events under the J/ψ resonance were analyzed for the behavior of the $\frac{P_x}{P}$, $\frac{P_y}{P}$, and missing mass values. Table 5. shows the difference in resolution, $\frac{\sigma_{RGA}}{\sigma_{MC}}$, for wide E_γ bins for the transverse missing momentum and the square of the missing mass for events under the J/ψ peak using the Fall 2018 dataset and Spring 2019 dataset.

To select and preserve the maximal number of J/ψ events, the analysis is done using 3σ cuts for all exclusivity variables.

5.12.3 FULL INVARIANT MASS SPECTRUM

Through the detection of the three final-state particles, analysis on the missing momentum and missing mass allows for the selection of quasi-real photoproduction events, as

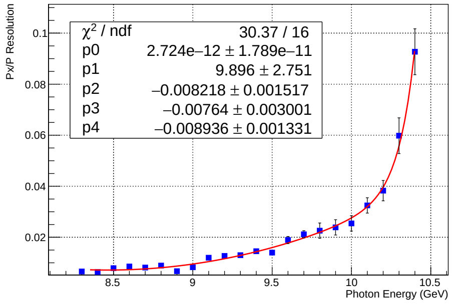

FIG. 83. The resolution of the X-component of the transverse missing momentum fraction was studied as a function of photon energy.

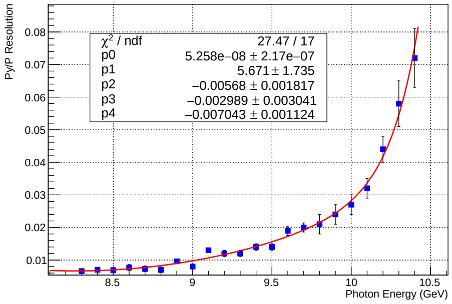

FIG. 84. The resolution of the Y-component of the transverse missing momentum fraction was studied as a function of photon energy.

discussed earlier. The four-vector information of the electron-positron pair is used to calculated the invariant mass. First, the entire mass spectrum was analyzed by tightening the exclusivity cuts, photon energy cuts, applying a different sector cut (as opposed to an opposite sector cut), and relaxing the momentum cuts of the electron-positron pair. The rationale was to analyze the yield and peak position of vector meson resonances, which includes the ϕ and ω mesons. As shown in FIG. 86, the ρ, ω, and ϕ resonances are clearly visible as well as the J/ψ resonance.

5.12.4 INVARIANT MASS ABOVE 2.5 GEV

From the event selection cuts that were designed in the previous subsections, the invariant mass above 2.5 GeV was calculated from the momentum information of the e^+e^- pair from the decay of the J/ψ. Using the sum of a Gaussian and polynomial fit, the number of J/ψ's, the mean, and the width were calculated. The first fit parameter returns the yield. The fitting process is achieved by MINUIT, the standardized minimization routine package offered by the ROOT software. The specific binning shown in the histogram was used for the purpose of achieving the optimal fit quality, a source of systematic uncertainty that is explored in Chapter 7. As observed in the invariant mass distributions, there is a strong J/ψ peak above the background, which consists mostly of pure Bethe-Heitler and electroproduction processes. The invariant mass distributions from Fall 2018 and Spring 2019 dataset are displayed in FIG. 87 and FIG. 88. According to the result of MINUIT regarding the first coefficient, X1,

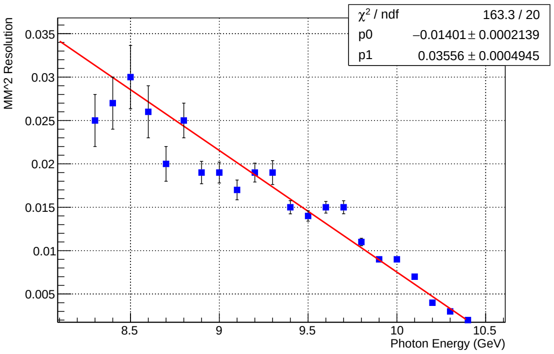

FIG. 85. Using Gaussian plus polynomial fits, the resolution of the square of the missing mass was studied as a function of photon energy.

the total number of J/ψ events in the combined datasets in the Fall 2018 dataset is 134 and the number for the Spring 2019 dataset is 78. Due to the electron and positron momentum corrections from the missing neutron peak studies, the positions of the peaks, represented by the second MINUIT coefficient, are more aligned with the natural position of the J/ψ resonance as compared to the positions before the momentum corrections, as explained in Chapter 5.

5.12.5 KINEMATICS OF SELECTED EVENTS

The scattering angle as a function of momentum was studied for the electron, positron, and proton. In addition, the momenta of the electron-positron pair were shown have a linear correlation in FIG. 89, which was similar to what was observed in the MC studies. For the extraction of cross sections and physical observables, the reconstruction of kinematic variables such as the photon energy and momentum transfer is paramount. The resulting distributions for these quantities helps determine the appropriate binning for the available phase space for J/ψ photoproduction. The 1D distributions of the photon energy, which are shown in FIG. 90 and FIG. 91, shows the increase in the number of events as the photon energy increases as expected. The momentum transfer and the photon energy were studied in FIG. 92 and FIG. 93 for the Fall and Spring datasets, respectively. As observed in these histograms, there is a clear t_{min} boundary that increases when E_γ approaches the threshold energy. The events shown in these 1D and 2D distributions pass an invariant mass cut within

TABLE 5. A table describing the approximated MC vs. data resolution ($\frac{\sigma_{RGA}}{\sigma_{MC}}$) difference for the Fall 2018 and Spring 2019 configurations .

E_γ	$\frac{P_x}{P}$	$\frac{P_y}{P}$	M_X^2
8.3-9.6(F18)	1.9	1.9	1.3
9.6-10.1(F18)	1.6	1.6	1.1
10.1-10.6(F18)	1.5	1.5	0.7
8.3-9.6(S19)	2.5	2.5	0.9
9.6-10.1(S19)	1.8	1.8	1.1

3σ to the J/ψ mean peak position.

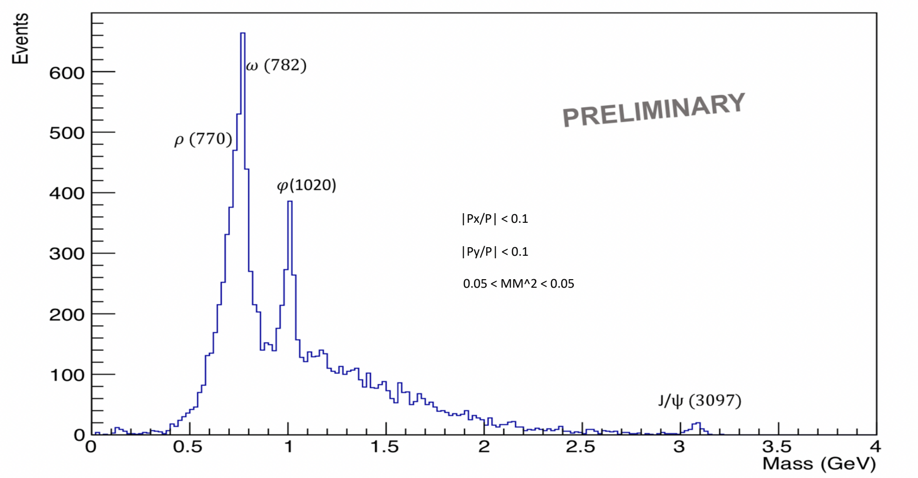

FIG. 86. The full invariant mass spectrum including the lower mass vector mesons

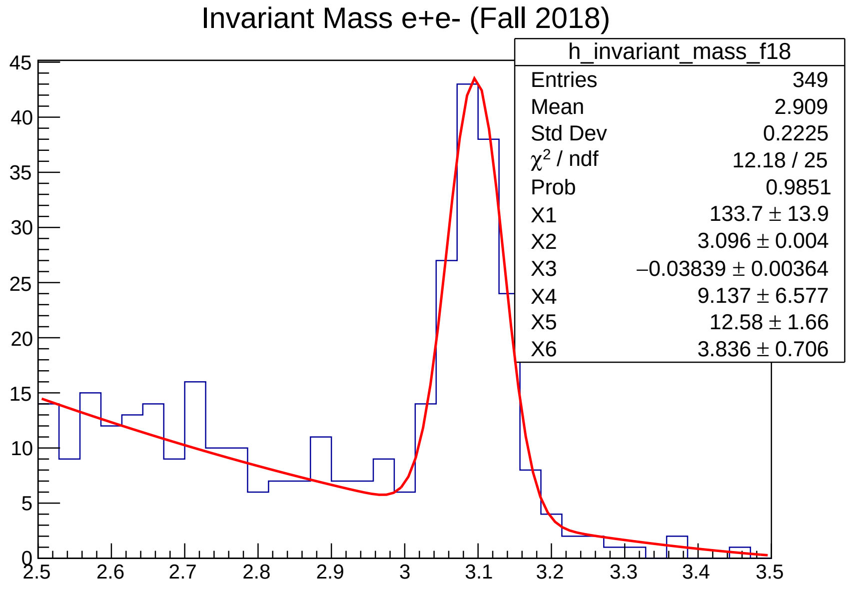

FIG. 87. The full invariant mass spectrum for the combined Fall 2018 dataset.

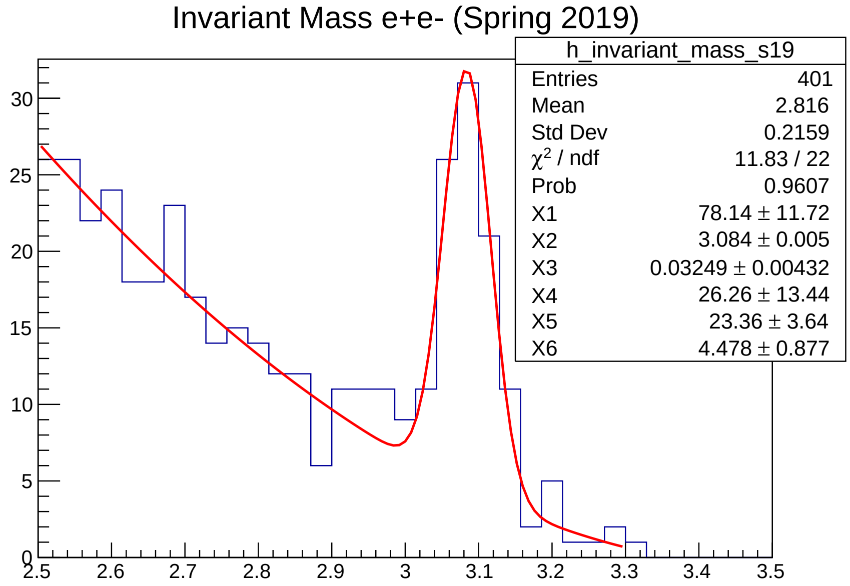

FIG. 88. Separate invariant mass distributions for the Spring 2019 dataset.

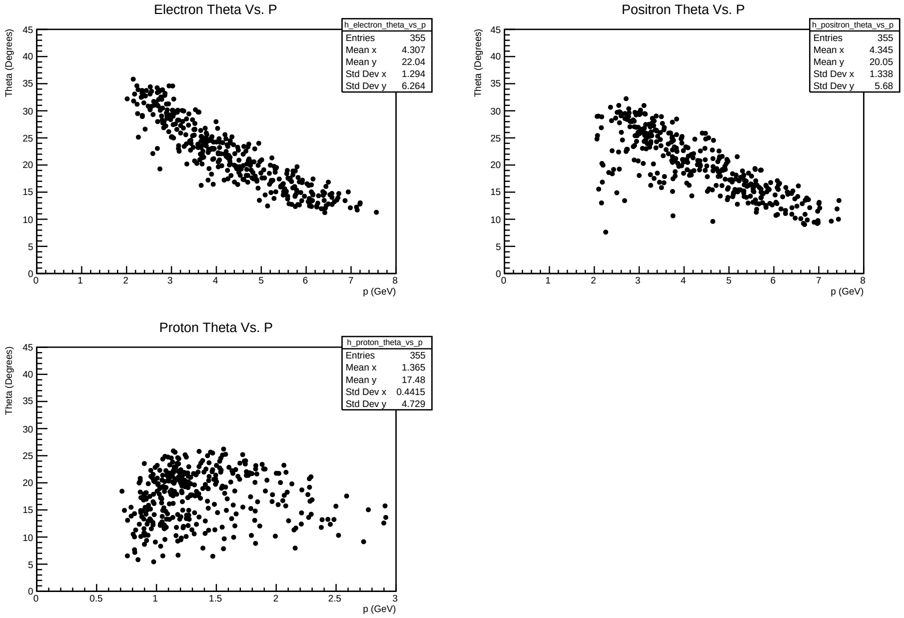

FIG. 89. The kinematics of the final-state particles.

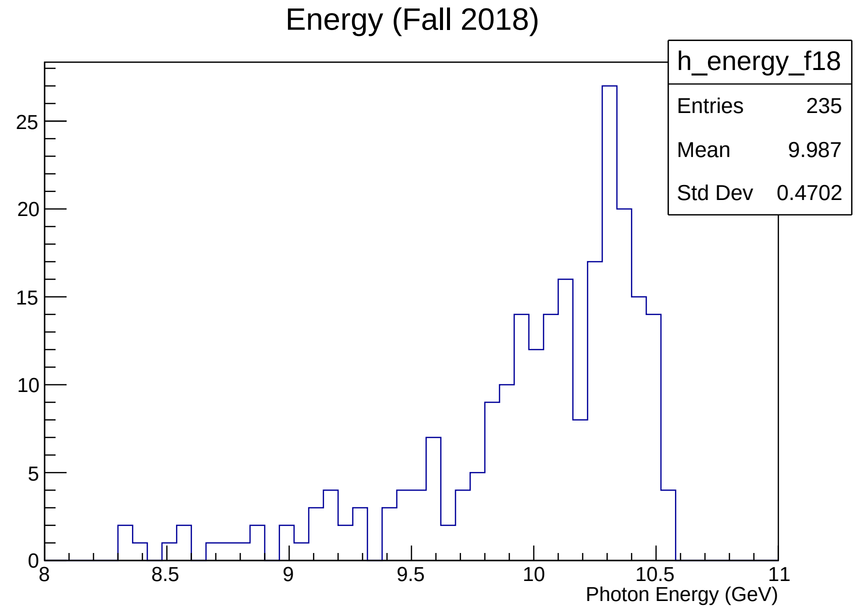

FIG. 90. 1D distribution of the photon energy for the Fall 2018 dataset.

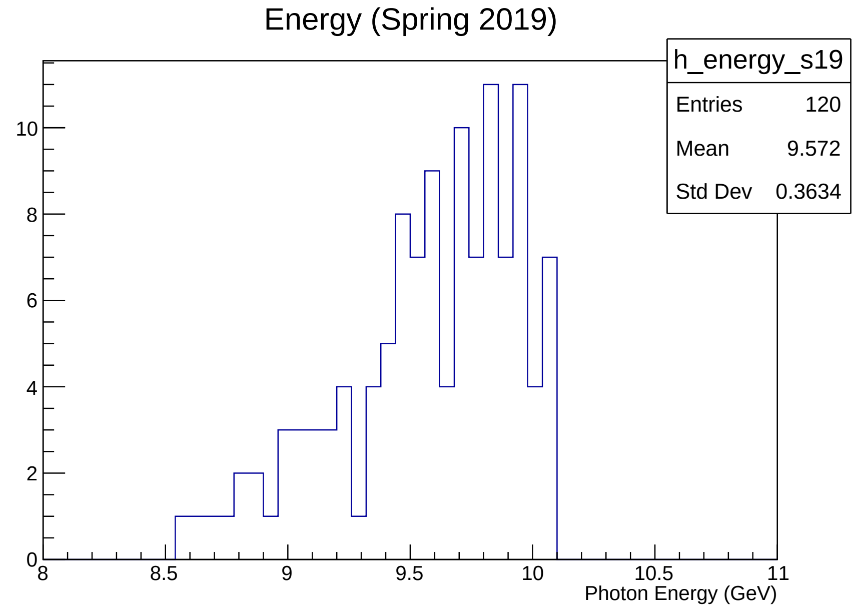

FIG. 91. 1D distribution of the photon energy for the Spring 2019 dataset.

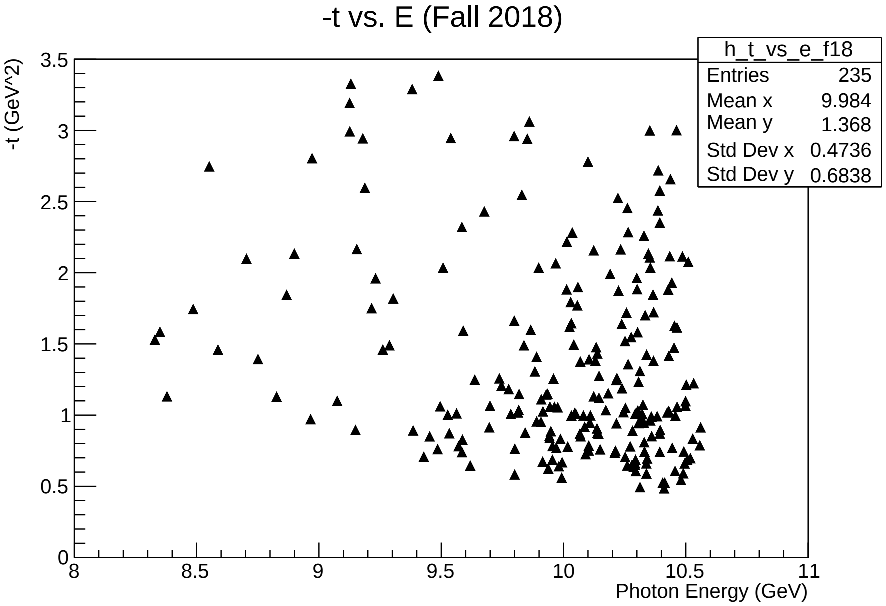

FIG. 92. 2D distribution of the momentum transfer and the photon energies for the Fall 2018 dataset.

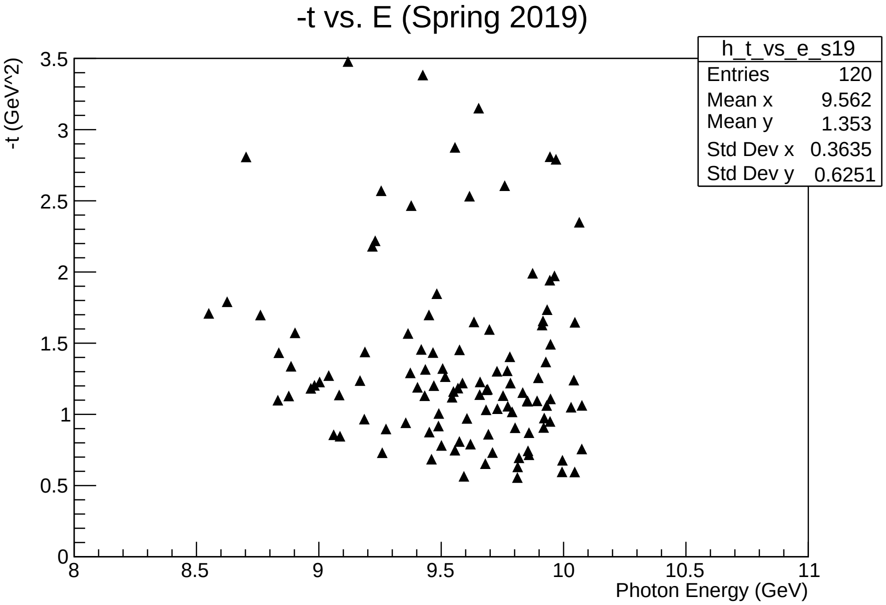

FIG. 93. 2D distribution of the momentum transfer and the photon energies for the Spring 2019 dataset.

CHAPTER 6

J/ψ SIMULATIONS

The generation of J/ψphotoproduction events was done through the generator, JPsiGen. The purpose of this generator is to simulate J/ψ photoproduction through the e^+e^- decay mode. The generator produces events in the LUND format. It contains information about the kinematics of the final-state particles as well as variables that can be used to weight the events by the appropriate scaling factors in the relevant phase space. In terms of the extraction of the J/ψ total and differential cross sections, the event generator (JPsiGen) and the simulation software, GEANT-4 Monte Carlo (GEMC), allows for the calculation of the reconstruction efficiency of the un-tagged photoproduction detection of the e^+e^- pair and the recoil proton. Knowledge of the efficiency is needed to extract the J/ψ yield.

6.1 JPSIGEN DESCRIPTION

JPsiGen was developed by Dr. Rafayel Paremuzyan to study J/ψ photoproduction using the two-gluon exchange, which gives a more conservative estimate of the J/ψ detection rates. The user of the generator has the option to choose the range in phase space that the generated events will occupy. Options include: the beam energy, the minimum and maximum E_γ, the limit of the transferred momentum, as well as the t-slope for the differential cross section. The JPsiGen selects E_γ values within the range from the threshold energy at 8.21 GeV to the beam energy, which is 10.6 GeV for the Fall 2018 configuration and 10.2 GeV for the Spring 2019 configuration. The momentum transfer, $-t$, is selected between t_{min} and t_{max}. If the reaction, $a + b \to 1 + 2$, is known, these kinematic limits can be determined if the E_γ is known. Those limits are t_{min} and t_{max}, which are

$$t_{min} = m_{a,2}+m_{1,2}-\frac{1}{2s}\left[(s+m_{a,2}-m_{b,2})(s+m_{1,2}-m_{2,2}) - \sqrt{\lambda(s, m_{a,2}m_{b,2})\lambda(s, m_{1,2}, m_{2,2})}\right] \tag{72}$$

and

$$t_{max} = m_{a,2}+m_{1,2}-\frac{1}{2s}\left[(s+m_{a,2}-m_{b,2})(s+m_{1,2}-m_{2,2}) + \sqrt{\lambda(s, m_{a,2}, m_{b,2})\lambda(s, m_{1,2}, m_{2,2})}\right] \tag{73}$$

where λ is,

$$\lambda(x, y, z) = (x - y - z)(x - y - z) - 4yz. \tag{74}$$

In addition to the kinematic limits of the generated phase space, JPsiGen also calculates the correct scaling factors on an event-by-event basis. These scaling factors are preserved in the LUND file as well as the final DST files to allow for a more accurate calculation of acceptances. These scaling factors include the t-dependent cross section, the phase space factor, and the photon flux. The cross section, which is based on the two-gluon exchange model, is depicted as,

$$\frac{d\sigma}{dt} = \frac{N_{2g} n_{ue} (1 - x)^2}{R^2 M_{J/\psi}^2 F_{2g} (s - m_p^2)^2}. \tag{75}$$

where F_{2g}, the gluon form factor of the proton is proportional to,

$$F_{2g} = \exp bt. \tag{76}$$

The phase space factor is the difference between t_{min} and t_{max}. The photon flux is described in Chapter 7. FIG. 94 illustrates the phase space coverage for the generated J/ψ events while weighted by the scaling factors mentioned earlier. To show the effect of the slope parameter, b, the 2D weighted phase space was sliced in two of the E_γ bins and the exponential slope was extracted from the fits, confirming the consistency between the input t-slope and the one observed in the MC, as shown in FIG. 95.

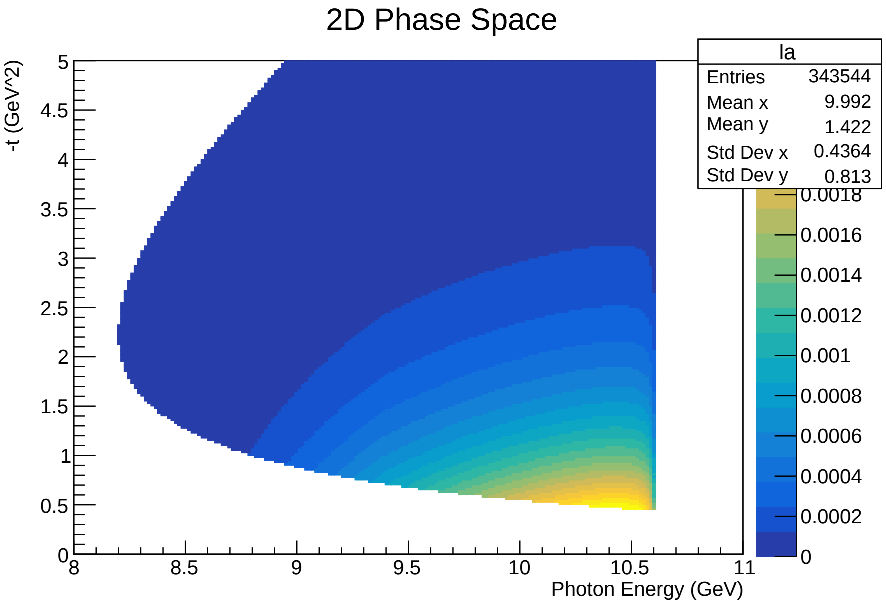

FIG. 94. Phase space for J/ψ photoproduction from MC-generated events for the Fall 2018 configuration.

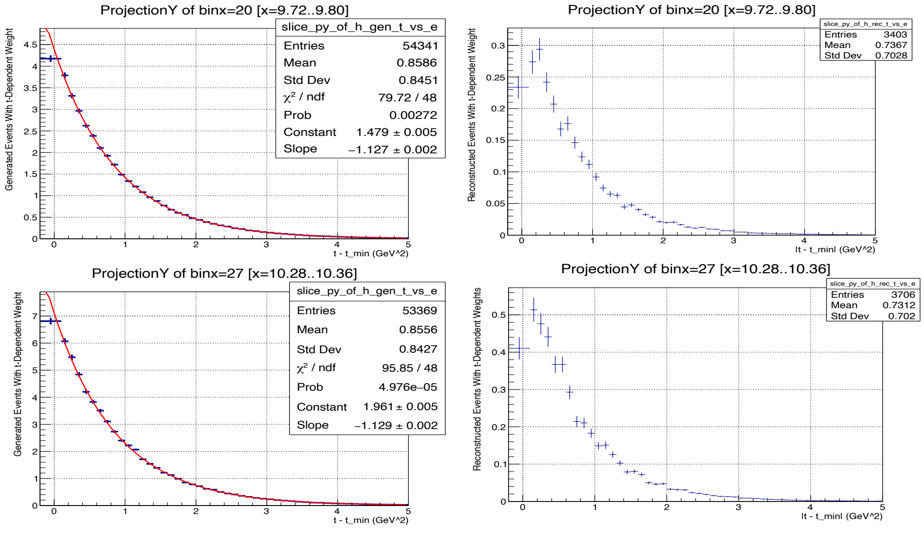

FIG. 95. The weighted generated and reconstructed number of events for two different E_γ bins using MC.

6.2 MC DATA PROCESSING

For the measurement of J/ψ cross sections, it is important to generate high-statistics for MC data to allow for the calculation of acceptances in small bins of E_γ and $t - t_{min}$. In addition, having a large supply of MC J/ψ events allows for the study of systematic effects that require high statistics. To allow for the processing of large J/ψ MC datasets, the Open Science Grid (OSG) was used due to the large computational ability to produce data in a relatively short timeframe. The OSG provides several options including the Run period, the beam energy, the t-slope, and the background merging files associated with the relevant beam current. For the purpose of this analysis, 50 million JPsiGen events were generated by the OSG framework. However, since the RG-A Fall 2018 and RG-A Spring 2019 periods contain mixtures of run configurations, it is necessary to calculate the ratios associated with the different beam currents used. For example, the Fall 2018 RG-A period utilized 45 nA, 50 nA, and 55 nA runs, which contained 75, 8, and 17 percent, respectively. This is displayed in FIG. 96.

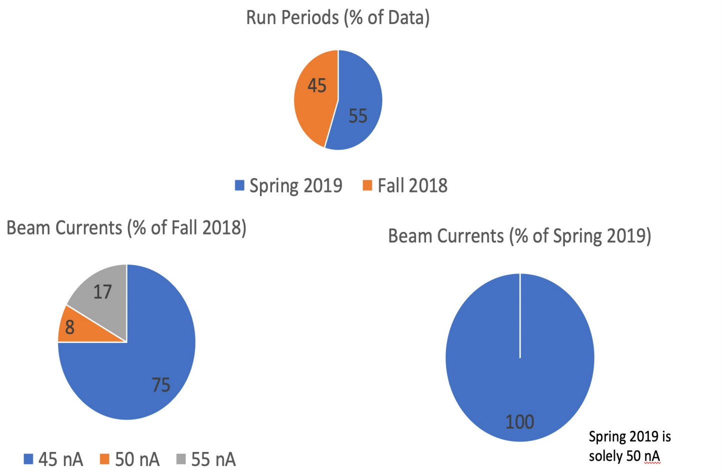

FIG. 96. The proportion of runs based on the run period and beam current settings

Having a large MC dataset with the correct proportion of events from the relevant run periods and run conditions allows for the correct calculation of both the event-by-event and total average efficiencies for the relevant area of phase space for the extraction of cross sections. For the extraction of cross sections described in Chapter 7, datasets from different run periods and beam currents are mixed; therefore, MC data should be approached the same way with a mixture of events from varying run conditions.

6.3 EFFECT OF BACKGROUND MERGING

The study of reconstruction efficiency for J/ψ photoproduction requires simulations that incorporate background merging capabilities. Because the beam current operated as high as 50 nA, background processes induce TDC signals; therefore, tracking reconstruction is unable to accurately produce the curvature of the final-state particles in some cases. This causes an inefficiency stemming from the background. The loss in efficiency was studied for JPsiGen events that were merged with 50 nA background. Two datasets were compared: JPsiGen events with no background merging and those with 50 nA background merging. The efficiency in the merged case is approximately 65 percent of that of the un-merged case when studied as a function of E_γ, as depicted in FIG. 97. The current status of background merging was validated using inclusive electron studies and mainly emphasizes the loss of efficiency in the drift chambers. There are on-going studies on the intrinsic inefficiency of not only the drift chambers, but other CLAS12 detectors.

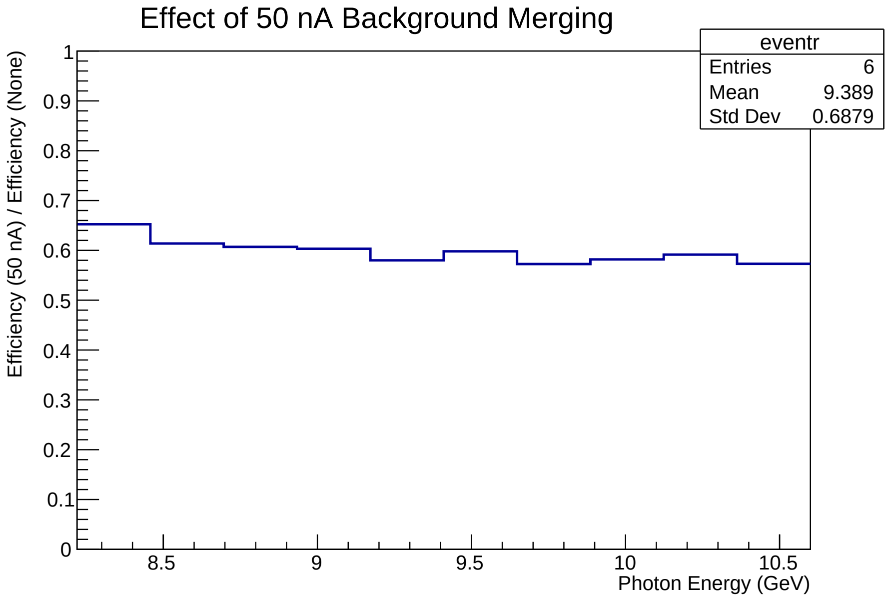

FIG. 97. Ratio of the merged efficiency of J/ψ detection as a function of E_γ over that of the un-merged case.

6.4 EFFICIENCY

Due to intrinsic inefficiencies of detector and the limits of the geometrical acceptance of J/ψ events in the CLAS12 forward detector, only a fraction of J/ψ events get reconstructed and measured in the data. To measure the cross sections, the actual J/ψ yield is needed. Therefore, the reconstruction efficiency should be calculated in the phase space relevant for the extraction of the cross sections. The reconstruction efficiency, η, is defined as the number of reconstructed events over the number of generated events in the specified bin,

$$\eta = \frac{N_{rec}}{N_{gen}}. \tag{77}$$

The efficiency of J/ψ detection was studied as a function of E_γ for two different E_{beam} settings corresponding to the two RG-A periods. This is displayed in FIG. 98.

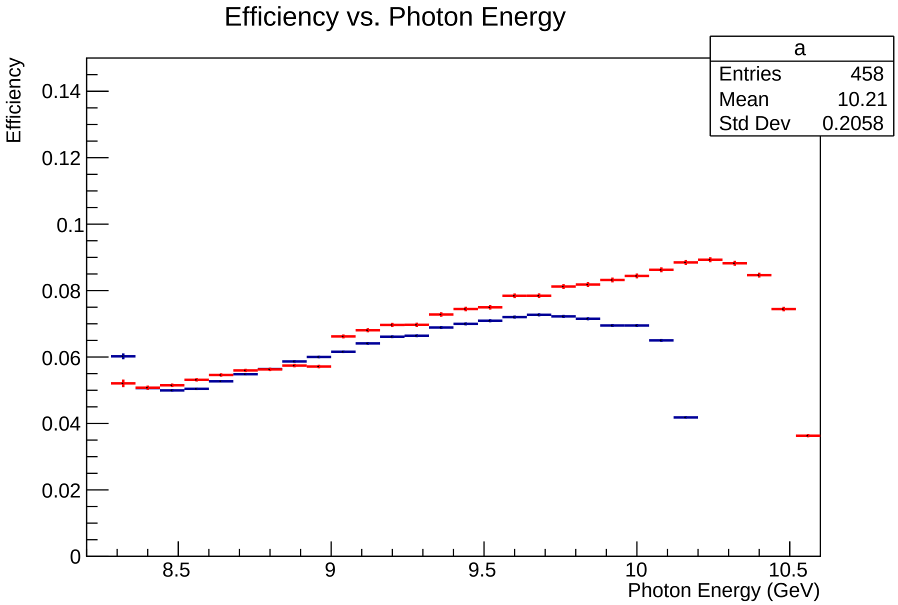

FIG. 98. Reconstruction efficiency for J/ψ detection as a function of E_γ for the Fall 2018 (red) and Spring 2019 (blue) run periods.

In the analysis code, the generated and reconstructed events are filled in separate histograms in (E_γ,$-t'$). To make the geometrical acceptances more realistic, the events are weighted by the scaling coefficients specified earlier in the chapter. The two-dimensional efficiency map was constructed in small bins of E_γ and $-t$, as shown in FIG. 99. Two of the E_γ bins were sliced to show the general trend of the efficiency as a function of t' in FIG.100 and FIG. 101.

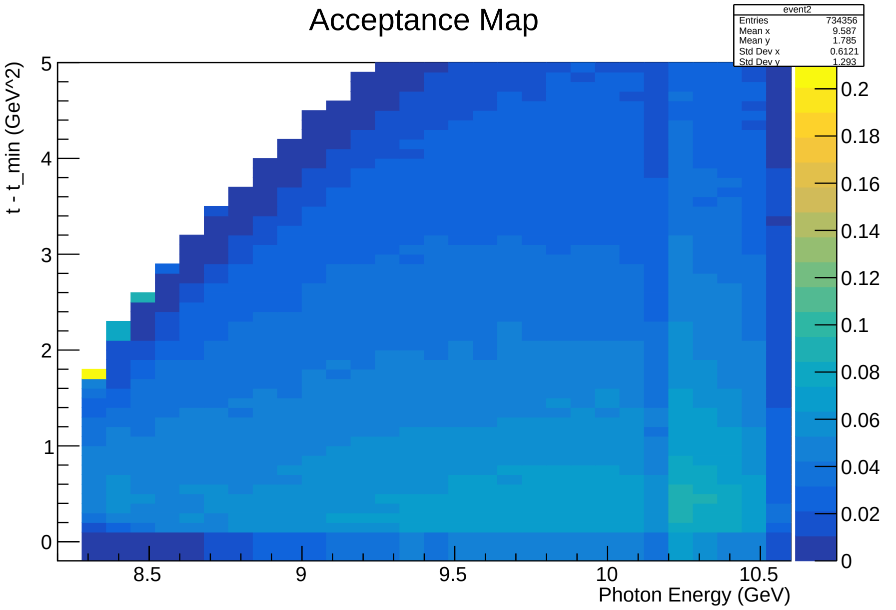

FIG. 99. Reconstruction efficiency for J/ψ events as a function of E_γ and t'.

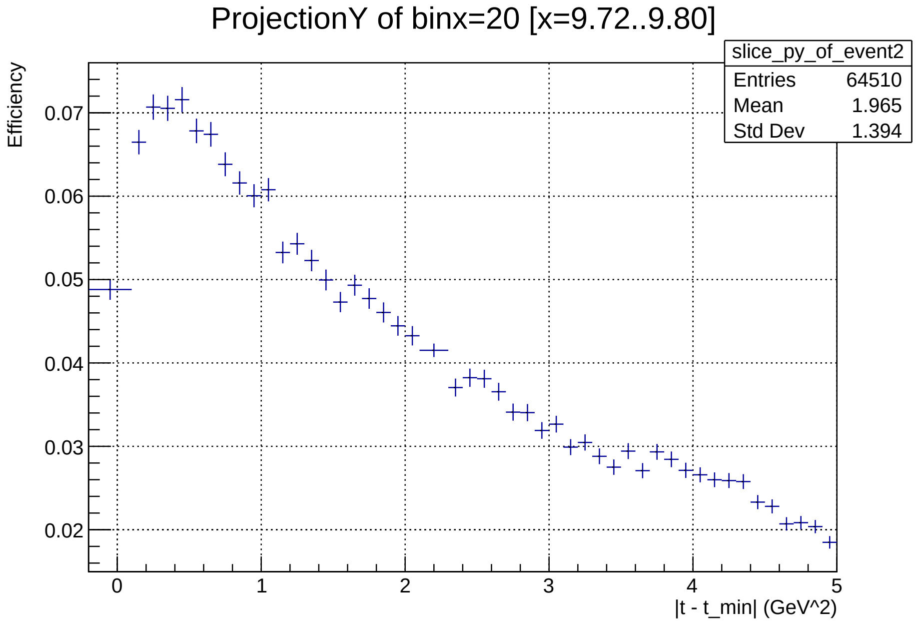

FIG. 100. Reconstruction efficiency for J/ψ events as a function of t' for the energy bin 9.72 GeV to 9.80 GeV.

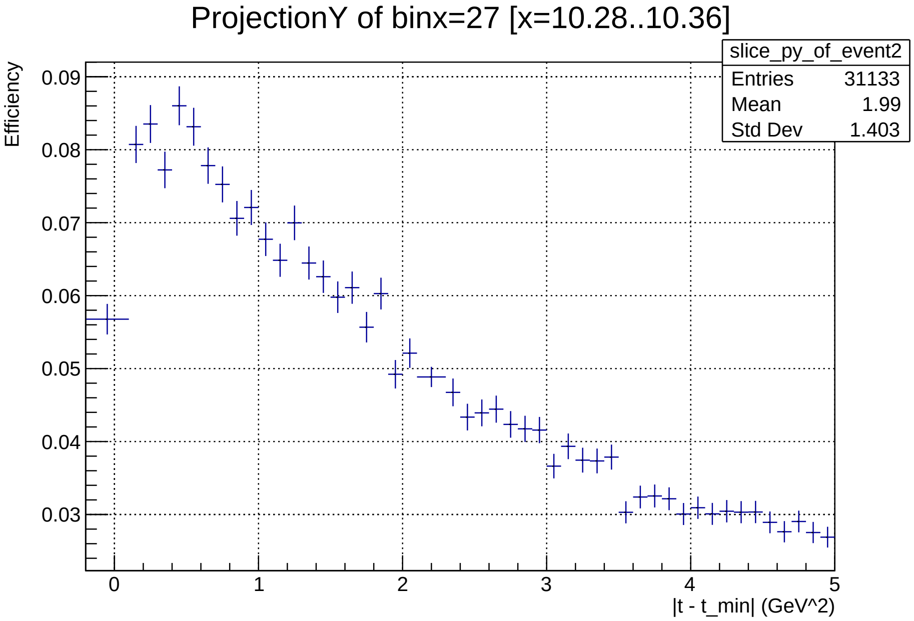

FIG. 101. Reconstruction efficiency for J/ψ events as a function of t' for the energy bin 10.28 GeV to 10.36 GeV.

CHAPTER 7

EXTRACTION OF J/ψ CROSS SECTIONS

7.1 OVERVIEW

After the development of the analysis framework, the total and differential cross sections of J/ψ photoproduction were calculated using the RG-A Fall 2018 and Spring 2019 datasets. The cross section of a particle physics process describes the probability that such a process will occur when an external energy source, such as a beam, interacts with a localized system or target. The differential cross section is similar, but the process's differential is studied as a function of a kinematic variable, such as transferred momentum. For J/ψ photoproduction, the total cross section is measured by detecting the number of J/ψ events in different ranges of E_γ per the integrated luminosity. The formula for the total cross section is,

$$\sigma_0(E_\gamma) = \frac{N_{J/\psi}}{\mathcal{N}_\gamma \cdot n_T \cdot Br \cdot \eta_A}. \tag{78}$$

Measuring the total cross section can be broken down into the following steps.

- Quantify the number of J/ψ events, $N_{J/\psi}$, detected for each photon energy bin.
- Calculate the J/ψ yield, $Y(J/\psi)$, using $N(J/\psi)$ and the average efficiency, η_A, of the E_γ bin.
- Calculate the sum of the virtual and real fluxes, $\mathcal{N}_\gamma$.
- Calculate the number of target protons for the analyzed datasets, n_T
- Scale with the branching ratio, Br, which is 0.06.

The differential cross section is calculated with several overlapping steps with a couple of key differences regarding the calculation of the yield, described in the next subsection. It is studied in terms of $t^{'}$, which is defined as:

$$t' = t - t_{min}. \tag{79}$$

In addition, the size of the t' must be taken into account, as shown below,

$$\Delta t' = t'_b - t'_a. \tag{80}$$

The formalism of the differential cross section is described by the following,

$$\frac{d\sigma}{dt'} = \frac{\mathcal{Y}}{\Delta t' \cdot \mathcal{N}_\gamma \cdot n_T \cdot Br}. \tag{81}$$

7.2 EXTRACTING THE NUMBER OF DETECTED J/ψ EVENTS

For the total cross sections, the invariant mass distributions were made for each photon energy bin. The ranges of these bins, the datasets, and the number of detected J/ψ events are listed on the four histograms, as shown in FIG. 102. The number of J/ψ events, tabulated in Table 6, is calculated by a direct fit of the invariant mass distributions with a Gaussian plus polynomial function.

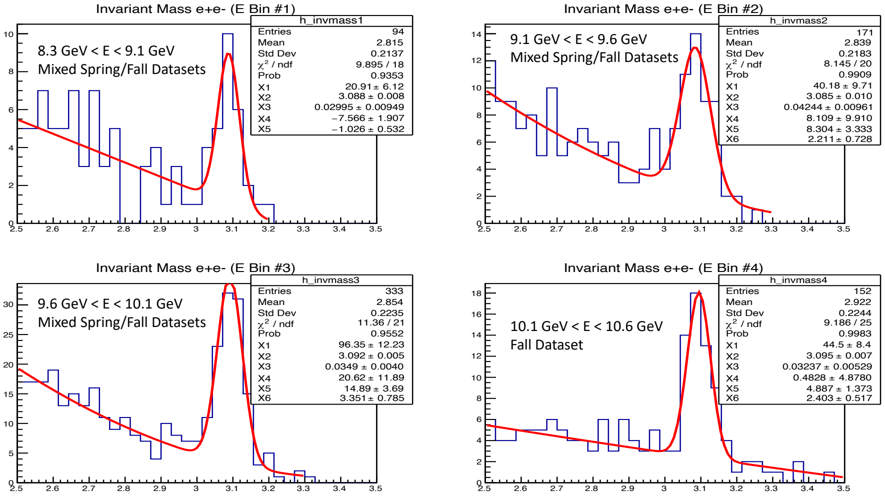

FIG. 102. The invariant mass distributions corresponding to the energy bins used for extracting the total cross section of J/ψ photoproduction.

Calculating the differential cross section requires a robust method of J/ψ yield extraction for bins in photon energy and momentum transfer where statistics is not adequate for direct

TABLE 6. E_γ averages and number of detected J/ψ events for total cross section bins.

E_γ	$(E_\gamma)_{avg}$	N(J/ψ)
(8.3-9.1)	8.81	21
(9.1-9.6)	9.38	42
(9.6-10.1)	9.88	96
(10.1-10.6)	10.33	45

fitting using the superposition of Gaussian and Polynomial functions. Therefore, special procedures need to be developed to calculate the number of J/ψ events that can be verified by systematic comparisons with methods such as direct fitting. In order to extract the J/ψ yield in individual (E_γ,$-t'$) bins, the behavior of the polynomial background that surrounds the J/ψ resonance needs to be understood. The first step is to analyze the entire E_γ bin, which is integrated over all of t'. In each of those bins, it is necessary to apply a direct fitting using the superposition of the Gaussian and Polynomial functions as shown below,

$$\mathcal{F} = \mathcal{P}(M_{e^+e^-}) + \mathcal{G}(M_{e^+e^-}). \tag{82}$$

The polynomial function is written as the following:

$$C_1(x-\mu)^2 - C_2(x-\mu) + C_3. \tag{83}$$

The function, $\mathcal{G}$, contains parameters for the position of the J/ψ peak, the number of J/ψ events, and the resolution of the peak. The function, $\mathcal{P}$, is the background function, which describes Bethe-Heitler events along with background from the mis-identification of pions as positrons. The understanding of $\mathcal{P}$ is useful for J/ψ yield extraction because it allows for the comparison between the number of events (N_h) in the purely Bethe-Heitler region, which is from 2.5 GeV to 2.9 GeV, and number of events (N_b) in the region that comes within $\pm 3\sigma$ of the J/ψ peak position. These values, displayed below, can be obtained by integrating the formula, $\mathcal{P}$,over these regions,

$$N_h = \int_{2.5}^{2.9} \mathcal{P}(M)dM. \tag{84}$$

$$N_b = \int_{m_0-3\sigma_G}^{m_0+3\sigma_G} \mathcal{P}(M)dM. \tag{85}$$

Knowing these two integral values for all photon energy bins can allow for the calculation of the background ratio. The background ratio will be used to estimate the background in the region of the J/ψ peak in low-statistic (E_γ,$-t^{'}$) bins to extract the number of J/ψ's. The background ratio, $\mathcal{C}$, is defined below.

$$\mathcal{C} = \frac{N_b}{N_h} \tag{86}$$

Therefore, with the knowledge of the background ratio related to the background-only section and the signal section of the invariant mass spectrum, the total number of J/ψ events can simply be defined as the difference between the total number of events in the histogram in the range where the signal is present and the estimated number of background events, which is made possible by the background ratio. The formula for the number of J/ψ events in a specific (E_γ,$-t$) bin is displayed below,

$$N_{J/\psi} = N_s - \mathcal{C} \times N_h^t. \tag{87}$$

This method assumes that the $\mathcal{C}$ is independent of the transferred momentum, $-t^{'}$. FIG. 103 and FIG. 104 are illustrations of this method by applying a direct fit on the invariant mass spectrum for two photon energy bins, 9.4 GeV to 10.1 GeV and 10.1 GeV to 10.6 GeV, respectively.

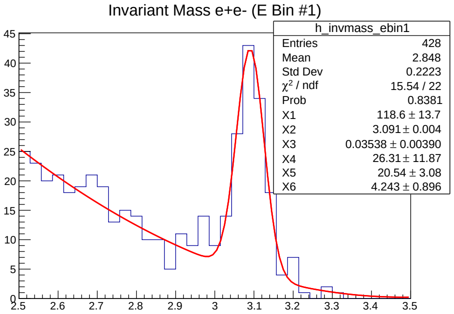

FIG. 103. The first energy range for the differential cross section extraction.

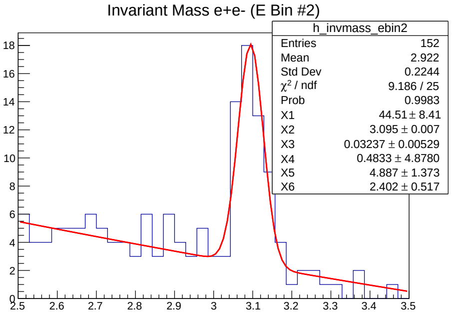

FIG. 104. The second energy range for the differential cross section extraction.

Once the background ratio, $\mathcal{C}$, is established for the large photon energy bins used for the differential cross sections, it is then possible to apply the J/ψ yield extraction formalism each $t^{'}$ bin. For both photon energy ranges, four bins were studied for $t^{'}$. These two photon energy ranges were selected because t_{min} does not vary as much in these regions as opposed to the region very close to the threshold energy at 8.21 GeV. Also, the energy range is broad enough to allow for adequate statistics for the t-slope study. In FIG. 105, the individual invariant mass distributions for the first energy bin are displayed. In FIG. 106, the ones for the second energy bin are displayed.

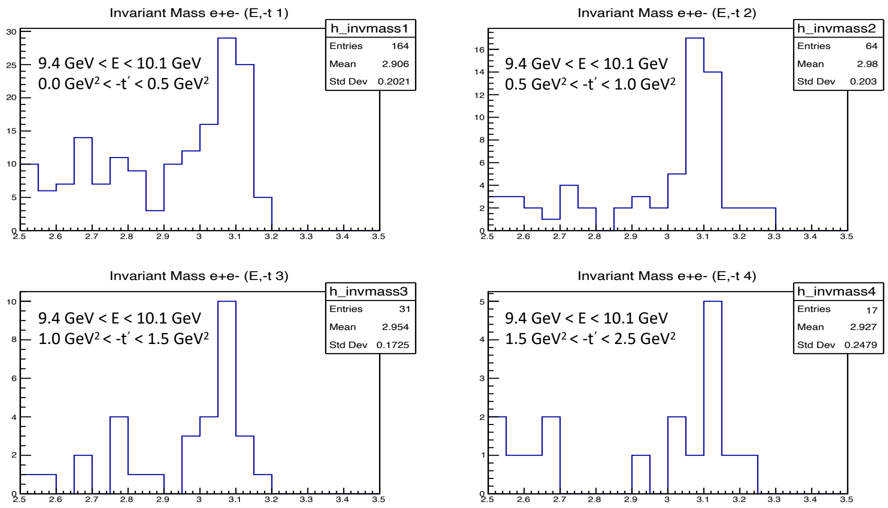

FIG. 105. The invariant mass distributions for the first photon energy range.

Table 7. shows the values for the calculated number of J/ψ events in each of the (E_{γ},$-t^{'}$) bins using the procedures outlined in this section.

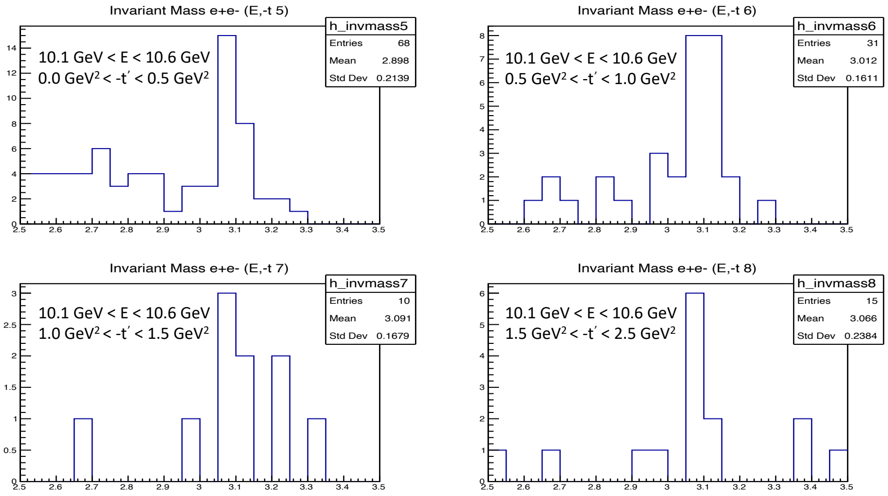

FIG. 106. The invariant mass distributions for the second photon energy range.

TABLE 7. The number of J/ψ events as well as the average t' and the ratio, C, used to make the calculation.

$(E_\gamma, -t')$	$(t')_{avg}$	N(J/ψ)	C
(9.4-10.1)(0.0-0.5)	0.25	67	0.1384
(9.4-10.1)(0.5-1.0)	0.68	36	0.1384
(9.4-10.1)(1.0-1.5)	1.26	18	0.1384
(9.4-10.1)(1.5-2.5)	2.06	8	0.1384
(10.1-10.6)(0.0-0.5)	0.24	19	0.264
(10.1-10.6)(0.5-1.0)	0.69	18	0.264
(10.1-10.6)(1.0-1.5)	1.27	5	0.264
(10.1-10.6)(1.5-2.5)	1.79	7	0.264

7.3 EFFICIENCY TO EXTRACT THE TOTAL J/ψ YIELD

In the Monte-Carlo section, the method behind the calculation of the efficiency was outlined. The JPsiGen event generator combined with background merging simulated photoproduction events with J/ψ. Within the context of calculating the differential cross sections, a 2D map of the efficiency must be developed in small bins in each of the (E_γ,$-t'$) bins. These bins must be understood using fine binning so that the level of accuracy is high and to allow for event-by-event efficiency calculation. Since the J/ψ is not identified in the data on an event-by-event basis, the efficiency is taken into account for all events $\pm 3\sigma$ within the J/ψ mass peak. The idea behind the efficiency calculation for individual (E_γ,$-t$) bins is to quantify the MC-calculated efficiency for each detected J/ψ.

$$\mathcal{Y} = \frac{N_{J/\psi}}{N_s} \times \sum_{1}^{N_s} \frac{1}{\eta_i}. \tag{88}$$

In the region that comes within 3σ of the J/ψ peak, the proportion of signal events versus background events overwhelmingly favors the signal, which is beneficial for this method. The background in the high invariant mass regions mostly comprises of the Bethe-Heitler production of e^+e^- pairs.

One major difference between the differential and total cross section extractions is the approach towards the efficiency value. For the $\frac{d\sigma}{dt}$ calculation, the efficiency was calculated on an event-by-event basis. For the extraction of the total cross section, σ, MC data is used to calculate the average efficiency as shown below,

$$\eta_A^i = \frac{N_r^i}{N_g^i}. \tag{89}$$

where i is the E_γ bin of interest. The numerator and denominator represent the number of reconstructed and generated events, respectively.

7.4 PHOTON FLUX

For the measurement of photoproduction cross sections, such as Bethe-Heitler or J/ψ production, requires the understanding of the rate at which the incoming electrons from CEBAF produce virtual and real photons. For the calculation of the photoproduction rate, that electroproduction cross section has to be scaled by the Estimated Photon Approximation (EPA). The virtual photon flux was calculated using the EPA. Also, the real photon flux was calculated using the standard formula for electron bremsstrahlung. The associated equations are described below. For the purposes of extracting both differential and total cross sections for J/ψ photoproduction, the EPA and the real photon flux need to be integrated within the desired photon energy range. The sum of those two values yields the total photon flux for the calculation of those cross sections:

$$\Gamma(E_\gamma) = \frac{1}{E_b}\frac{\alpha}{\pi * x} * ((1 - x + \frac{x^2}{2}) * log(\frac{Q^2_{max}}{Q^2_{min}}) - (1 - x))dE \tag{90}$$

$$n(E_\gamma) = \frac{dx}{X_0}\frac{1}{E_\gamma} * (\frac{4}{3} - \frac{4}{3}\frac{E_\gamma}{E_b} + \frac{E^2_\gamma}{E^2_b})dE. \tag{91}$$

The virtual and real fluxes are visually displayed in FIG. 107. The fluxes that are shown are associated with beam energies of 10.6 GeV and 10.2 GeV. As shown in the EPA and real flux equations, there is a dependence on the beam energy, so these values must be calculated for separate datasets, which could involve different beam energies. The graph also shows the trends of the two values as the virtual flux drops sharply closer to the beam energy. As for the real photon flux, the relative yield is lower by about an order of magnitude and does not have a strong dependence on the photon energy.

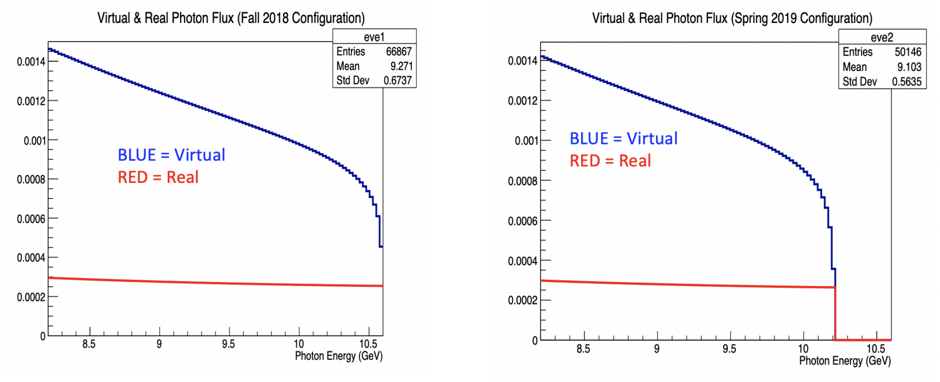

FIG. 107. The virtual photon flux in blue and the real photon flux in red for the Fall 2018 and Spring 2019 run configurations.

7.5 NORMALIZATION STRATEGY

In this dissertation, normalization will not be included in the extraction of the differential and total cross sections. There is strong evidence from simulation studies that the processes that are in the phase space for normalization, from 2 GeV to 3 GeV, do not include only pure Bethe-Heitler photoproduction. There are also Compton diagrams from electroproduction that contribute to the rates observed in the RG-A datasets. For future analysis with normalization and increased statistics, a more comprehensive event selection strategy will be employed to get a reasonable comparison between the BH MC expected rates and the observed rates in the data. The purpose of normalization is to use a well-known process to factor out some unknowns in the cross section extraction. These unknowns can be the detector efficiency or the luminosity. Such a method is necessary because measurements relevant to the cross sections, such as the MC detector efficiency and the knowledge of the luminosity, may not correspond exactly to reality. The normalization factor, ω_c is described below,

$$\omega_c = \frac{n^d_{BH}}{\mathcal{N}_\gamma \cdot n_T} \times \frac{n^G_{BH}}{n^R_{BH}} \times \frac{1}{\sigma_{BH}}. \tag{92}$$

where σ_{BH} is the total theoretical cross section of the Bethe-Heitler produced in the specified mass range and photon energy range. At the current stage of this analysis, we assumed,

$$\omega_c = 1. \tag{93}$$

7.6 DIFFERENTIAL CROSS SECTION RESULTS

The differential cross section, Eq. (81), as a function of $|t - t_{min}|$ was calculated for two different energy ranges from 9.4 GeV to 10.1 GeV and 10.1 GeV to 10.6 GeV. The plots are displayed in FIG. 108 and FIG. 109. The points are fitted with an exponential function:

$$y = p_0 p_1 e^{-p_1 x}. \tag{94}$$

The fit parameters are also shown in these figures. The first parameter, p0, is considered the total cross section for that bin and the second parameter, p1, is the slope of the t-dependence. For the first E_γ bin, the t-slope was determined to be 1.297 ± 0.145. For the second E_γ bin, the t-slope was determined to be 1.208 ± 0.2639.

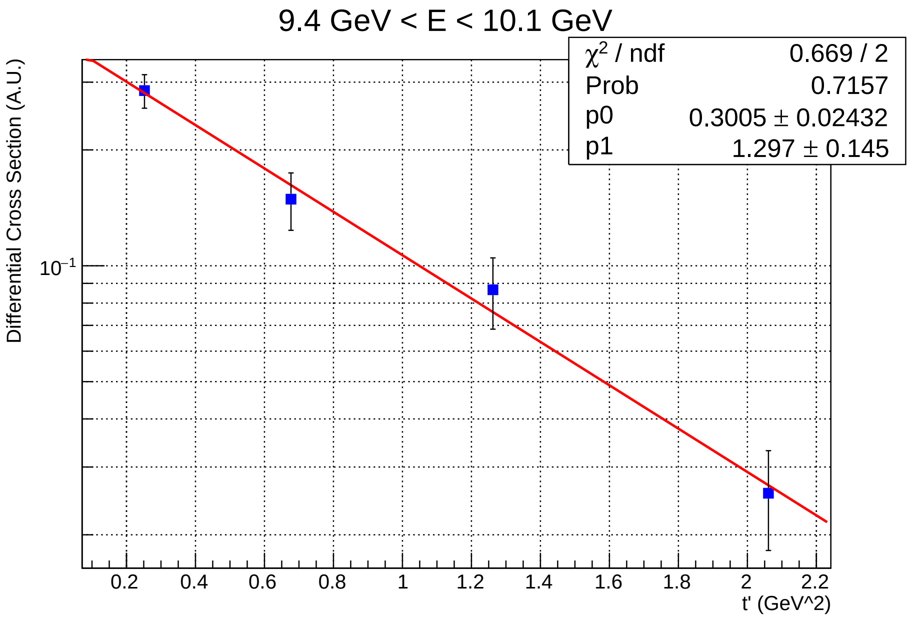

FIG. 108. The differential cross section as a function of t' for the first energy bin.

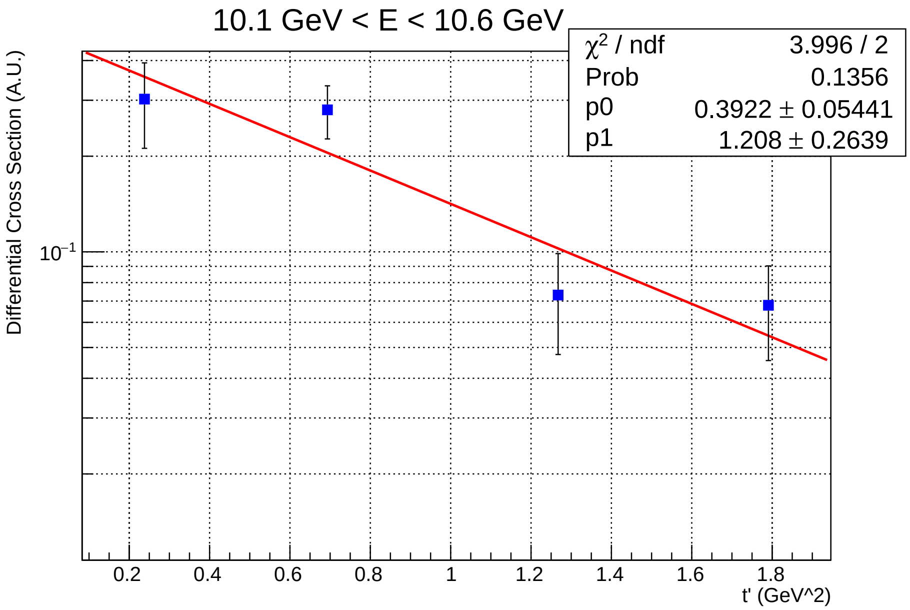

FIG. 109. The differential cross section as a function of t' for the second energy bin.

7.7 TOTAL CROSS SECTION RESULTS

The total cross sections, Eq. (78), were calculated in four bins of E_γ using the methods outlined in the previous subsections. The cross section was also calculated for the two E_γ bins used for the t-slope study by extracting the p_0 parameter from the fit. FIG. 110 shows the results of this study.

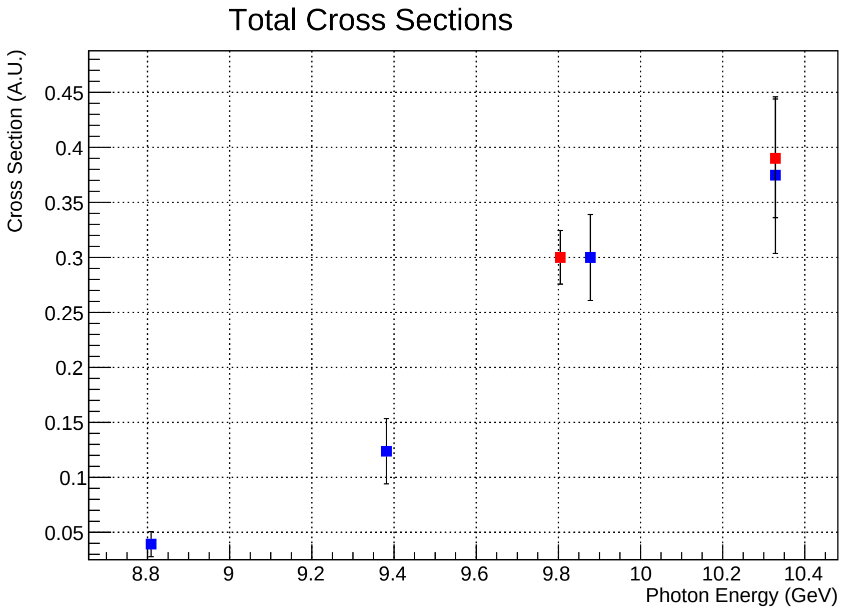

FIG. 110. For the total cross sections, the blue points were extracted from, Eq. (78), and the red points were extracted with the p_0 parameter in the t-slope study.

7.8 SOURCES OF STATISTICAL AND SYSTEMATIC UNCERTAINTY

For the calculation of the total and differential cross sections, there are sources of systematic uncertainty related to the procedures for the cross section extraction methodology as well as the general analysis framework for the selection of particles and events. The objective of these systematic studies is to quantify the amount of contribution certain methods and parameters have on increasing the uncertainty over the final cross section results.

The systematic uncertainties that can affect both the total and differential cross sections are listed below.

- The effect of the event selection cut sizes on Y(J/ψ).
- The effect of the MVA cut value on Y(J/ψ).
- The effect of the JPsiGen t-slope on the calculated efficiencies from MC.

Secondly, the systematics/statistical uncertainties that can affect the differential cross sections are the following.

- The comparison between two methods of extracting Y(J/ψ): $\frac{N_{J/\psi}}{\bar{\eta}_i}$ and $\frac{N_{J/\psi}}{N_s} \times \sum_1^{N_s} \frac{1}{\eta_i}$.
- The re-producibility of the number of J/ψ events, N(J/ψ), in low-statistic bins
- Systematics due to the assumption that C is independent of $t^{'}$

Finally, the systematic uncertainties that only affect the total cross section are listed below.

- The effect of binning on the extraction of N(J/ψ)
- The discrepancy between the number of reconstructed J/ψ events and the extracted fitting result.

7.8.1 EVENT SELECTION EFFECT ON Y(J/ψ)

The parametrized event selection constraints on $\frac{P_x}{P}$, $\frac{P_y}{P}$, and M_X^2 can introduce a systematic uncertainty on the J/ψ yield calculations for both the total and differential cross sections. The standard cuts for event selection are placed at 3σ, where σ is the resolution of the exclusivity variable. To quantify the systematic effect of altering these cuts, the $\frac{P_x}{P}$ and $\frac{P_y}{P}$ were set to 2.5σ and then at 3.5σ while keeping M_X^2 at the default cut value. With this set-up, the yield was re-calculated. The same test was done in the reverse order while varying the M_X^2 cut and keeping the transverse missing momentum components constant. These findings are summarized in Table 8 for total cross section bins and Table 9 for differential cross section bins.

7.8.2 PID MVA CUT EFFECT ON YIELD

As discussed in Chapter 5, most particle identification is based off of the CLAS12 Event Builder algorithms for the e^+e^-p final state reaction. However, for positrons above the HTCC

TABLE 8. A table describing the systematic effect of exclusivity cuts on the Y(J/ψ) yield for total cross sections.

$(E_\gamma, -t')$	Y(Default)	Y($\frac{P_{x,y}}{P}$(L))	Y($\frac{P_{x,y}}{P}$(H))	Y(M_X^2(L))	Y(M_X^2(H))	Total
(8.3-9.1)	400	401	300	445	425	12.7%
(9.1-9.6)	669	672	641	653	657	1.7%
(9.6-10.1)	1503	1495	1538	1420	1510	2.6%
(10.1-10.6)	746	751	712	675	724	3.8%

TABLE 9. A table describing the systematic effect of exclusivity cuts on the Y(J/ψ) yield for differential cross sections.

(E_γ)	Y(Default)	Y($\frac{P_{x,y}}{P}$(L))	Y($\frac{P_{x,y}}{P}$(H))	Y(M_X^2(L))	Y(M_X^2(H))	Total
(9.4-10.1)	2011	1987	2104	1921	2003	2.9%
(10.1-10.6)	722	746	688	652	709	4.5%

pion threshold (4.9 GeV), multi-variate analysis (MVA) was used to distinguish between real positrons and mis-identified pions in the momentum range where contamination is most prevalent. The Boosted Decision Tree (BDT) cut value used in this analysis is placed at -0.01. As a systematic check, a tighter cut was applied to observe how much the total J/ψ yield changes. The shift from the original value is considered the systematic uncertainty due to the MVA cut placement. This check was done for the four E_γ bins for the total cross section measurements and the eight $(E_\gamma, -t)$ bins for the differential cross section measurements. Table 10 and Table 11 show the uncertainties for the total and differential cross sections, respectively.

7.8.3 STATISTICAL N(J/ψ) UNCERTAINTY IN (E_γ, $-T$) BINS

TABLE 10. A table describing the systematic effect of the MVA cut on the Y(J/ψ) yield for total cross sections.

(E_γ)	Y(Default)	Y(MVA=0.05)	Total
(8.3-9.1)	400	401	0.25%
(9.1-9.6)	669	704	5.2%
(9.6-10.1)	1503	1445	4.0%
(10.1-10.6)	746	748	0.27%

TABLE 11. A table describing the systematic effect of the MVA cut on the Y(J/ψ) yield for differential cross sections..

(E_γ)	Y(Default)	Y(MVA=0.05)	Total
(9.4-10.1)	2011	1954	2.9%
(10.1-10.6)	722	725	0.4%

The method that is used for calculating the number of detected J/ψ events in low-statistic bins needs to be checked for the magnitude of the systematic uncertainty. Because of the availability of high-statistics MC, it is straightforward to quantify the deviations in the number of J/ψ events as this methodology is repeated in many iterations. This check is done for each kinematic bin of (E_γ,$-t$). The systematic check is achieved by using the MC data to purposely fill histograms with the same number of J/ψ and BH events within their respective statistical uncertainties. As expected, one would observe subtle deviations of the shape and widths of the signal and background events within that low-statistic bin. Using the same formulas and methods outlined in the previous section, the number of J/ψ events is calculated for many iterations of these histograms. The statistical uncertainty of the J/ψ yield calculation for a specific bin of (E_γ,$-t$) would be the standard deviation of the histogram of the results. One-hundred of these distributions were produced through simulations. For example, for the first (E_γ,t') bin in the energy range between 10.1 GeV

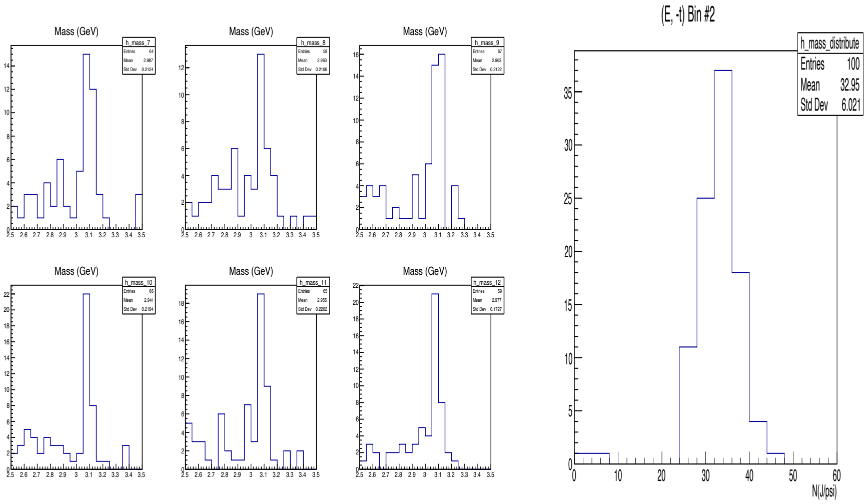

FIG. 111. Six examples of the high-statistics MC check on J/ψ yield calculation method for the E_γ, 9.4 GeV to 10.1 GeV and the t' range between 0.5 and 1.0 and also a distribution N(J/ψ) calculations for 100 histograms that contains the standard deviation for that bin.

and 10.6 GeV, the number of J/ψ and background events in that bin were used to produce MC invariant mass distributions to quantify the systematic uncertainty of the J/ψ yield extraction for bins with less statistics. The result of one these distributions is shown in FIG. 111. Table 12 shows the values for the standard deviations in each of the eight (E_γ,t') bins.

7.8.4 SYSTEMATICS FROM THE ASSUMPTION THAT C IS INDEPENDENT OF MOMENTUM TRANSFER

As described earlier in this section, the determination of N(J/ψ) in (E_γ, $-t$) bins requires the study of the background function in the invariant mass spectrum integrated over all t'. In these bins, there are low-statistics, which means direct fitting is not feasible. The ratio of the integral of the purely background region (2.5 GeV to 2.9 GeV) and the region that comes within 3σ of the J/ψ peak is calculated in the large E_γ bins that are used for the differential cross section extraction. This method operates under the assumption that the ratio, C from Eq. (86), does not change much as a function of t'. However, a systematic check is needed to ensure that the usage of the constant C is valid when extracting N(J/ψ) in various t' bins. In this systematic check, the t' bins are combined between the two E_γ ranges used for the differential cross section extraction, as illustrated in FIG. 112. This ensures enough

TABLE 12. A table showing the standard deviation of the N(J/ψ) MC distributions for each differential cross section bin.

$(E_\gamma, -t')$	STDEV	Error
(9.4-10.1)(0.0-0.5)	6.773	10.1%
(9.4-10.1)(0.5-1.0)	6.021	16.7%
(9.4-10.1)(1.0-1.5)	3.806	21.1%
(9.4-10.1)(1.5-2.5)	2.304	29.2%
(10.1-10.6)(0.0-0.5)	5.699	30.0%
(10.1-10.6)(0.5-1.0)	3.507	19.4%
(10.1-10.6)(1.0-1.5)	1.767	35.3%
(10.1-10.6)(1.5-2.5)	2.324	33.2%

statistics to get a quality fit in order to compare with the sums of the two N(J/ψ) values. The percent deviations are displayed in FIG. 113.

A systematic check was done in determining the effect on variations of the background ratio, C, on the calculated number of J/ψ events, which could contribute to the uncertainty of the differential cross sections. Two C values were considered for each of the eight bins. One was the original C value from the fitting of the background function integrated over all t'. The other C value that is used for this systematic study is the individual C value in each t' bin when the two wide E_γ ranges were mixed, as shown in the previous 113. The tabulated results of this systematic study are summarized in Table 13.

7.8.5 EFFECT OF BIN SIZE N(J/ψ) EXTRACTION FOR E_γ BINS

For the total cross section extraction, the procedure for the N(J/ψ) calculation is to do a Gaussian plus 2nd order polynomial fit where one of the coefficients returns the number of events under the peak and above the fitted background. The parameter that returns N(J/ψ) is dependent on the bin size of the histograms, which range from 2.5 GeV to 3.5 GeV. The bin size is selected based off of the statistics available and the quality of the fit. Such binning will have an effect on the overall shape of the resonance and can introduce a systematic shift of the N(J/ψ) that needs to be understood, so that the effect on the total cross section result is clear. Therefore, a comparison check was done for cases where the histograms have varying

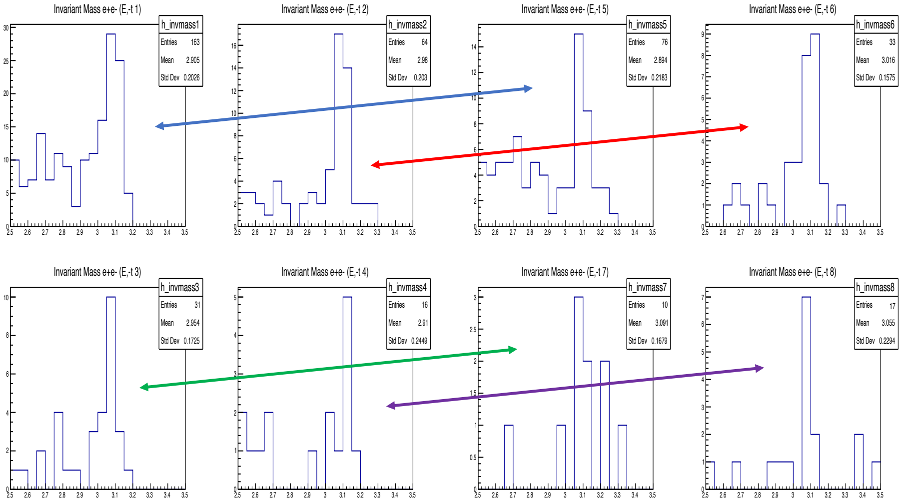

FIG. 112. The mixing of invariant mass distributions in various (E_γ, $-t'$) bins from the combination of two E_γ bins.

bin sizes: 40 MeV, 33 bins, 29 MeV, and 25 MeV. The results of this systematic study are displayed in Table 14.

7.8.6 N(J/ψ) UNCERTAINTY DUE TO THE FIT

For the extraction of the total cross sections, a fitting is done using ROOT's MINUIT utility between the invariant mass spectrum and a functional form consisting of the superposition of Gaussian and polynomial contributions. Using MC data from generated J/ψ and Bethe-Heitler events, histograms were constructed with proportions of signal and background events to closely mirror those observed in the RG-A data for the E_γ bins used for the total cross section measurements. As a systematic check, it is important to study the discrepancy between the number of true reconstructed J/ψ events and the number as determined by the fitting procedure. As shown in the previous subsection, binning has a systematic effect on N(J/ψ), but the pollution of background under the J/ψ may introduce an additional source of uncertainty. As shown in FIG. 114, the percent deviations are on the order of 5 percent.

7.8.7 YIELD METHOD UNCERTAINTY

The measured differential cross section for J/ψ photoproduction is proportional to the

TABLE 13. A table describing the systematic difference between the N(J/ψ) calculation when taking into account variations in the C values.

E_γ	C(E_γ)	C(t')	Total
(9.4-10.1)(0.0-0.5)	67	55	21.8%
(9.4-10.1)(0.5-1.0)	36	30	20.0%
(9.4-10.1)(1.0-1.5)	18	14	28.6%
(9.4-10.1)(1.5-2.5)	8	7	14.2%
(10.1-10.6)(0.0-0.5)	19	17	11.8%
(10.1-10.6)(0.5-1.0)	18	17	5.9%
(10.1-10.6)(1.0-1.5)	5	5	0%
(10.1-10.6)(1.5-2.5)	7	7	0%

TABLE 14. A table describing the systematic difference between the N(J/ψ) result for different binning.

E_γ	N40(J/ψ)	N33(J/ψ)	N29(J/ψ)	N25(J/ψ)	Total
8.3-9.1	23	25	21	20	8.6%
9.1-9.6	43	45	40	46	5.3%
9.6-10.1	99	104	96	98	3.0%
10.1-10.6	49	47	45	47	3.0%

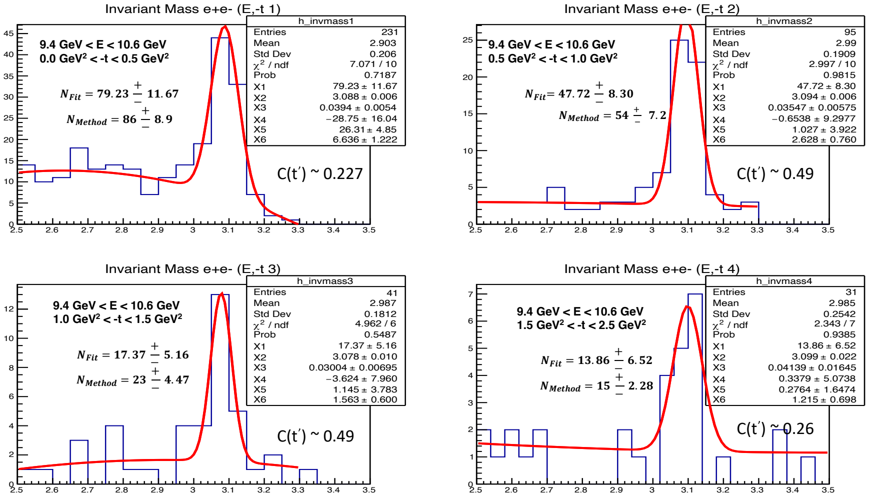

FIG. 113. A comparison of the fitted extraction of the number of events vs. the methodology used for the entire E_γ bins used for differential cross sections.

total yield, which is the number of J/ψ's produced in the experiment after the efficiency is taken into account. In the previous section, the extraction of the number of detected J/ψ events was described. After that is established, methods can be designed to get the most accurate yield by using the efficiency dependence that was computed with fine binning using MC data. Each event whose mass comes within the J/ψ peak has its own individual efficiency based on the measured E_γ and $-t$. There are two methods that are tested for their reproducibility in terms of calculating the yield using the number of J/ψ events and the event-by-event efficiencies. The first involves a straightforward correction to the number of J/ψ events by calculating the average value of the subset of event-by-event efficiencies that passes the invariant mass cut. This is described in the following equation,

$$\mathcal{Y}_1 = \frac{N_{J/\psi}}{\bar{\eta}_i}. \tag{95}$$

An alternative strategy for determining the yield in each differential cross section bin would involve a different approach that involves taking the sum of the reciprocal of each event-by-event efficiency that passes the invariant mass cut. This would involve all events including the background at the base of the J/ψ peak. Therefore a scaling factor is applied to the sum integral that estimates the ratio of signal events over background events. This

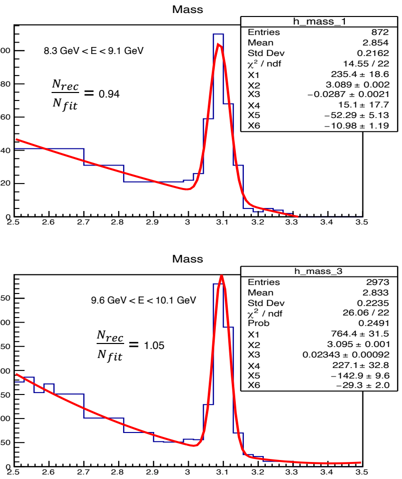

FIG. 114. The comparison between the number of true reconstructed J/ψ events and the fitting result using MC data.

concept is illustrated in the formalism below,

$$\mathcal{Y}_2 = \frac{N_{J/\psi}}{N_s} \times \sum_{1}^{N_s} \frac{1}{\eta_i}. \tag{96}$$

To determine the systematic uncertainty of the yield extraction, it is necessary to compare the results using the two methods for different bins of (E_γ and $-t'$). To demonstrate this systematic check, the J/ψ yields were calculated in the same four bins that are analyzed for the total cross section measurements. Both yield formulas were used and the systematic uncertainty was determined to be low enough to show the validity and effectiveness of both methods. The findings are summarized in Table 15.

7.8.8 GENERATED T-SLOPE EFFECT ON EFFICIENCY CALCULATION

The extraction of cross sections relies on the accurate calculation of the CLAS12 reconstruction efficiency of J/ψ photoproduction events using the generator, JPsiGen. As described earlier, JPsiGen depicts the kinematics of the e^+e^-p final state from the decay of J/ψ. It uses the two-gluon exchange cross section formalism to provide event-by-event weighting to make the acceptances more realistic. However, since the t-slope is not definitively known at a precise level, there is a degree of uncertainty regarding that value. Therefore, the

TABLE 15. A table describing the systematic difference between two different methods of determining Y(J/ψ) for the E_γ ranges used for the differential cross section extraction.

$(E_\gamma, -t')$	Y1(J/ψ)	Y2(J/ψ)	Total
(9.4-10.1)(0.0-0.5)	1001.9	977.3	2.6%
(9.4-10.1)(0.5-1.0)	523.3	521.8	0.3%
(9.4-10.1)(1.0-1.5)	304.3	303.3	0.3%
(9.4-10.1)(1.5-2.5)	180.18	179.2	0.54%
(10.1-10.6)(0.0-0.5)	299.4	279.3	7.2%
(10.1-10.6)(0.5-1.0)	276.9	260.2	6.4%
(10.1-10.6)(1.0-1.5)	72.4	71.8	0.8%
(10.1-10.6)(1.5-2.5)	134.4	132.5	1.4%

efficiency calculation, which depends on those weighted events, will have a systematic uncertainty caused by the knowledge of the t-slope. To quantitatively describe this effect, the efficiency was calculated in four E_γ ranges using different values of the t-slope, b, which is a user-defined parameter in the generator. The following b values were considered: 1.13 (default), 1.6 and 0.5. As shown in Table 16, the deviations in the average efficiency between the varying datasets is less than 10 percent. It is worth noting that these tabulated values were done using datasets done with 45 nA at 5 million events each, so the absolute values are slightly different from the ones used for the cross section measurements, which had mixtures of different background merging conditions. However, the systematic shifts are the same regardless of beam current composition. A similar study was done in Table 17 for the differential cross sections.

7.8.9 TOTAL COMBINED SYSTEMATIC UNCERTAINTIES

After all of the potential sources of systematic uncertainty are analyzed, a total aggregate uncertainty can be assigned to each measurement. There were four total cross section measurements corresponding to four E_γ bins. Additionally, there were eight differential cross section measurements in bins of $(E_\gamma, -t')$. Therefore, a total of twelve combined systematic uncertainties are calculated from the quadratic sum of each individual systematic uncertainty. The combined systematic uncertainties are in Table 18. and Table 19.

TABLE 16. A table describing the systematic difference between the η_A terms for the total cross sections being calculated with different JPsiGen t-slope parameters.

E_γ	$\eta_A(b = 1.13)$	$\eta_A(b = 1.6)$	$\eta_A(b = 0.5)$	Total
8.3-9.1	0.0514155	0.0533932	0.0459869	7.6%
9.1-9.6	0.0613602	0.0636787	0.0529164	9.5%
9.6-10.1	0.0684269	0.0724445	0.0601382	9.4%
10.1-10.6	0.0649495	0.0679064	0.0566321	9.3%

TABLE 17. The systematic difference between the $\sum \frac{1}{\eta_i}$ terms for the differential cross sections being calculated with different JPsiGen t-slope parameters.

E_γ	$\sum \frac{1}{\eta_i}(b = 1.13)$	$\sum \frac{1}{\eta_i}(b = 1.6)$	$\sum \frac{1}{\eta_i}(b = 0.5)$	Total
(9.4-10.1)(0.0-0.5)	1694	1683	1651	1.3%
(9.4-10.1)(0.5-1.0)	968	951	951	1.0%
(9.4-10.1)(1.0-1.5)	511	509	502	0.9%
(9.4-10.1)(1.5-2.5)	390	387	398	1.5%
(10.1-10.6)(0.0-0.5)	536	532	518	1.8%
(10.1-10.6)(0.5-1.0)	326	334	336	1.6%
(10.1-10.6)(1.0-1.5)	140	136	135	1.9%
(10.1-10.6)(1.5-2.5)	249	258	253	1.8%

TABLE 18. Systematic uncertainty summary for the total cross sections.

(E_γ)	MVA	Binning	Fit	t-Slope	Exc. Cuts	Total
8.3-9.1	0.25%	8.6%	6.0%	7.6%	12.7%	18.1%
9.1-9.6	5.2%	5.3%	5.0%	9.5%	1.7%	13.2%
9.6-10.1	4.0%	3.0%	5.0%	9.4%	2.6%	12.0%
10.1-10.6	0.27%	3.0%	4.0%	9.3%	3.8%	11.2%

TABLE 19. Systematic uncertainty summary for the differential cross sections.

$(E_\gamma, -t')$	MVA	Yield	t-Slope	Exc. Cuts	C	Total
(9.4-10.1)(0.0-0.5)	2.9%	2.6%	1.3%	2.9%	21.8%	22.3%
(9.4-10.1)(0.5-1.0)	2.9%	0.3%	1.0%	2.9 %	20.0%	20.4%
(9.4-10.1)(1.0-1.5)	2.9%	0.3%	0.9%	2.9%	28.6%	28.9%
(9.4-10.1)(1.5-2.5)	2.9%	0.54%	1.5%	2.9%	14.2%	14.9%
(10.1-10.6)(0.0-0.5)	0.4%	7.2%	1.8%	4.5%	11.8%	14.7%
(10.1-10.6)(0.5-1.0)	0.4%	6.4%	1.6%	4.5%	5.9%	9.94%
(10.1-10.6)(1.0-1.5)	0.4%	0.8%	1.9%	4.5%	0.0%	4.97%
(10.1-10.6)(1.5-2.5)	0.4%	1.4%	1.8%	4.5%	0.0%	5.06%

CHAPTER 8

CONCLUSION

8.1 J/ψ PHOTOPRODUCTION NEAR THRESHOLD

The measurement of the total and differential cross sections for J/ψ photoproduction using CLAS12 has the potential to illustrate a more clear model of the reaction mechanism in the threshold region. These measurements are sensitive to form factors that describe the distribution of color charge in the proton. Using the available RG-A data from the CLAS12 experiment, preliminary cross section results have been achieved and this analysis will continue to evolve as more data (RG-A Spring 2018) become available after calibration and processing. This boost in statistics will be needed for the pentaquark search study. The current status of J/ψ analysis in CLAS12 has a strong foundation. Advancements have been made regarding particle identification, event selection, momentum corrections, efficiency studies, and background studies. As preliminary results await from Hall C, it needs to be determined what models best suit the cross section dependence on photon energy for CLAS12. There have been proposed models that assume a superposition of the two-gluon and three-gluon exchange mechanisms. One piece of the CLAS12 J/ψ analysis that needs to be improved and added is the normalization using the Bethe-Heitler cross section, which is a well-known reaction. The preliminary results established in this dissertation assume an ideal knowledge of the luminosity and the detector efficiency. Normalization has not been done yet and will be incorporated in future analysis. Additional studies are needed to study the comparison of the expected rates from MC (electro-production and photo-production) and what is measured in the RG-A data. Once these are analyzed, a more complete conclusion regarding the impact on physics can be drafted.

8.2 TORUS FIELD MAPPING PROJECT

The preparation, implementation, and analysis associated with the Torus field mapping project proved to be valuable to the CLAS12 experiment. As mentioned in the particle identification section, there are several factors that can cause imperfections regarding the reconstruction of charged particles in the forward detector. One of them is the extent to which the field map model used in reconstruction mirrors the field in reality. By measuring the field using precise instrumentation and a well-engineered procedure, there is a baseline set of measurements that can be used as comparisons to the field model iterations that are used for DC reconstruction. In addition, a unique mathematical method was developed to minimize a chi-squared function which contains fitting coefficients associated with the distortions of one of or many coils. The final results were relayed to the magnet team and several iterations of field maps were designed based on those calculated coil distortions, which include translational motions and ad hoc corrections to certain pieces of the coils. Generally, each field map showed an improvement of the reconstruction of the elastic peak in terms of the position and the resolution. The latest map, however, has not been used yet for the RG-A data, which uses a map from 2018. The plan is to implement the latest map produced in 2021 to improve the reconstruction of charged particles for future run groups.

BIBLIOGRAPHY

[1] S.L. Glashow *et al.*, Phys. Rev. D **2**, 1285 (1970).

[2] J. Aubert *et al.*, Phys. Rev. Lett. **33**, 1404 (1974).

[3] A. Solliday, Symmetry Magazine (2014).

[4] J. E. Augustin *et al.*, Phys. Rev. Lett. **33**, 1406 (1974).

[5] U. Camerini *et al.*, Phys. Rev. Lett. **35**, 483 (1975).

[6] B. Gittelman *et al.*, Phys. Rev. Lett. **35**, 1616 (1975).

[7] S. J. Brodsky *et al.*, Phys. Rev. B **23**, 498 (2001).

[8] M. Thomson, *Modern Particle Physics* (Cambridge University Press, 2013).

[9] I. Hinchliffe *et al.*, Annu. Rev. Nucl. Part. Sci., (2000).

[10] A. Kronfeld *et al.*, Annu. Rev. Nucl. Part. Sci., (2012).

[11] F. Halzen and A. Martin, *Quarks and Leptons: An Introductory Course in Modern Particle Physics* (John Wiley and Sons, 1984).

[12] M. Riordan, "The Discovery of Quarks", SLAC-PUB-5724, 1992.

[13] M.N. Rosenbluth *et al.*, Phys. Rev. Lett **79**, 615 (1950).

[14] C. Diaconu *et al.*, Rom. Journ. Phys. **52**, 972 (2007).

[15] M. Hentschinski *et al.*, Journal of Physics: Conference Series **651**, (2015).

[16] GlueX Collaboration *et al.*, Phys. Rev. Lett. **123**, (2019).

[17] M. Battaglieri *et al.*, Jefferson Lab CLAS12 Proposal E12-12-001A, 2017.

[18] M. Vanderhaeghen *et al.*, Phys. Rev. D. **94**, 074001 (2016).

[19] R. Aaij *et al.*, Phys. Rev. Lett. **115**, 072001 (2015).

[20] M. Eides *et al.*, Mod. Phys. Lett. A. **35**, 2050151(2020).

[21] D. Douglas *et al.*, Annu. Rev. Nucl. Part. Sci. 2001 **51**, 413, (2001).

[22] V. Burkert *et al.*, Nuc. Inst. and Meth. A. **959**, 163419 (2020).

[23] N. Baltzell *et al.*, Nucl. Inst. and Meth. A **959**, 163421 (2020).

[24] R. Fair *et al.*, Nucl. Inst. and Meth. A **962**, 163578 (2020).

[25] M. Mestayer *et al.*, Nucl. Inst. and Meth. A **959**, 163518 (2020).

[26] G. Asryan *et al.*, Nucl. Inst. and Meth. A **959**, 163425 (2020).

[27] D. Carman *et al.*, Nucl. Inst. and Meth. A **960**, 163629 (2020).

[28] Y. Sharabian *et al.*, Nucl. Inst. and Meth. A, **960**, (2020).

[29] M. Antonioli *et al.*, Nucl. Inst. and Meth. A. **962**, 163701 (2020).

[30] P. Chatagnon *et al.*, Nucl. Inst. and Meth. A. **959**, 163441 (2020).

[31] D. Carman *et al.*, Nucl. Inst. and Meth. A. **960**, 163626 (2020).

[32] S. Boyarinov *et al.*, Nucl. Inst. and Meth. A. **966**, 163698 (2020).

[33] B. Raydo *et al.*, Nucl. Inst. and Meth. A. **960**, 163529 (2020).

[34] V. Ziegler *et al.*, Nucl. Inst. and Meth. A. **959**, 163472 (2020).

[35] S. Stepanyan (private communication)

[36] P. Ghoshal et al., IEEE Transactions On Applied Superconductivity, **29**, (2019).

[37] F. X. Girod (private communication)

[38] M. Defurne, in The CLAS12 Ready For Science Review, 2017.

[39] D. Carman, in The 15th International Conference on Meson-Nucleon Physics and the Structure of the Nucleon, 2019.

[40] M. Battaglieri, in The InterInternational Workshop On Partial Wave Analysis For Hadron Spectroscopy, 2015.

VITA

Joseph Newton
Department of Physics
Old Dominion University
Norfolk, VA 23529

Joseph Newton is a Ph.D. student at Old Dominion University and is projected to graduate in August 2021. He started his graduate studies in 2014 and began full-time research in 2016 with CLAS12.

Typeset using LaTeX.